UNIVERSITÀ DEGLI STUDI DI PARMA

Dottorato di Ricerca in Fisica
XXIV ciclo

DYNAMICAL AND RHEOLOGICAL CHARACTERIZATION OF 2D ARCHITECTURES AT THE AIR/WATER INTERFACE

Caratterizzazione dinamica e reologica di architetture 2D all'interfaccia aria/acqua

COORDINATORE:
Chiar.mo Prof. Pier Paolo Lottici
TUTOR:
Chiar.mo Prof. Luigi Cristofolini

DOTTORANDO:
Dott. Davide Orsi

It is a reasonable position to deny the stones in the street; it will be a religious dogma to assert them. It is a rational thesis that we are all in a dream; it will be a mystical sanity to say that we are all awake. Fires will be kindled to testify that two and two make four. Swords will be drawn to prove that leaves are green in summer.
We shall be left defending, not only the incredible virtues and sanities of human life, but something more incredible still, this huge impossible universe which stares us in the face.
We shall fight for visible prodigies as if they were invisible.
We shall look on the impossible grass and the skies with a strange courage.
We shall be of those who have seen and yet have believed.

— G.K. Chesterton

a Maria Camilla

ABSTRACT

This Thesis reports the characterization of the mechanical response and of the internal microscopic dynamics of 2D Langmuir films, performed and interpreted within the theoretical framework provided by fluctuation-response function theorems. The mechanical shear modulus of Langmuir films has been measured by means of the Interfacial Shear Rheology technique (ISR). X-ray photon correlation spectroscopy (XPCS) experiments were performed to characterize the slow microscopic dynamics of samples either at the air/water interface or transferred on solid substrate.

Two kind of systems have been investigated: polymeric films made of a photosensitive azobenzene-polyacrylate (PA4), and films of gold nanoparticles (GNPs) forming a 2D gel.

Langmuir films of PA4 present an elastic shear response, which can be controlled at will by suitable illumination, induceing photoisomerisation of the azobenzene and therefore a transformation from an elastic to a viscous film. This process is accompanied by an acceleration, of more than one order of magnitude, of the internal dynamics, without a change in any thermodynamic parameter (temperature or surface pressure). Also, back isomerization with blue light acts on the system as an "optical quench". All this allows the polymer to be brought out of equilibrium- and its dynamics being studied- in a novel and unconventional way.

GNP films are characterized by an heterogeneous morphology, with a foam-like structure at low concentration, and a Levy-distribution of sizes, which is deemed to be at the origin of the elastic, gel-like mechanical response observed. The slow dynamics of the films, observed by XPCS on the spatial scale of hundreds of nanometers, has an hyper-diffusive character which has been found in many arrested systems. Dynamical heterogeneities have been observed and characterized by means of higher order correlation functions -in particular, four times correlation functions have been experimentally accessed for the first time in an XPCS experiment in the course of this work. The GNP 2D gel dynamics is characterized by two distinct time scales; both fast and slow motions are confined to the surface plane (2D) and have similar dependencies on the exchanged momentum, and on the coverage fraction. The degree of heterogeneity increases with concentration; at the same time, it seems that the motion involves a hierarchy of spatial scales. These results are compatible with theoretical results and simulations of the dynamics of colloidal gels.

PUBLICATIONS

Some results and discussions presented in this work have been previously reported in the following articles, published on international peer-reviewed scientific journals.

- D. Orsi, L. Cristofolini, M. P. Fontana, E. Pontecorvo, C. Caronna, A. Fluerasu, F. Zontone, and A. Madsen
  Microscopic dynamics in nanocomposite photosensitive films studied by X-ray Photon Correlation Spectroscopy
  PHILOSOPHICAL MAGAZINE, 1478-6435 (2010)

- D. Orsi, L. Cristofolini, M. P. Fontana, E. Pontecorvo, C. Caronna, A. Fluerasu, F. Zontone, and A. Madsen
  Slow dynamics in an azopolymer molecular layer studied by X-ray Photon Correlation Spectroscopy
  PHYSICAL REVIEW E 82(3), 031804, (2010)

- D. Orsi, L. Cristofolini, and M. P. Fontana
  Equilibrium and out-of-equilibrium dynamics in a molecular layer of azopolymer floating on water studied by Interfacial Shear Rheology
  JOURNAL OF NON-CRYSTALLINE SOLIDS, 357(2), 580-586 (2011)

- D. Orsi, A. Fluerasu, L. Cristofolini, A. Moussa id, F. Zontone, and A. Madsen
  Dynamics in dense hard-sphere colloidal suspensions
  PHYSICAL REVIEW E, 85, 011402 (2012)

- D. Orsi, P. Cicuta, G. Baldi, and L. Cristofolini
  On the relation between hierarchical morphology and mechanical properties of a colloidal 2D gel system
  COLLOIDS AND SURFACES A, in press (2012)
  DOI: 10.1016/j.colsurfa.2012.01.001

- D. Orsi, G. Baldi, A. Madsen, and L. Cristofolini
  Heterogeneous dynamics and superdiffusion in a 2D gel
  PHYSICAL REVIEW LETTERS, accepted (2012)

The most amazing combinations can result
if you shuffle the pack enough.

— Mikhail Bulgakov
The Master and Margarita

ACKNOWLEDGMENTS

I am deeply indebted towards *Prof. Luigi Cristofolini* for his friendship and support. This Thesis would not have been possible without his unique and remarkable scientific guidance.

I would also like to acknowledge and thank

Dr. Anders Madsen
for the priceless discussions/lessons/advices on XPCS experiments and their interpretation, with particular regards to the aspects connected with dynamical heterogeneities. His irreplaceable expertise proved -in many occasions- to be essential during XPCS experiments.

Dr. Pietro Cicuta
for his support, his help and the useful discussions on rheology. I also thank him for the opportunity to perform rheology measurements at Cavendish Laboratory (Cambridge, UK);

For their friendship and the precious help they provided me, I want to thank

Dr. Giacomo Baldi
for his help in XPCS experiments on gold nanoparticle films, and during the interpretation of the results;

Dr. Andrei Fluerasu
for having introduced me to XPCS and speckle visibility experiments, and for his help with XPCS experiments (and for the Champagne!);

Francesca Pincella
for the aid with gold nanoparticles sample preparation and characterization;

Agostino Romeo and *Matteo Parmigiani*
for their contribution to the rheological characterization of Langmuir films of lipids.

CONTENTS

ACRONYMS

AFM	Atomic Force Microscopy
APD	Avalanche Photo-Diode
BAM	Brewster Angle Microscopy
DLS	Dynamic Light Scattering
EPR	Electron Paramagnetic Resonance
GNPs	gold nanoparticles
GSE	generalized Stokes-Einstein
KWW	Kolraush-William-Watts
ISR	Interfacial Shear Rheology
LS	Langmuir-Schaeffer
MPT	Multiple Particle Tracking
MSD	mean square displacement
SEM	Scanning Electron Microscopy
SGR	soft glass rheology
TEM	Transmission Electron Microscopy
VFT	Vogel-Fulcher-Tamman
XPCS	X-ray Photon Correlation Spectroscopy
XSVS	X-ray Speckle Visibility Spectroscopy

Part I

LANGMUIR ARCHITECTURES

1 INTRODUCTION

1.1 A BIT OF HISTORY

The investigation of bidimensional systems at the air/water interface has its foundation in the late XIX century, when the experiments of Lord Raileigh [1] and A. Pockels [2] provided evidence that films at the air/water interface may have a thickness limited to one molecule. These experiments proved that the measurement of the variation of the surface tension of water due to the presence of oil films allows a precise study of the correspondent phase diagram. Since then, the measurement of surface tension variations is one of the basic tools for the study of architectures at the air/water interface.

The work of I. Langmuir in 1920-1940 provided a deeper insight on the processes that lead to the formation of films at the air/water interface [3] -now named after him- depending on the properties of the subphase [4, 5]. Moreover, during these years the study of interfacial films proved to be particularly fertile on an applicative perspective. The step towards application was made possible by the deposition of mono and multilayers on solid substrate, a technique pioneered by K. Blodgett and V. Schaefer: one of the first application regarded the use of deposited films to suppress light reflection from a glass [6]. The experimental devices developed by Langmuir, Schaeffer and Blodgett -in particular the trough and the deposition techniques and tools named after them- are still, with minor modifications and upgrades, the key components of laboratories devoted to the study of interfaces.

During the second half of the XX century, several techniques were developed in order to characterize the mechanical response of interfacial films; usually, they consisted in adaptation of "3D" rheometers -such as the *tube* and *concentric cylinders* rheometers- to the reduced dimensionality of 2D films. These measurements aided the understanding of the internal dynamics of the films in equilibrium conditions, exploiting the connection between mechanical response and dynamics provided by the *fluctuation-response function* theorems [7], whose theoretical foundations were settled in the 1960'. At the same time the structure of the film could be investigated, at atomic resolution, by neutron reflectivity, X-ray reflectivity and grazing incidence diffraction.

Alongside the measurement of the mechanical properties of Langmuir architectures, their slow internal dynamics could also be directly measured by means of spectroscopy techniques. Optical techniques

such as FT-IR spectroscopy and non-linear second harmonic generation proved to be powerful tools to provide very detailed informations on the structure and the dynamics of the film at the molecular level. Significant relevance was gained by Dynamic Light Scattering (DLS) [8]; this technique, made possible by the advent of lasers and integrated circuits in the second half of the XX century, allow the measurement of the diffusional and rotational diffusion coefficients of colloids, molecules and cells -in bulk and at the air/water interface.

Finally, scanning microscopies (SEM, TEM, AFM) are commonly employed to observe the micro and nanoscopic of Langmuir films transferred on substrates such as mica, glass or silicon.

In the last two decades, the study of Langmuir architectures -from both a mechanical and a dynamical point of view- was supported and enhanced by many technological improvements, such as the availability of

- fast, high resolution CCD cameras;
- optical tweezers, a tool consisting of highly focused laser beams that can apply force of the order of piconewtons to a nanoscopic sample;
- fast computers with enough memory to handle large simulations of molecular dynamics.

The increase in velocity, sensitivity and accuracy provided by these more efficient tools discloses the possibility of *real-time* characterization of *out-of-equilibrium* interfacial processes, a key feature in both applicative and theoretical research. Moreover, the direct observation of structure and dynamics of 2D films using a microscope, in addition to the ability to accurately control their density over a wide range, constitutes a straightforward scientific approach that is more problematic -or even impossible- in 3D systems.

1.2 MOTIVATIONS

The study of Langmuir architectures is motivated by the many technological perpective /applications it provides in several fields, including food science, cosmetics, medicine, optics, bio-inspired nanotechnology and nanoelectronics industries. As a matter of fact, many advances and improvements have been made possible by a deeper comprehension of the mechanical response and of the internal dynamics of Langmuir films, along with the aging behavior, which is relevant e.g. for determining shelf-life of many products.

Food science and cosmetics industries are particularly interested in understanding how to improve the stability of foams, cremes and emulsions, where the interface play a fundamental role. As examples, one

may consider mayonnaise, whipped creams, detergents, beauty face masks, shaving foams, etc. The stability of the emulsion "honeycomb" structure that characterizes all these systems is maintained by means of Van der Waals or dipolar interactions between the molecules that form the interfaces [9]. These forces equilibrate the defoaming effect of gravitation and concentration/pressure gradients; at the same time they are responsible of the mechanical properties of the system: depending on the application, the shear and compressional properties have to be conveniently tuned.

The dynamical and mechanical properties of interfacial films may also improve systems with applications in *medicine*, with particular regard towards less invasive nanoscopic spproaches to therapy and diagnostics. As a typical example, one may consider organic nanocapsules, capable of on-command targeted delivery of their content. In fact, nanoparticles functionalized with a layer of antibodies or receptors may be driven towards a certain organ or tumor for therapy -thermal therapy or drug delivery- or diagnostic/imaging [10, 11]. Recent applications for cancer *photodynamic therapy* are based on inorganic nanotubes and nanowires coated with layers of organic molecules [12, 13, 14]; when these systems are irradiated with light or X-rays, the organic coating emits radicals that kill cancer cells. Here, the properties of the inorganic/organic interface play a key role towards the desired functionality.

Moreover, monolayers of lipids at the air/water interface constitute the simpler experimental model systems available of *cellular membranes*. Subsequently, this enabled the investigation of the modification of dynamical and mechanical properties of biological membranes induced by the interaction with drugs and proteins [15, 16, 17].

In recent years, *electronics and nanotechnology* focused on the study of organic interfaces: organic electronic devices could overcome the limits of the silicon technology connected with the size of the devices. Actually, semiconductor transistors in integrated circuits have reached the limit size of 20-30 nanometers, above which quantum effects disrupt their functionality. Only a molecular approach may surpass this limitation. At the same time, organic nanoelectronics could take advantage of the self-assembly, bottom-up approach towards production [18], building the device starting from the single molecule. This could lead to an increment in performances, accompanied by a consistent reduction of production costs. Among the several possible application, we may count

- command surfaces for liquid crystal displays;
- high-density optical data storage [19] realized by means of layers of photosensitive polymers;

- nanoparticles coated with conductive/insulating polymers, for molecular , single-electron transistors [20], characterized by the Coloum Blockade and Coloumb Cascade phenomena;

- organic/inorganic hybrid films with photovoltaic capabilities [21]: despite showing a reduced efficiency and aging problems, they may be integrated on virtually any device, including plastics and fabrics.

Finally, organic 2D films with tunable dynamical and mechanical properties are employed in several nanotechnology prototypes such as

- hydrophobic on-command surfaces, with auto-cleaning capabilities driven by the tunable dipole density of the surface [22];

- nanosized motors and actuators [23, 24];

- fabrics with improved resistance [25].

1.3 FLUCTUATION AND RESPONSE FUNCTIONS: TWO SIDES OF THE SAME PHENOMENON?

The experimental investigation of Langmuir architectures constitutes an accurate tool for the study of several phenomena of theoretical interest, such as dynamical heterogeneity [26] and anomalies in the vibrational density of states [27, 28], that received huge attention in the past years from the scientific community. Furthermore, 2D architectures act as models of a wide class of ideal arrested system of interest for statistical physics, to study phenomena like glass transition, gelification and dynamical arrest in reduced dimensionality.

Equilibrium and *out-of-equilibrium* dynamics can be studied in two ways: by studying the response to external mechanical stresses, or through the investigation of the relaxation times that govern the dynamics of the system. The two approaches are complementary, and despite the very different experimental techniques that each of them involves, the informations provided are deeply linked.

The links are provided by *fluctuations-response function theorems* that -when their validity is demonstrated- provide a quantitative connection between the characteristic parameters of the mechanical response of the system and the dynamical relaxation times.

Two simple and widely known examples of such relations are the *fluctuation-dissipation* theorems demonstrated in the early 20^{th} century for Brownian motion (Einstein [29]) and for the thermal noise in a resistor (Johnson-Nyquist [30]).

As an example of the first, we consider a diluted colloidal suspension of micron-sized particles (radius R) in water as basic system to qualitative test the existence of these relations. The thermal fluctuations of the molecules influence the motion of the colloidal probes in two different ways: they generate their random motion, and at the same time they give rise to the friction force that arises when the particle is moved by an external force (i. e., an electric field on charged particles). These two phenomena, the random *fluctuations* of the colloidal probes and the *dissipative friction* that is opposed to their motion, are likely to be related *since they share the same origin*.

Following the work of Kubo [7, 31], this argument can be formalized considering the results of Einstein theory of Brownian Motion. The diffusion coefficient D of the colloidal probes is proportional to their mobility μ:

$$D = k_B T \mu. \tag{1.1}$$

The diffusion constant is obtained from the mean square displacement (MSD)

$$D = \frac{\langle x(t) - x0) \rangle^2}{2t}, \tag{1.2}$$

where the average is performed over the ensemble of particles. If u is the particle velocity, then the displacement of a particle is $x(t) - x(0) = \int_0^\infty u(t')dt'$, and the diffusion coefficient can be related to the autocorrelation function of particle velocity:

$$D = \frac{1}{2t}\int_0^\infty dt_1 \int_0^{t_1 - t'} \langle u(t_1)u(t_1 + t')\rangle \, dt' = \\ = \int_0^\infty \langle u(t_0)u(t_0 + t)\rangle \, dt \tag{1.3}$$

The Stokes relation, valid in low Reynolds number regime, relates the mobility of a spherical particle to the viscosity of the colloidal suspension, so that $\mu = \frac{1}{\zeta} = \frac{1}{6\pi R\eta}$, where ζ is the Stokes drag coefficient. The Einstein relation for Brownian motion can therefore be written as a inverse proportionality between the diffusion coefficient D (*fluctuation*) and the suspension viscosity η (*response function*), retrieving the widely known Einstein-Stokes relation:

$$D = \frac{k_B T}{6\pi R\eta}. \tag{1.4}$$

A first step towards a generalization of this classical equation is obtained by substituting the diffusion coefficient D with the right term of equation 1.3 [7], so that the inverse of the suspension viscosity η is now proportional to the *correlation function* of the particle velocity:

$$\frac{1}{\eta} = \frac{6\pi R}{k_B T}\int_0^\infty \langle u(t_0)u(t_0 + t)\rangle \, dt. \tag{1.5}$$

Equation 1.5 connects the mechanical response function to the correlation function of a relevant experimental quantity of the system; the characterization of the dynamics of the system may take advantage of both rheological and fluctuation measurements.

A recently proposed generalized Stokes-Einstein (GSE) relation for viscoelastic fluids [32, 33] relates the viscoelastic response of a colloidal suspension to the correspondent diffusion coefficient, e. g. measured in a dynamic light scattering experiment. It relates the Laplace transform of the MSD, $\langle \widetilde{r}^2(s)\rangle$, to the Laplace transform $\widetilde{G}(s)$ of the mechanical response function $G(t)$. This GSE equation allow the interpretation of colloidal probe motion in a 2D viscoelastic film [34, 35]:

$$\langle \widetilde{r}^2(s)\rangle = \frac{2}{3}\frac{k_B T}{\pi R s \widetilde{G}(s)} \tag{1.6}$$

the reduced dimensionality influences the value of the numerical coefficient only ($\frac{2}{3}$ in 2D, 1 in 3D). Equation 1.6 is the founding relation of Multiple Particle Tracking (MPT), a technique that measures the shear modulus of interfacial films via the MSD of microscopic tracers embedded into it.

1.4 STRUCTURE OF THE WORK

This Thesis reports on the investigation of mechanical properties and internal dynamics of Langmuir architectures. The informations obtained from the measurements of the interfacial mechanical properties and of the microscopic dynamics will be combined to reach a more complete understanding of the properties of these systems. Therefore we may say that the family of Theorems relating response functions to the spontaneous fluctuations of the system constitutes the background and the foundations of this Thesis.

In part (ii) the interpretative theoretical grounds of interfacial rheology are outlined. Next, the experimental devices used to characterize the response to an interfacial shear stress are described. Part (iii) illustrates how photon correlation experiments with visible light and X-rays can access the internal dynamics of interfacial systems by means of intensity correlation functions. In particular, second and fourth order density auto-correlators describe accurately the internal dynamics along with its possible heterogeneity.

Part (v) and (iv) contain the mechanical and dynamical characterization of two interfacial systems:

- films of gold nanoparticles, a model of a 2D gel;
- molecular layers of a photosensitive, liquid-crystalline polymer that can be driven out-of-equilibrium through perturbation with UV and blue lights.

Finally, results are to be compared and interpreted with respect to a model, recently proposed in the literature, *which can be viewed as a generalized fluctuation-response function relation*.

2

INTERFACIAL MONOLAYERS: THE LANGMUIR TECHNIQUE

2.1 THE AIR/WATER INTERFACE

An interface is a surface separating two bulk phases, which exhibits peculiar properties, absent in either phase it delimits. The air/water interface is perhaps the most common interface encountered in everyday experience. Because of its generic definition (as a delimiting region that possesses unique properties not present in the bulk) the interface thickness may not be precisely defined, as it depends on the intermolecular forces present in the subphase, ranging up to several nanometers. For instance, the coulombic interactions between charged molecules can extend the interfacial regions much beyond the usual thickness of one or two molecular diameters that is observed in system composed by neutral molecules.

As discovered in the late XIX century [1, 2], in equilibrium conditions the air/water interface always assumes the shape that minimizes its area. The reaction to any deformation of the shape of the interface region itself is called *surface tension*, and has the dimensions of a force divided by a length.

If we consider the energy possessed by each molecule of the water surface, the molecules with the minimum energy are those of the bulk, where they are surrounded by the maximum number of neighbors. The molecules at the interface, instead, possess an higher energy, due to the lower number of neighbors. Since the equilibrium state is that of minimal energy, it will presents the lower possible number of interfacial molecule, and therefore by the minimum area.

Therefore, the surface tension γ can be defined as the partial derivative of the Gibbs free energy G [36] with respect to the surface area A:

$$\gamma = \left(\frac{\partial G}{\partial A}\right)_{T,P} \tag{2.1}$$

while temperature T and pressure P are considered constant. Another way of visualizing this phenomenon is considering the motion of the molecules. At equilibrium, the exchange rates of molecules from the bulk to the surface and back must be equal. Since molecule at the surface is surrounded by fewer molecules than one in the bulk liquid, more molecules will diffuse initially from the surface, increasing the mean atomic separation between surface molecules, as well as the inter-molecular forces [37].

The air/water interface present a surface tension equal to $72.8 mN/m$ at $20°C$. This value is exceptionally high if compared to other liquids, and contributes to explain why water is a very common subphase in surface experiments. The presence of a monomolecular film on a liquid surface will affect the surface tension: the reduction of the pure liquid surface tension due the film is called *surface pressure* Π,

$$\Pi = \gamma_0 - \gamma \tag{2.2}$$

where γ_0 is the surface tension of the pure liquid and γ is the surface tension of the film-covered surface. Usually, Π for the air/water surface is of the order of some mN/m; obviously, the maximum value of Π is equal to γ_0 for water.

These considerations imply that the formation of a molecular layer at the air/water interface can be easily studied by monitoring the surface pressure Π. The trough containing the subphase is equipped with a set of moving barriers that can run over the water, thus varying the available surface A. In this way, the pressure Π can be monitored as a function of sample packing, ensuring a continuous control of the sample phase transitions that may occur as the surface area is reduced.

2.2 THE LANGMUIR TROUGH

A fundamental tool for the scientific investigation of molecular films at the air/water interface is the Langmuir trough, depicted in figure 1. It consists of a container made of highly polished Teflon, a relatively common and cheap hydrophobic material, fixed to an aluminum base, equipped with a system of internal channels for water heating/cooling circulation. Two Teflon barriers can be moved synchronously onto the trough, varying the area A of the air/water interface. Teflon is employed because its hydrophobicity ensure the formation of a concave meniscus when the trough is completely filled with water. This meniscus reduces the formation of collapses and aggregates in the film, during its formation.

The purity of the water surface is a key parameter to control the successful formation of a uniform monolayer at the interfaces, so an accurate cleaning procedure is performed before each measurement: the trough and the barriers are washed multiple times with hot water and soap, and finally rinsed with high-purity water.

The solution of the insoluble molecules we want to investigate is dispersed onto the water surface. When the solvent is completely evaporated, the molecules are confined on the water surface in a 2D gaseous state. In case of *amphiphilic* molecules (such as stearic acid), characterized by hydrophilic and hydrophobic portions, we find that the first is immersed in water while the second is lifted out of the water subphase.

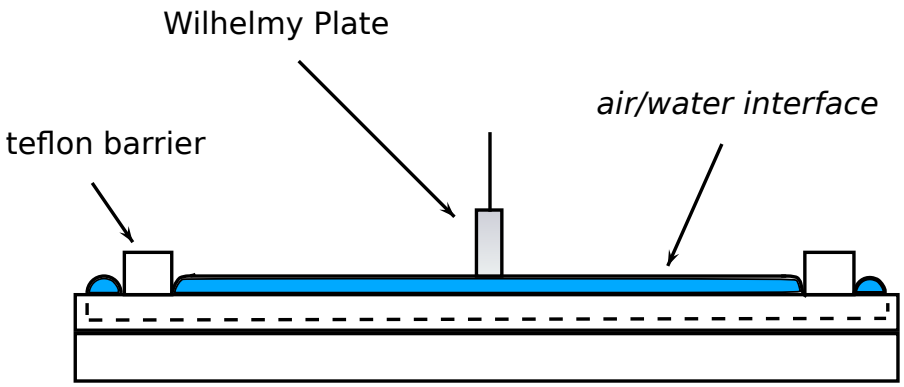

Figure 1: Sketch of a double barrier Langmuir trough

The surface pressure Π is measured using a device, called *Wilhelmy balance*, that operates through the detection of the force necessary to keep a small (1cm wide) filter paper plate, partially immersed into the liquid, at constant height. This force has to equilibrate the sum of the surface tension, the weight of the plate and the buoyancy due to displaced water. The balance measures this force as the voltage that has to be applied to the electromagnet that holds the plate to keep constant its vertical position. The voltage-surface pressure calibration is performed either using calibration weights, or by measuring the variation ΔF of the equilibrating force when the wet paper plate, previously immersed in pure water, is lifted up out of the subphase. If the paper is thin enough, the difference of surface tension is then

$$\Delta\gamma = \frac{\Delta F}{2W}$$

where W is the plate width. Moreover, this force variation corresponds to 72.8mN/m, the value of surface pressure of a clean air/water interface.

2.3 Π − A ISOTHERMS

A first characterization of a monolayer at the air/water interface can be achieved by the measurement of the surface pressure, in equilibrium conditions, as a function of the surface area available to any molecule on the water surface. In practice, this measurement is usually performed in quasi-equilibrium conditions, during constant area reduction, achieved with the slow motion of the teflon barriers that equip the Langmuir trough; the obtained curve is called *surface pressure - area (Π − A) isotherm*, as it is measured at constant temperature. A paradigmatic calibration measurement is the Π − A isotherm of stearic acid, shown in figure 2.

The curve can be divided into several regions; in each region the surface pressure grows roughly at constant rate, and a change of slope indicates a "phase" transition. A complete characterization of

the different phases of lipid monolayers is reported in a review by Kaganer, Möhwald and Dutta [38]. The review reports experiments performed by means of x-ray-diffraction experiments, computer simulations, molecular models that allowed the reconstruction of phase diagrams of many amphiphilic molecules at the air/water interface.

- At large values of the area, molecules do not interact with each other; the monolayer can be considered to lay in a "gaseous" state, at zero surface pressure.
- A first small increase of the surface pressure to a constant value smaller than $1 mN/m$ is caused by the lifting of the hydrophobic tail of the stearic acid from the water surface.
- At lower values of the surface area, the surface pressure starts to grow linearly, as a consequence of the onset of intermolecular interactions: the monolayer is in the so-called "liquid" phase.
- A "solid" phase is reached by further reduction of the area, which results in a steeper increase of Π. The close packing of the molecules lifts the hydrophobic tails completely out of the subphase and orients them into an ordered phase.
- By compressing the solid phase above a rupture point, collapses start to appear in the molecular layer, with the formation of portions of film denoted by bilayers and/or aggregates.

In addition to this rough and oversimplified categorization of the possible phases of Langmuir films, it has to be mentioned that several *liquid-liquid* and *solid-solid* transitions have been observed in the literature, depending of the properties of the molecules at the interface.

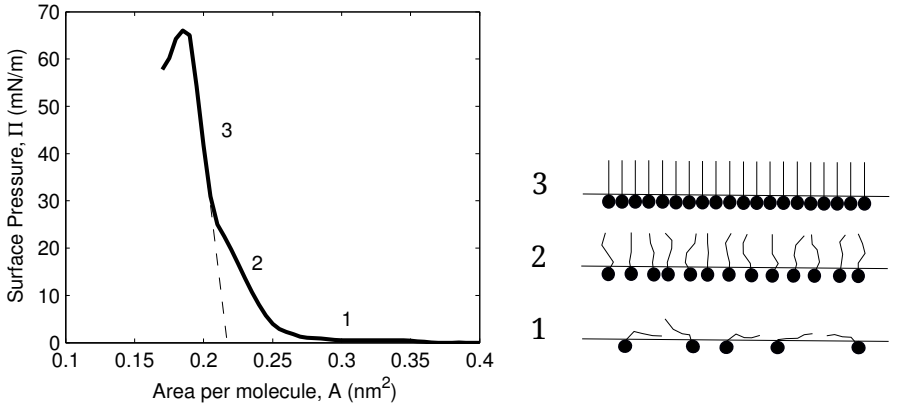

(a) (b)

Figure 2: a) An example of pressure-area isotherm: stearic acid on water surface. The dashed line is the linear fit to the steeper region, described in the text. b) different phases of a Langmuir monolayer: from bottom to top, gas, liquid and condensed phases.

An *area per molecule*, the area occupied by a single molecule in a compact film, is measured as the intercept with the abscissa axis of the line used to fit the portion of the isotherms corresponding to the "solid" phase.

2.4 TRANSFERRED MULTILAYERS ON SOLID SUBSTRATE

In order to be attractive from the point of view of technological applications, Langmuir monolayers have to be transferred onto solid substrate, such as glass or silicon.

Moreover, some of the characterization techniques used in this Thesis are not feasible at the air/water interface, either because of the low signal-to-noise ratio arising from a single molecular layer, or because the presence of a liquid subphase is incompatible with the experimental setup, as in scanning electron microscopy where measurements are performed in void.

A Langmuir film in the *liquid condensed* phase can be transferred on a properly prepared surface by means of either

- the Langmuir-Shaeffer (horizontal) deposition technique;
- the Langmuir-Blodgett (vertical) deposition technique;

In the Langmuir-Shaeffer technique the film, previously compressed up to desired surface pressure, is divided into small rectangular portions by placing a plastic mask -which present several rectangular holes- onto the water surface. The operator holds the substrate, horizontally oriented, using a pair of tweezers; then he places the substrate in contact with the film at the air/water interface. If the film-substrate interaction is strong enough, the film is transferred onto the substrate as this is gently lifted up. Then, the residual water is removed using a subtle nitrogen blow. The gesture is repeated for each portion the film in divided into, obtaining a multilayer sample deposited onto the solid substrate. The main advantage of this technique is that it does not require any special equipment; however, the uniformity of the deposited film is strictly related to the operator skills.

The Langmuir-Blodgett technique, on the contrary, the substrate is mounted vertically on a motorized support. The substrate is then slowly immersed completely and extracted, so that a layer of molecules is transferred onto it. This can be repeated as many times as desired. Meanwhile, the area of the trough is continuously reduced, in order to keep constant the surface pressure of the film. The Langmuir-Blodgett technique requires dedicated deposition hardware and software, but it ensures the deposition of molecular layers with high uniformity and reproducibility

In both techniques, the substrate has to present a clean and smooth surface in order to ensure that the fewest modification are induced on

the film structure by the transfer process. Depending on the characteristic of the substance that has to be transferred, the substrate may have to be modified by proper techniques and treatments, such as silanization, in order to make it more hydrophobic/hydrophilic, thus ensuring a complete and uniform transfer. Despite the highest accuracy paid in the deposition process, the first layers always suffer a certain degree of modification with respect to the structure shown at the air/water interface. The internal properties and dynamics are affected by the proximity to the surface. For this reason, in this Thesis a total number of more than 10 layers is usually transferred, for a total sample thickness of tens /hundreds of nanometers, so that the bulk properties are investigated.

2.5 CHARACTERIZATION OF LANGMUIR LAYERS: COMPLEMENTARY TECHNIQUES

Langmuir monolayers, either at the air/water interface or transferred on silicon substrate, were characterized in this Thesis using several complementary techniques. Their morphology and structure of sampless and films, as well as its uniformity/heterogeneity [37] were investigated. A brief selection of common techniques is reported in the following list, along with the instrumental equipment used during this project.

- *Optical microscopy* either on deposited multilayer or directly at the air/water interface; in the latter case, a custom trough equipped with a window is used on an inverted microscope. Microscopy is particularly useful to check the absence of aggregates and the uniformity of the film, but only on the microscopic scale.

- *Transmission Electron Microscopy (TEM)*, *Scanning Electron Microscopy (SEM)* and *Atomic Force Microscopy (AFM)* to observe and characterize the morphology of deposited layers down to the nanoscale. The SEM microscope used in this work is a FEG-SEM Zeiss Supra 40[1] operated at $2-10$kV, while AFM images have been obtained using a ThermoMicroscope Autoprobe CP Research instrument[2], commonly operated in contact mode with a SiN soft cantilever.

- *Brewster Angle Microscopy* and *Null-Ellipsometric Imaging*. In extinction condition, obtained by reflection on the water surface at the Brewster angle or by means of polarizers, the reflected intensity from the surface is zero. The extinction condition is broken by the presence of the film, so that it is possible to observe *in-situ* the formation of a Langmuir layer and characterize the

1 Carl Zeiss NTS GmbH, DE
2 ThermoMicroscopes, Sunnivale CA, USA

eventual presence of domains in the structure of the condensed-liquid phase (i.e. in lipids). Null-ellipsometry in imaging mode was performed with an Optrel-Multiskop[3] ellipsometer operated at wavelength $\lambda = 632nm$ and by an EP3 NANOFILM[4] Microscope operated at $\lambda = 532nm$.

- *Null-ellipsometry*, to measure the thickness of Langmuir mono and multilayers by studying how the polarization of an incident laser beam is modified upon reflection from the sample. The change in the polarization state is connected to the thickness and refractive index of the sample by the Drude-Fresnel equations. These measurements were conducted using the Optrel-Multiskop Ellipsometer.

- *UV-Vis absorption spectroscopy*, used to measure the absorption spectrum of the films and evaluate concentration of sample solution. For gold nanoparticle samples, this technique was also employed to check the nanoparticle size. UV-Vis spectroscopy measurements were performed in this work using a Jasco V-500 spectrometer.

- *Grazing Incidence X-ray Diffraction* (GID) and *X-ray Reflectivity* (XRR), to determine the structure of compact films at the air/water interface.

2.6 TROUGHS

The laboratory for Molecular Nanotechnology in Parma is equipped with several Langmuir troughs. In particular, two specific custom troughs[5] were used:

- A $8.5x25.5cm^2$ trough for ellipsometry and rheology measurements;

- A $4x25cm^2$ trough featuring a circular glass window placed in its center, to be used on an inverted microscope equipped with long focal objectives.

Both trough are controlled using an electronic hardware from R&K[6], equipped with a PID controller for measurements performed while keeping constant the surface pressure. The whole system is interfaced with a computer, using Matlab for data acquisition.

3 Optrel GbR, Sinzing, DE
4 Accurion GmbH, Goettingen, DE
5 Mechanical Laboratory - Physics Department, University of Parma
6 Riegler & Kirstein GmbH, Potsdam, DE

Part II

MECHANICAL RESPONSE FUNCTIONS

Detailed description of the fundamental theory and the experimental setups behind the measurements of the mechanical response functions of a Langmuir film.

3

MECHANICAL RESPONSE OF 2D FILMS

In the previous chapter, we have described the techniques and procedures that allow the formation and characterization of a Langmuir monolayer. In order to obtain more detailed informations on its mechanical properties, the *rheology* -the measurement of the mechanical response- of monolayers of insoluble surfactants has to be considered. In analogy to the usual bulk rheology, it is possible to follow the response of the film to different perturbations as a function of thermodynamical variables like temperature or surface pressure. The first attempt to project on two dimensions the principles of bulk rheology was formulated by Boussinesq at the beginning of the 20th century [39, 40]. This theory describe the so-called "linear regime", where the study of viscoelastic effects is limited to the restricted interval of stress amplitude where the resulting strain is linearly proportional to the stress. This implies that stress, strain, and their time derivatives are related by a linear differential equation with constant coefficients. In analogy with Miller and coworkers [41], we consider a infinitesimal portion of 2D film. Since the linear regime is investigated, the interfacial stress tensor σ may be defined in term of its deviation from the equilibrium

$$\sigma = \sigma_c + \sigma_s = \sigma_0 \begin{vmatrix} 1 & 0 \\ 0 & 1 \end{vmatrix} + \begin{vmatrix} \sigma_{11} - \sigma_0 & \sigma_{12} \\ \sigma_{21} & \gamma_{22} - \sigma_0 \end{vmatrix} \tag{3.1}$$

Each component σ_{ij} represents the force, exerted along direction i, that acts on a line perpendicular to the direction identified by versor j, as shown in figure 3.

We are not interested into deformation that causes a rigid movement of the whole film. Therefore, we have to exclude deformations where the tensor σ is proportional to the displacement $u = (u_x(x, y, t), u_y(x, y, t))$ of each of its infinitesimal portions -identified by coordinates (x, y).

On the contrary, we investigate deformations where the components of σ are connected to u through linear differential equations. In this situation, the tensor σ is linked to the so-called strain tensor γ, composed by the partial derivatives of u relatively to x and y:

$$\gamma = \begin{vmatrix} \frac{\partial u_x}{\partial x} & \frac{1}{2}\left(\frac{\partial u_x}{\partial y} - \frac{\partial u_y}{\partial x}\right) \\ -\frac{1}{2}\left(\frac{\partial u_x}{\partial y} - \frac{\partial u_y}{\partial x}\right) & \frac{\partial u_y}{\partial y} \end{vmatrix} \tag{3.2}$$

This tensor can be expressed as the sum of an isotropic term γ_c -which has the same trace of γ- and a deviation term γ_s:

$$\begin{aligned} \gamma = \gamma_c + \gamma_s = \\ = \begin{vmatrix} \frac{1}{2}\left(\frac{\partial u_x}{\partial x} + \frac{\partial u_y}{\partial y}\right) & 0 \\ 0 & \frac{1}{2}\left(\frac{\partial u_x}{\partial x} + \frac{\partial u_y}{\partial y}\right) \end{vmatrix} + \\ + \begin{vmatrix} \frac{1}{2}\left(\frac{\partial u_x}{\partial x} - \frac{\partial u_y}{\partial y}\right) & \frac{1}{2}\left(\frac{\partial u_x}{\partial y} - \frac{\partial u_y}{\partial x}\right) \\ -\frac{1}{2}\left(\frac{\partial u_x}{\partial y} - \frac{\partial u_y}{\partial x}\right) & -\frac{1}{2}\left(\frac{\partial u_x}{\partial x} - \frac{\partial u_y}{\partial y}\right) \end{vmatrix} \end{aligned} \tag{3.3}$$

So, both γ and σ tensors can be expressed as a sum of a symmetric tensor and an antisymmetric one, with the symmetric part given by the trace of the sum. A pure *compression* deformation is described by a linear differential equation that involves the symmetric parts of γ and σ. On the contrary, a pure *shear* deformation is described by analogous expressions that involve the antisymmetric parts of γ and σ.

3.1 ELASTIC SOLID

In this section, we consider a purely *elastic* isotropic film floating on the surface. The elasticity of the film implies that the tensors σ and γ are connected by a linear relation:

$$\sigma = \sigma_c + \sigma_s = k_c\,\gamma_c + k_s\,\gamma_s \tag{3.4}$$

The coefficients k_c and k_s are real parameters that express the elastic response of the film to compression and shear stresses; they are known as elastic *compressional* and *shear* modulus, respectively. In the following discussion, compression and shear deformations are considered separately for clarity.

3.1.1 *Isotropic compression*

We consider an isotropic dilation, applied in the same way in all directions - as sketched in figure 3.

In this case the off-diagonal terms of the stress and strain tensors are zero, as clarified by the drawing reported above; the tensors γ and σ reduce to

$$\begin{aligned} \sigma = \sigma_c = \sigma_0\, I \\ \gamma = \gamma_c = \frac{\partial u_x}{\partial x}\, I \end{aligned} \tag{3.5}$$

where I is the identity matrix.

We consider a square portion of the film of side l. A dilation generates a relative increase in the area which is equal to

$$\frac{\Delta A}{A} = \frac{(l + \delta u_x)^2 - l^2}{l^2} = \frac{2\,\delta u_x}{l} + O(\delta u_x^2) \simeq 2\frac{\partial u_x}{\partial x} \tag{3.6}$$

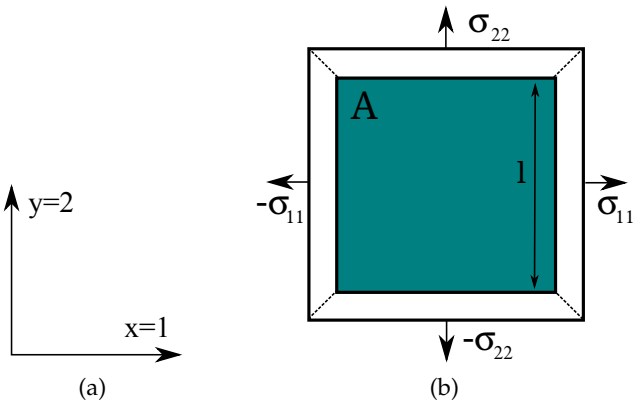

Figure 3: a) System of coordinates b) Sketch of an isotropic compression of a square portion of an elastic films.

therefore the rheological equation can be written as

$$\sigma_0 = k_c \frac{\partial u_x}{\partial x} = k_c \frac{\Delta A}{2A}. \tag{3.7}$$

The parameter k_i is usually expressed in terms of the *Marangoni elasticity modulus* E:

$$k_c = \frac{2\sigma_0}{\Delta A/A} = 2\,E \tag{3.8}$$

which is also known as dilation modulus.

The dilation modulus E can be deduced from a $\Pi - A$ isotherm; the slow reduction of the area at constant rate induces a dilation strain on the film, while the stress is measured as the variation of the surface tension. The compression modulus is proportional to the derivative of the curve

$$E = -A \frac{\partial \Pi}{\partial A} \tag{3.9}$$

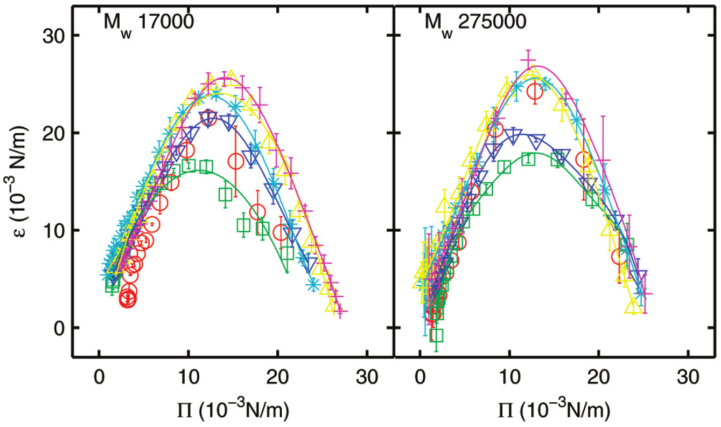

Figure 4: compressional modulus E measured on poly(vinyl acetate) samples characterized by different molecular weights [42].

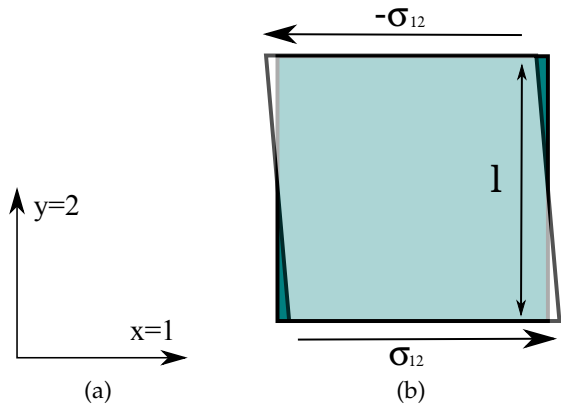

Figure 5: a) System of coordinates b) Sketch of an shear deformation of a square portion of an elastic films.

An example of this measurement, performed on poly(vinyl acetate) samples of different molecular weights by Spigone, Cicuta and coworkers [42], is reported in figure 4. The curves reported in the figure correspond to measurements performed at different values of the compression rate.

3.1.2 *Shearing*

In an analogous way, we consider a shear deformation of a square portion of elastic surface: this example is sketched in figure 5.

In this case the isotropic terms of the stress and strain tensors are null, and the rheological relation involves the deviatoric terms only:

$$\sigma_s = k_s \gamma_s$$

$$\downarrow$$

$$\begin{vmatrix} 0 & \sigma_{12} \\ -\sigma_{12} & 0 \end{vmatrix} = \sigma_0 \begin{vmatrix} 0 & 1 \\ -1 & 0 \end{vmatrix} = k_s \frac{1}{2} \begin{vmatrix} 0 & \frac{\partial u_x}{\partial y} \\ -\frac{\partial u_x}{\partial y} & 0 \end{vmatrix}$$

$$\downarrow$$

$$\sigma_0 = \frac{k_s}{2} \frac{\partial u_x}{\partial y}$$

The shear deformation does not change the area of the portion of film. The *shear elasticy modulus* G_s is defined as $G_s = \frac{\sigma_0}{\partial u_c / \partial y}$, therefore

$$k_s = 2\, G_s. \tag{3.10}$$

In conclusion, the mechanical properties of a perfectly elastic 2D surface can be described investigating the response to compressional and shear deformations, measuring the dilational modulus E and the shearing modulus G_s.

3.2 IDEAL FLUID

In an ideal fluid interface, or 2D Newtonian fluid, dissipation effects have to be considered. Hence, viscosity must replace elasticity in the rheological equations that relate shear and stress tensors. This can be simply done by replacing the vector of displacement u with its time derivative $\dot{u}$, obtaining the corresponding equations for the isotropic and deviatoric parts of the shear and stress tensors. These equations, describing compression and shear deformation, reduce to:

$$\Delta\sigma_c = 2\,\eta_c\,\dot{\gamma}_c \tag{3.11}$$

$$\Delta\sigma_s = 2\,\eta_s\,\dot{\gamma}_s \tag{3.12}$$

following an analogous procedure to that followed for the elastic deformations. The two real parameters η_s and η_c are respectively the *Newtonian shear viscosity* and the *Boussinesq dilational viscosity*.

In order to obtain a complete characterization of the elastic and viscous response of the sample, the elastic moduli E, G_s and the viscosities η_c, η_s have to be determined as a function of the time scale over which the stresses are applied. In real systems, the mechanical response is given by a combination of elastic and viscous behaviors. Several models of composition of these effects have been proposed: in the following sections, two simple models of viscoelastic response are discussed.

3.3 VISCOELASTIC FILM: MAXWELL MODEL

Using the previous simple examples as a starting point, it is possible to describe more complex systems that present both dissipative and elastic motions: the *viscoelastic* systems. These kind of response can be described by the *Maxwell model*, sketched as a series connection of a spring and a dumper.

If the stress applied to the insoluble monolayer is sufficiently small, so that both linearity and the superposition principles are preserved, the stress and strain tensors are related by two equations that are a linear composition of the relations found for the elastic film and the ideal fluid.

$$\begin{aligned} \text{dilation:}\quad & \gamma_c = \gamma_c(\text{elastic}) + \gamma_c(\text{viscous}) \\ \text{shear:}\quad & \gamma_s = \gamma_s(\text{elastic}) + \gamma_s(\text{viscous}) \end{aligned} \tag{3.13}$$

$$\downarrow$$

$$\gamma_c = \frac{\sigma_c}{2E} + \frac{1}{2\eta_c}\int \sigma_c \, dt$$
$$\gamma_s = \frac{\sigma_s}{2G_s} + \frac{1}{2\eta_s}\int \sigma_s \, dt \tag{3.14}$$

The differentiation of equations 3.14 leads to

$$\frac{1}{E}\dot{\sigma}_c + \frac{1}{\eta_c}\sigma_c = 2\dot{\gamma}_c$$
$$\frac{1}{G_s}\dot{\sigma}_s + \frac{1}{\eta_s}\sigma_s = 2\dot{\gamma}_s \tag{3.15}$$

Equations 3.15 are called the *Maxwell model* for viscoelasticity. We note that the rheological parameters can be combined into two characteristic times, $\tau_c = \eta_c/E$ and $\tau_s = \eta_s/G_s$. This reduces the equations to the simpler form

$$\tau_c\dot{\sigma}_c + \sigma_c = 2\eta_c\dot{\gamma}_c$$
$$\tau_s\dot{\sigma}_s + \sigma_s = 2\eta_s\dot{\gamma}_s. \tag{3.16}$$

From now on, a *pure shear deformation* will be considered for brevity. Common experimental devices, developed to measure the mechanical properties of 2D film, like Langmuir monolayers, often rely on an external oscillatory strain applied to the sample. Moreover, any external perturbation can be expressed in terms of its Fourier components. Supposing that such an oscillatory shear strain $\gamma = \gamma_0 e^{i\omega t}$ is imposed on a maxwellian 2D interface, the shear equation 3.16 becomes

$$\tau_s\dot{\sigma}_s + \sigma_s = 2\eta_s\gamma_0 i\omega e^{i\omega t} \tag{3.17}$$

This linear inhomogeneous differential equation has a purely oscillating solution,

$$\sigma_s = \frac{2\eta_s\gamma_0\omega\,(i + \omega\tau_s)\,e^{i\omega t}}{1+\omega^2\tau^2}. \tag{3.18}$$

The *interfacial shear modulus* G is defined as usual as the ratio between shear stress and strain, $G(\omega) = \frac{\sigma_d(\omega)}{2\gamma(\omega)}$. It is a frequency dependent complex parameter

$$G(\omega) = \frac{G_s\tau_s\omega(i+\tau_s\omega)}{1+\tau_s^2\omega^2}, \tag{3.19}$$

whose real and imaginary parts are respectively:

$$G'(\omega) = G_s\frac{\tau_s^2\omega^2}{1+\tau_s^2\omega^2} \tag{3.20}$$
$$G''(\omega) = \eta_s\omega\frac{1}{1+\tau_s^2\omega^2}. \tag{3.21}$$

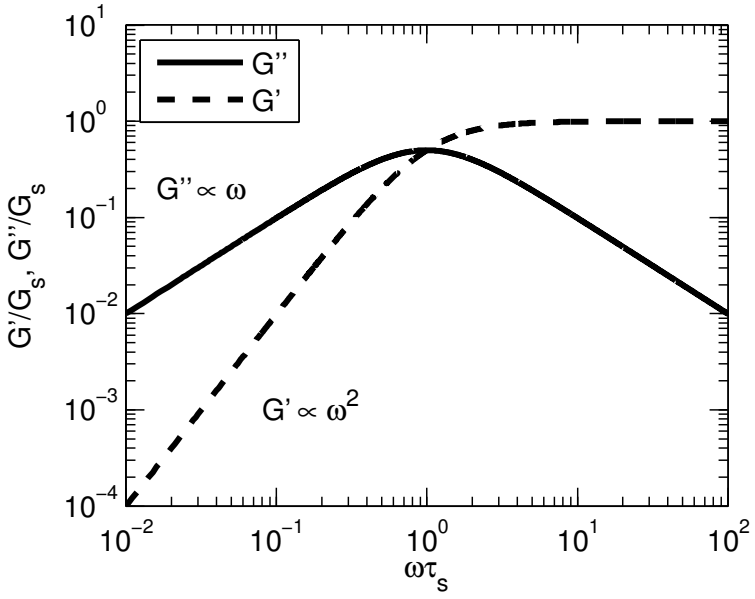

Figure 6: Maxwell model of a viscoelastic film. Normalized shear moduli G' and G'' calculated from equations 3.21, reported as a function of the reduced angular frequency $\omega\tau_s$.

It is worth noting that the real part of G is proportional to the *shear elasticity modulus* G_s, while the imaginary part is proportional to the *shear viscosity* η_s. Therefore, the real part of G, G', contains frequency-dependent information on the shear elasticity of the system, while the imaginary part G'' relates to the frequency-dependent viscous response to shear deformations.

The shear moduli G' and G'' predicted by the Maxwell model are reported in figure 6 as a function of the dimensionless quantity $\omega\tau_S$. As deduced from equation 3.21, the model predicts a *loss factor* - defined as the tangent of the phase lag between stress and strain in an oscillatory experiment- directly proportional to the angular frequency.

$$\tan(\delta) = G''/G' = \omega\tau_s \tag{3.22}$$

Subsequently, at $\omega = 1/\tau_s$ the model predicts a crossover from a dissipative regime at low frequency toward an elastic response at high frequency.

3.4 VISCOELASTIC FILM: GENERALIZED LINEAR SOLID MODEL

The Maxwell model for viscoelasticity often proves to be a somehow too semplicistic, though it describes well the behavior of many systems, like suspensions of surfactant micelles [43, 44].

Nevertheless, it is relatively easy to increase the complexity of the model to account for different phenomenologies. For instance, we

consider a viscoelastic film in which the stess and its derivative are related not only to the time derivative of the strain, as in equation 3.16, but also to the strain itself. This is possible if a second shear modulus is introduced, so that the mechanical response of the system is described by three parameters: η_s, G_{s1} and G_{s2}. Therefore, this model can be represented graphically as a spring connected in series with a parallel connection of a spring and a damper.

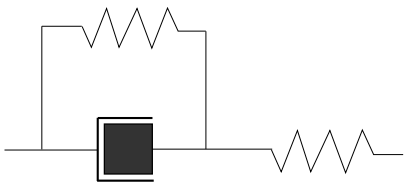

For the sake of simplicity, we consider a pure shear deformation:

$$\tau_1 \dot{\sigma}_s + \sigma_s = 2M_r(\gamma_s + \tau_2 \dot{\gamma}_s). \tag{3.23}$$

where

$$\begin{aligned} \tau_1 &= \frac{\eta_s}{G_{s1} + G_{s2}} \\ \tau_2 &= \frac{\eta_s}{G_{s2}} \\ M_r &= \frac{G_{s1} G_{s2}}{G_{s1} + G_{s2}} \end{aligned} \tag{3.24}$$

The solution of equation 3.23 for an oscillatory deformation, in analogy with the previous section, is used to obtain the interfacial shear moduli G' and G'',

$$\frac{G'(\omega)}{M_r} = \frac{1 + \tau_1 \tau_2 \omega^2}{1 + (\tau_1 \omega)^2} \tag{3.25}$$

$$\frac{G''(\omega)}{M_r} = \frac{(\tau_2 - \tau_1)\omega}{1 + (\tau_1 \omega)^2}. \tag{3.26}$$

whose frequency behaviors are reported in figure 7 for an hypothetical system characterized by $\tau_1 = 1s$ and $\tau_2 = 100s$. The presence of a second relaxation time introduces an inflection point in the frequency dependence of G', while leaving that of $G''(\omega)$ unaltered. The loss factor of the generalized linear solid model is

$$\tan(\delta(\omega)) = \frac{G''(\omega)}{G'(\omega)} = \frac{(\tau_2 - \tau_1)\omega}{\tau_1 \tau_2 \omega^2 + 1}. \tag{3.27}$$

Two crossovers are observed, from an elastic regime to a dissipative response, and back, at angular frequencies where the loss factor $\tan(\delta)$ is equal to unity, roughly correspondent to $\frac{1}{\tau_1}$ and $\frac{1}{\tau_2}$.

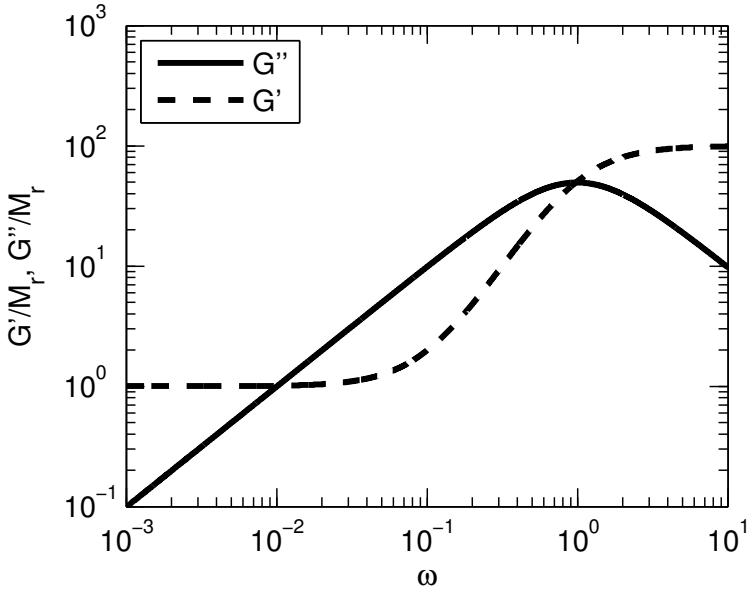

Figure 7: Generalized linear solid model of a viscoelastic film. Normalized shear moduli G' and G'' calculated for $\tau_1 = 1s$ and $\tau_2 = 100s$ from equations 3.26, reported as a function of the angular frequency ω.

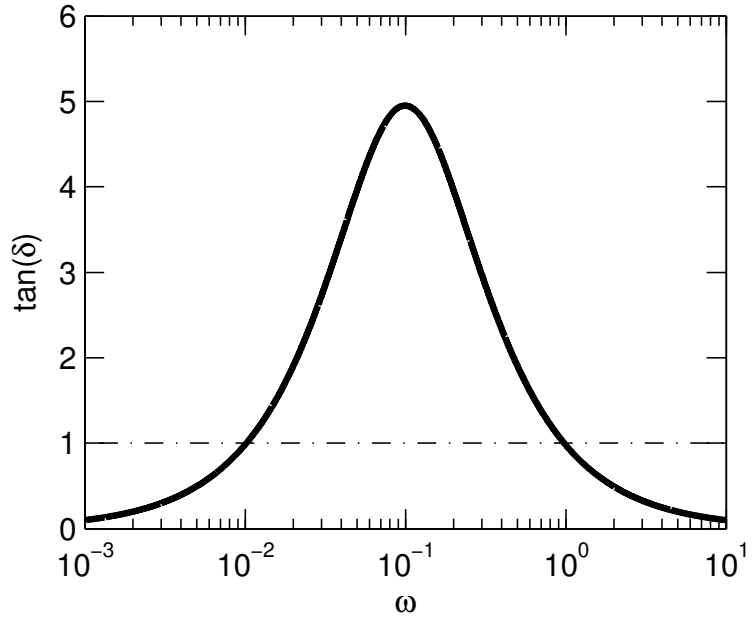

Figure 8: Generalized linear solid model of a viscoelastic film. Loss factor $\tan(\delta)$ calculated for $\tau_1 = 1s$ and $\tau_2 = 100s$ from equations 3.27, reported as a function of the angular frequency ω.

4 INTERFACIAL SHEAR RHEOLOGY

The measurement of the mechanical moduli -elastic and viscous- of an interfacial system may be performed directly, by measuring its response to an external deformation [45].

A complementary approach is based on the measurement on the fluctuations of the system, either by means of tracers embedded in the Langmuir film or by Dynamic Light Scattering (DLS) experiments, retrieving the mechanical moduli of the system using a GSE relation. This approach proves to be particularly useful for low-modulus films.

As stated here, the fluctuation-response function theorems provides the connection between the two approaches. A combined use of these complementary experimental methods to measure the dynamical moduli E and G could provide a more profound understanding of the system and of its behavior. In this work, the investigation is mainly focused on the measurement of the dynamical *shear* modulus G.

Given these consideration, rheological techniques are grouped into two categories, depending on the investigation approach they exploit:

- *active* rheology, when the film is stressed by an external force;
- *passive* rheology, when the probe investigates the fluctuations of the film to obtain information on its mechanical response.

Recently, many of these techniques, either active or passive, received a consistent gain in accuracy, resolution and operational range by the technological improvements in the fields of real-time data and image acquisition, e. g. the introduction of fast, high-resolution CCD cameras.

The *active* technique mainly used in this Thesis measures the interfacial shear modulus G using a magnetic needle, floating at the air/water interface, as an active probe. The presence of the film alters the motion of the needle. The film-induced damping and hindering are measured as function of the angular frequency of the oscillations. Other techniques, used during this project in addition to the oscillating needle techniques, are briefly described in chapter 5.

4.1 OSCILLATING NEEDLE SHEAR RHEOLOGY

An Interfacial Shear Rheology (ISR) apparatus that makes use of an oscillating magnetic rod was recently developed by the group of Gerald Fuller [46, 47]. The stress exerted by the needle on the film is equal to the shear oscillating force (with amplitude F), divided by two times the length L of the magnetic needle. The resulting shear strain γ is

equal to the needle oscillation amplitude X, divided by the distance W between the needle and the channel that delimits the investigated portion of the film. The oscillations of γ and σ are separated by a phase lag δ. The dynamic modulus is then given by:

$$G(\omega) = \frac{\sigma(\omega)}{\gamma(\omega)} = \frac{W}{2L}\frac{F(\omega)}{X(\omega)}e^{i\delta} \tag{4.1}$$

This experimental technique presents some limitations, related to its intrinsic design. A measurement performed on a film characterized by a low value of G may be strongly affected by contributions from the drag of the water subphase. At the same time, the technique is not suited to measure the response of very rigid films: the high force required to move the needle may induce undesired non-linear effects in the measurements of G.

The low limits of the dynamic range of the instrument is usually related to the so-called *Boussinesq number*, defined as the ratio between the drag due to the film at the interface, and the drag due to the subphase, that affect the movement of the needle at the interface. It is expressed as

$$B = \frac{d_{film}}{d_{subphase}} = \frac{\eta_s P L_b}{\eta_b A L_s} \tag{4.2}$$

where η_s and η_b are the viscosities of the film and of the subphase, A and P are the area and the perimeter of the contact region between the needle and the film, L_s and L_b are the lengths over which the velocity fields vary in the film and in the bulk. Depending on the value of B, three regimes can be roughly identified:

- if $B >> 1$, the effect of the subphase on the measurement of G are negligible;
- if $B << 1$, the needle is probing the flow properties of the subphase;
- an intermediate regime for $B \simeq 1$, where the interpretation of the measurement of the shear modulus G has to account in some way the contributions due to the drag of the subphase.

4.1.1 *Instrument design*

The interfacial rheometer we developed is an upgraded version of the instrument described by Fuller, adapted to the study of photosensitive polymers. A sketch and two photographs of the instrument are shown in figure 9.

The instrument is build around the Langmuir trough described in chapter 2. Two parallel glass plates, each of them 10cm long, define a channel used to constrain the needle position along the direction

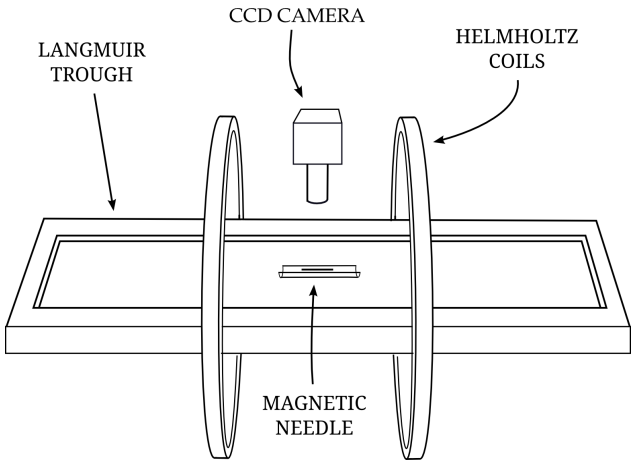

(a)

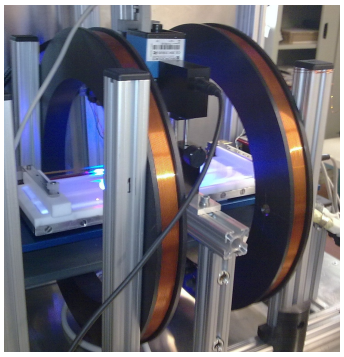

(b)

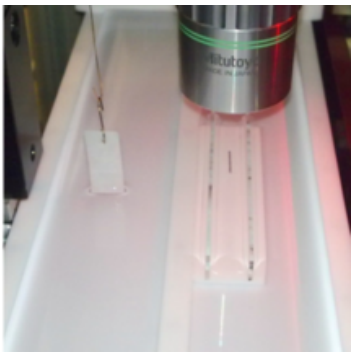

(c)

Figure 9: Sketch of the interfacial shear rheometer. a) simplified scheme of the interfacial rheometer; b) The interfacial shear rheometer implemented in Parma, seen from side; c) the magnetic rod floating at the air/water interface, between the glass plates.

parallel to the short edge of the trough. The stainless steel needle is typically 13mm long and has a diameter of 0.35mm; its surface is kept clean by immersion in chloroform. The needle is magnetized to saturation value before each experiment by contact with a permanent magnet.

Two coils in Helmholtz configuration (diameter $D = 32cm$, resistance $R = 7\Omega$) are placed around the Langmuir trough: each of them carries a static current $I_0 = 1A$. The static magnetic field generated by I_0 aligns the needle along the axis of the coils, as shown in figure 10a. The whole system is oriented parallel to the North-South direction, so the Earth field does not affect the alignment of the needle. A sinusoidal current is added to one of the coils, producing the oscillating field gradient that moves the needle. A typical sinusoidal wave of frequency $0.25Hz$ and amplitude $I = 1mA$ generates a force F of the order of $50nN$ on the needle, resulting in a displacement of about $10\mu m$.

This "two-coils" design is a simplification of the design originally proposed by Fuller and coworkers, which makes use of two coils in Helmholtz configuration to generate the static magnetic field, and two smaller coils in anti-Helmholtz configuration as the source of the oscillating magnetic gradient that moves the needle. In the following, we show that the use of two coils do not alter significantly the behavior of the oscillating magnetic field gradient, with respect to the one obtained with four coils.

We name x the distance from the center of the trough, along the axis of the two coils. Figure 10a reports the magnetic fields H_1 and H_2 generated by each coil -placed respectively at $x = -8cm$ and $x = 8cm$- and by the two coils in Helmholtz configuration. Close to $x = 0cm$, the total field H_{tot} is constant over x. When the oscillating current I is added to one coil, near to $x = 0cm$ the field H_{tot} grows linearly with x. If the needle, aligned parallel to the axis of the coils, is described as a magnetic dipole of momentum μ, the force exerted on the needle is given by

$$\overrightarrow{F}(x) = \overrightarrow{\mu} \times \nabla \overrightarrow{H}(x) \tag{4.3}$$

In the following, we consider only the component of the force parallel to the axis of the two coils. A calculation of the behavior of $F(x)$ for our instrument is shown in figure 10b. Close to $x = 0$, F is directly proportional to x: therefore, an elastic constant can be defined as

$$k = \frac{F(x)}{x}. \tag{4.4}$$

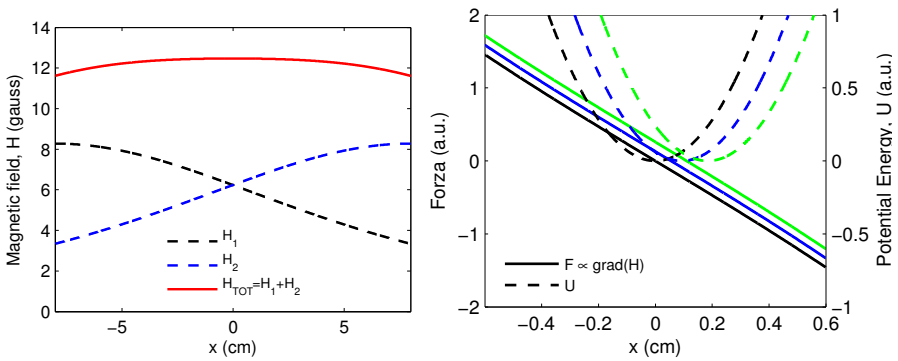

(a) (b)

Figure 10: a) magnetic fields generated by each coil, and by the two coils in Helmholtz configuration, as a function of the distance x from the center of the trough; b) The force $F(x)$ exerted on the needle (continuous lines) and the potential energy $U(x)$ (dashed lines) are reported for several values of the current I added to one of the two coils: $I = 0mA$ (black), $I = 3mA$ (blue), $I = 6mA$ (green).

Given this linearity, the energy of the dipole-field interaction $U(x)$ is parabolic in proximity of $z = 0$. The needle will change its position

accordingly to the position x_0 of the minimum of U. Since x_0 depends on the value of the oscillating current I, we have that

$$x_0 = Ae^{i\omega t}. \tag{4.5}$$

One may consider that, while in the four-coils configuration the value k is constant, this do no happen in a two-coils design.

The calculation reported in figures 10b and 11 shows the dependence of k over the current I is negligible in the present experimental setup; the relative variation of k reaches a maximum value of the order of 10^{-3}.

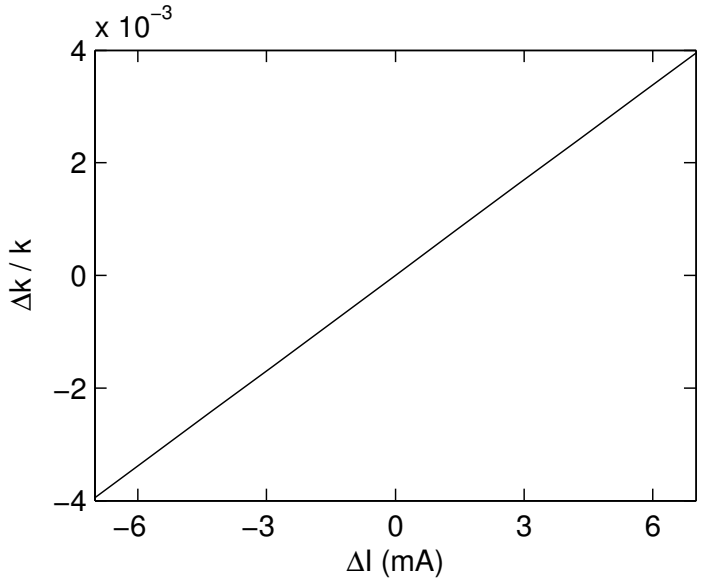

Figure 11: relative variation of the curvature k of the magnetic potential, as a function of the oscillating current added to one of the two coils.

The resulting displacement $d(\omega)$ of the needle -of the order of 50μm- is detected by a CCD camera[1] equipped with a long focal objective[2]. An hardware DAQ board[3] is used to control the instrument: using its analog outputs it is possible to drive the trough barriers and to apply the oscillating current to the Helmholtz coils via a set of power supplies. The DAQ analog inputs are used to measure the trough area, the surface pressure and the current on the coils as functions of time. Both the DAQ hardware board and the CCD camera are triggered by an external reference wave, oscillating at 14Hz. The external triggering is needed to properly measure the phase lag $\delta(\omega)$ between stress and strain, ensuring that the correct mechanical response is retrieved. A connection scheme of the experimental setup is sketched in figure 12.

1 The Imaging Source, 1024x768 pixels
2 Mitutoyo MPLAN-APO-20X
3 National Instruments PCI-6036e

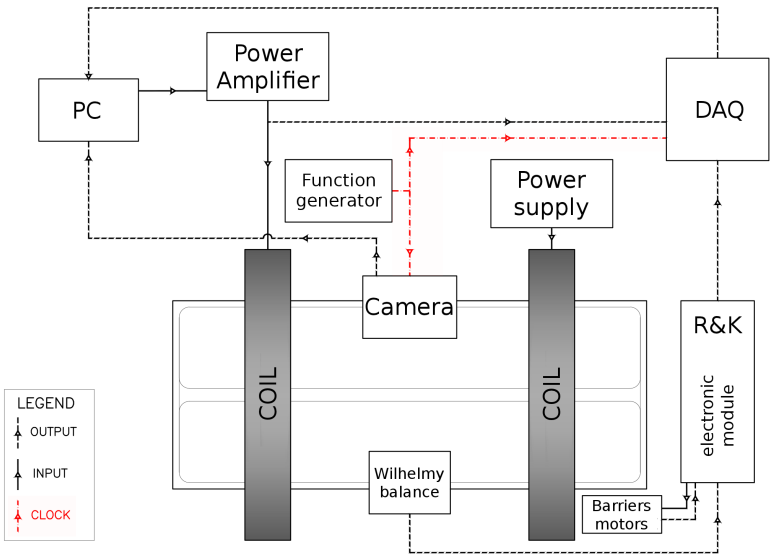

Figure 12: detailed sketch of the electrical connections of the experimental setup. The connections relative to the trigger signal are depicted in red.

4.1.2 *Calibration: oscillations on pure water*

In order to characterize the inertial response of the needle, we consider the oscillatory movement of the needle on a pure water surface. The total force exerted on the needle given by the composition of:

- a viscous drag force $F_c = -d\dot{x}$, where d is the drag coefficient for a motion parallel to the axis of the needle. If the needle is thin - its radius is much shorter than its length ($a << L$)- then the drag coefficient is given by a relatively simple expression [48]

$$d = \frac{2\pi\eta L}{\log\left(0.43\, L/l_0\right)} \tag{4.6}$$

  The drag coefficient d is then related to the water viscosity η, the needle length L and a characteristic length l_0 over which the two dimensional fluid velocity field can vary, which can be safely assumed to be of the order of the needle's radius a;

- an harmonic force originating from the interaction between the magnetic dipole of the needle and the magnetic field gradient generated by the system of coils,

$$F_m = -k\left(x - x_0\right) = -\frac{\partial^2 U}{\partial x^2}\left(x - x_0\right) \tag{4.7}$$

  where k is the elastic constant previously defined and U is the energy of the dipole-field interaction. The center x_0 of the har-

monic potential oscillates with angular frequency ω (see equation 4.5).

The resulting differential equation is

$$m\ddot{x} = -d\dot{x} - kx + kAe^{i\omega t} \tag{4.8}$$

Equation 4.8 is that of a forced-dumped oscillator of mass m, spring constant k and damping constant d [47]. The ratio AR of the amplitudes of the needle and force oscillation, and the phase lag δ result as:

$$AR = \frac{X}{kA} = \frac{1}{\sqrt{(k - m\omega^2)^2 + (\omega d)^2}} \tag{4.9}$$

$$\delta = \arctan\left(\frac{-\omega d}{k - m\omega^2}\right) \tag{4.10}$$

Commonly, instead of measuring the elastic constant k, the simpler approach of measuring the oscillatory voltage V applied to one of the two coils is preferred. Therefore, a calibration constant has to determined; in order to do that, the amplitude ratio $AR_V = \frac{X}{V}$ is measured. Observing the high-frequency limit of AR, it can be noted that it is proportional to ω^2 via the mass of the needle m.

$$\frac{X(\omega)}{F(\omega)} = \frac{X(\omega)}{\alpha V(\omega)} \to m\omega^2, \ \omega \to \infty \tag{4.11}$$

This relation -in analogy with [46]- allow the determination of the *calibration constant* α:

$$\alpha = \frac{1}{m\omega^2} \lim_{\omega\to\infty} \frac{X}{V} \tag{4.12}$$

A measurement of AR and δ is reported in figure 13 in logarithmic and semilogarithmic scale, respectively. While the mass m of the needle is measured, the oscillator parameters k and d were determined by a fit performed on the stress-stain ratio curve using equation 4.9; they are reported in table 1. The phase lag δ is in very good agreement with the model curve built from the parameters of table 1 (figure 13b) using equation 4.10.

k	$1.13 \cdot 10^{-5} N/m$
m	$9.9 \cdot 10^{-6} Kg$
d	$1.74 \cdot 10^{-5} Kg/s$

Table 1: Forced-dumped oscillator parameters that describe the response of the ISR needle on a pure water surface.

It is worth comparing the value of d obtained from the fit of the experimental curves with its theoretical value calculated using equation 4.6. If the characteristic length l_0 is taken equal to the needle's

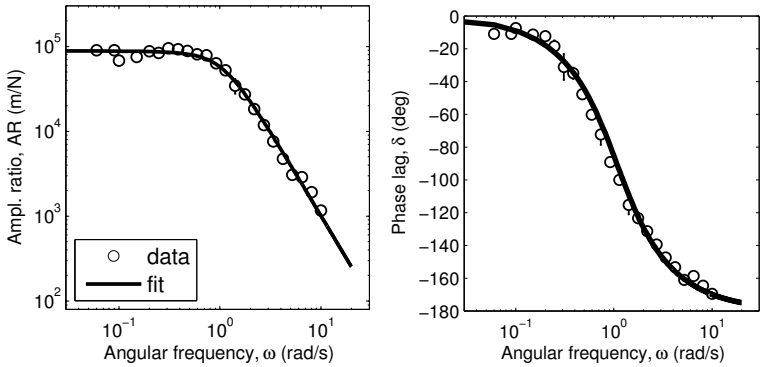

(a) (b)

Figure 13: ISR measurement on a pure water (Millipore) surface. The response is that of a forced-dumped oscillator. a) Amplitude ratio reported as a function of frequency (circles); the line is the fit with equation 4.9. b) Frequency dependence of the phase shift (circles), compared with the model curve obtained from equation 4.10.

radius a, we obtain $d_t = 2.38 \cdot 10^{-5} Kg/s$, with respect to the measured value of $1.74 \cdot 10^{-5} Kg/s$: the order of magnitude of the drag is correctly predicted.

4.1.3 *Oscillations in presence of a film*

The presence of a film at the air/water interface induces an additional hindrance of the motion of the needle, thus reducing the amplitude

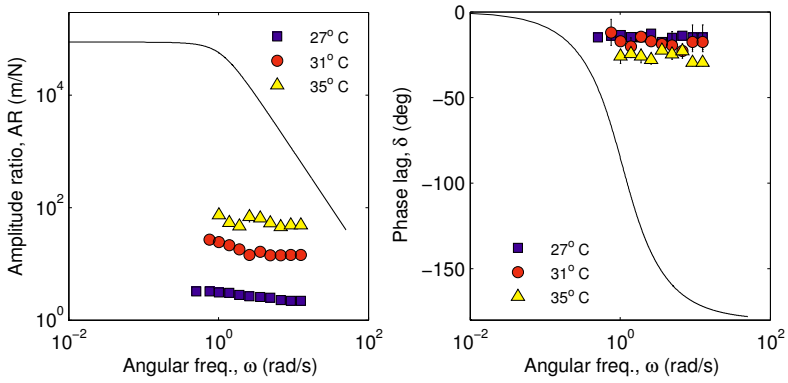

(a) (b)

Figure 14: ISR measurements on Langmuir films of a photosensitive azopolymer, performed for several values of the temperature. a) Force-needle position amplitude ratio, reported in log-log scale b) phase lag, reported in semilogarithmic scale. Experimental data are compared with the response measured in absence of a Langmuir film (continuous lines) obtained from the calibration measure of figure 13.

of its oscillations and modifying the phase lag between stress and strain. An example of the film-induced "extra-damping" is reported in figure 14 for films of a photosensitive polyacrylate.

An ISR measurement of the response of a Langmuir film can be considered meaningful is it is significantly different from the measurement performed in absence of film, which characterize the intrinsic oscillating behavior of the system. If this deviation is too small, than the measurement is likely to include huge effects due to the drag of the subphase.

As stated at the beginning of this chapter, the contribution to the drag due to the water subphase are negligible if the Boussinesq number B is high: $B >> 1$.

Usually, a so-called *experimental Boussinesq number* [46, 47]

$$B_{exp} = \frac{AR_{sys}}{AR_{film}} \tag{4.13}$$

is used in the literature to quantify the deviation of the response of the needle from the behavior observed on pure water. If $B_{exp} > 10 - 100$ in the frequency range investigated, then the mechanical response measured may be considered as not affected by hydrodynamic contributions due to the bulk of the subphase. In this case, the shear modulus G is given by

$$G(\omega) = \frac{W}{2L}\frac{\alpha V(\omega)}{X(\omega)}e^{i\delta} \tag{4.14}$$

If $B \simeq 1$, the subphase drag contribution to G has to be decoupled from the one due to the film. A simple way to decouple the contributions to G arising from the drag of the film and from the drag of the subphase, when the latter is not negligible, is to imply a linear relation between the two quantities [49, 47], so that

$$G_{film} = G_{meas} - G^*_{water} = G_{meas} - \frac{W}{2L}AR_w \exp(i\delta_w). \tag{4.15}$$

The accuracy of this procedure is questionable. In this work, the preferred approach consists in setting a confidence threshold value $B_{exp} = 10$, above which the measurement can be considered as not influenced by subphase drag contributions.

4.1.4 *Measuring the response of a Newtonian fluid*

An additional control of the instrument calibration is conducted measuring the response of films of poly(dimethylsiloxane) of controlled thickness d and known viscosity $\eta_{bulk} = 0.97 Pa \cdot s$. This oil has the mechanical response of an ideal (newtonian) fluid: it presents a purely viscous response with frequency-independent shear viscosity η_s.

In case of predominantly viscous systems, the generalized 2D viscosity η_{2D} is obtained from G through the simple relation:

$$\eta_{2D} = \frac{G''}{\omega}. \tag{4.16}$$

It is reasonable to assume that η_{2D} is proportional to the bulk viscosity through the thickness of the film, $\eta_{2D} = d \cdot \eta_{bulk}$, thus ignoring confinement effects.

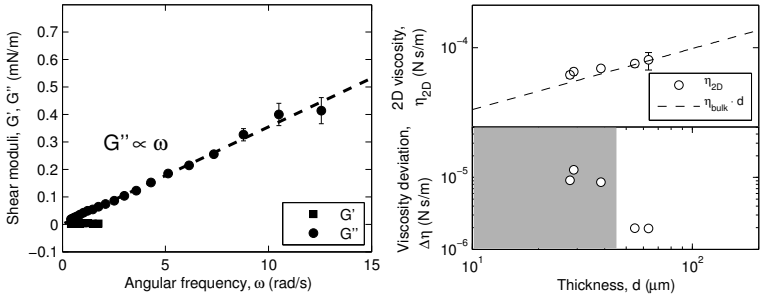

(a) (b)

Figure 15: ISR calibration measurement on a thin layer of oil - poly(dimethylsiloxane) - of known viscosity. a) loss and storage moduli G'' (circles) and G' (square) reported as a function of the angular frequency. The dashed line is a fit of G'' with a linear frequency dependence. b) Top: The 2D viscosity of polydimethilsiloxane oil films as a function of the thickness of the layer (circles). The dashed line represent the nominal value. Bottom: deviation of the 2D viscosity $\Delta\eta$ from the nominal value of the oil.

Data are shown in figure 15a: the film behaves as a Newtonian fluid with G'' (circles) growing linearly with the frequency, as indicated by fit represented by the dashed line, while G' is zero within the error. In figure 15b we compare the value of the viscosity η_{2D} obtained from G'' for each film thickness d with its expected value based on the bulk viscosity.

The results are consistent with the theoretical behavior for an ideal viscous fluid. However, careful inspection of the data from the lowest thickness ($d < 50\mu m$, represented by the gray area in the picture) shows a small deviation which can be ascribed to the drag due to the water subphase, which becomes comparable to that of the film when this becomes too thin. This effect has already been found and discussed in the literature [47]. If we suppose, in a simple approximation, a linear superposition of these effects, a rough estimate of the subphase drag is obtained: $|G|_{sub} \simeq 10\mu N/m$.

4.1.5 *Adaptation for photosensitive polymers*

The study of the mechanical properties of photosensitive polymers requires a proper adaptation of the instrument described so far. In particular, the instrument had to be enclosed in an aluminum box equipped with removable walls, to ensure that spurious light from the ambient does not influence the rheological properties of the film. Moreover, the illumination light required for the tracking of the needle's position has to be chosen in a spectral region where the sample is characterized by low absorbance. For the photosensitive azopolymers investigated in this work, red light ($\lambda > 630nm$) was chosen.

5

COMPLEMENTARY RHEOLOGICAL TECHNIQUES

Besides the *oscillating needle* technique, many other rheological techniques have been proposed and developed. In this chapter, we report a brief description of other rheological techniques.

Some of them used during this project. The measurements performed with these techniques were conducted in collaboration with dr. Pietro Cicuta, often using the experimental setups available at Cavendish Laboratory, Cambridge (UK).

5.1 OSCILLATING RING

The oscillating ring technique [50] makes use of the same general principles behind the oscillating needle technique, with some differences:

- the metallic ring probe is *directly* connected to the motor that induces its oscillations, and the ring oscillations are measured by means of optical or magnetic transducers;
- the probe oscillation is less prone to spurious influences, because of its mechanical connection to the motor. On the contrary, the oscillating needle movements could be influenced by parasitic magnetic fields;
- given the circular probe, a circular barrier with two small apertures is used to define the portion of the film whose mechanical properties are probed.

This instrument is a 2D implementation of the *coaxial cylinders (Couette) viscometer* [45, 51]. The equation of motion closely resembles eq.4.8 obtained for the oscillating needle interfacial rheometer:

$$I\frac{\partial^2\theta}{\partial t^2} + k\theta = T_{ext} - T_{film} - T_{water} \tag{5.1}$$

where I is the moment of inertia of the system constituted by the ring and its connections to the external motor, θ is the angular displacement, and the letter T indicate the torques exerted by the external motor, the Langmuir film and the water subphase. The mechanical response of the film is obtained from the extra damping of the oscillation induced by it, respect to the oscillatory response measured on pure water.

The oscillating ring viscometer used at the Cavendish Laboratory is a CIR-100 viscometer[1], depicted in figure 16a

1 Camtel, Royston, Herts, UK

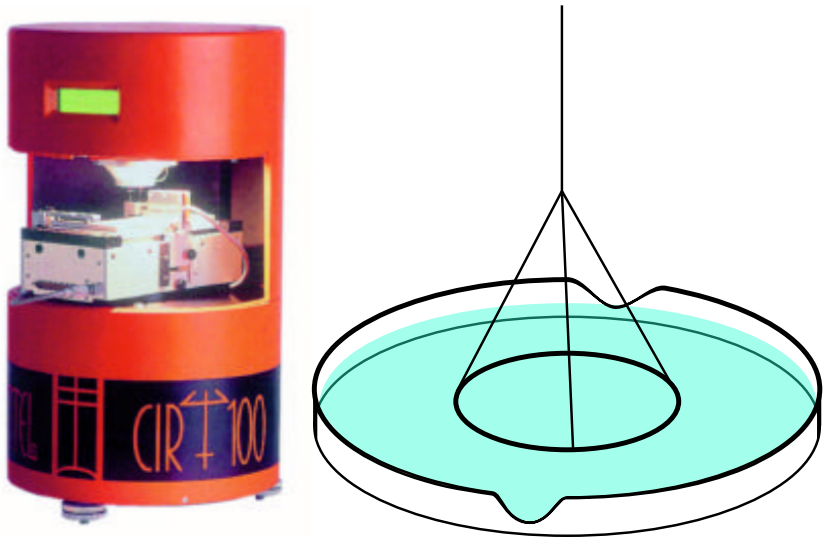

(a) (b)

Figure 16: Oscillating ring interfacial rheometer. a) CIR-100 rheometer from Camtel. b) Sketch of the probe floating on the film surface. The external ring defines the measurement area; it is characterized by two small apertures to allow the formation of the film inside the ring during compression.

Some disadvantages of this instrument are introduced by the external ring wall, necessary to clearly define the portion of film investigated and more specifically by its narrow apertures.

These apertures have to be small, so that the experimental geometry is unambiguously defined. When the film has a particularly high dynamic modulus, its rigidity obstacles its formation inside the ring during barrier compression. Then, the presence of the film in the measurement region has to be checked either by null-ellipsometry or, when this technique is not available, by placing a Wilhelmy plate inside the ring. The first solution is recommended, since the presence of a Wilhelmy plate inevitably modifies the response of the sample.

5.2 OSCILLATING BARRIERS

The oscillating barriers technique makes use of Wilhelmy balances to measure the response function to a mechanical stress induced by an oscillatory movement of the barriers of the Langmuir trough. This is done detecting the surface tension fluctuations over time [52, 53]. Since the compression induced by the movement of the barrier is uniaxial, the stress induced on the film is the linear composition of a dilational and a shear deformation. The compressional and shear moduli E and G can be measured at the same time by means of two Wilhelmy balances, placed respectively perpendicular and parallel to the barriers, as depicted in figure 17.

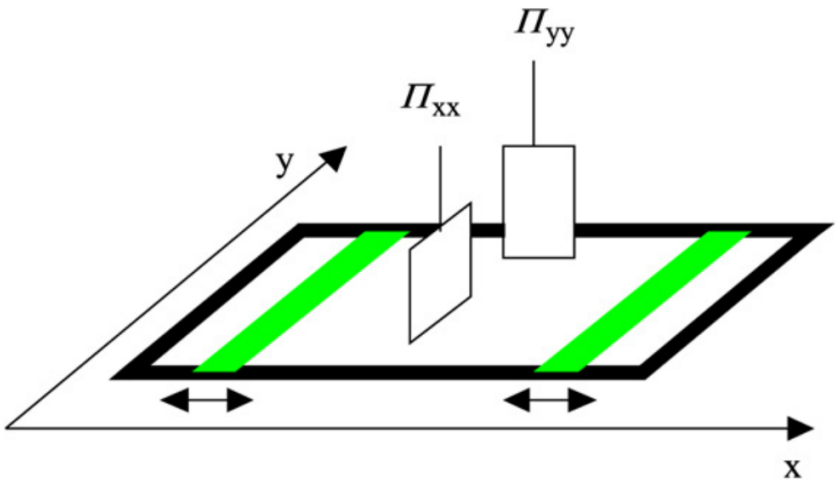

Figure 17: Sketck of the oscillating barriers apparatus, consisting in a Langmuir trough equipped with two Wilhelmy balances [53]. The barriers are drawn as green bars; Π_{xx} and Π_{yy} indicate the components of the surface pressure tensor respectively parallel and perpendicular to the barriers.

The first step consists in the formation of the Langmuir film at the desired surface pressure. At this point, a synchronized oscillation of the barriers position is induced, leading to a corresponding oscillation $\alpha = \log\left(\frac{A(t)}{A_0}\right) \simeq \frac{\delta A(t)}{A_0} = \frac{\Delta A}{A_0}\cos(\omega t)$ of the surface area. The components of the stress tensor are equal to the variation of the surface tension measured by the two Wilhelmy balances [54];

$$\begin{aligned}\sigma_x x &= \Pi_{xx} - \Pi_0 = (E + G_s)\alpha + (\eta_c + \eta_s)\dot{\alpha} \\ \sigma_y y &= \Pi_{yy} - \Pi_0 = (E - G_s)\alpha + (\eta_c - \eta_s)\dot{\alpha}\end{aligned} \tag{5.2}$$

where Π_{xx} and Π_{yy} indicate the components of the surface pressure tensor respectively parallel and perpendicular to the barriers. Therefore, if the amplitude of the oscillations of Π_{xx} and Π_{yy} is measured, along with their phase lag θ with respect to the oscillations of the area, both the compression and shear dynamic moduli ϵ and G can be retrieved [52, 53, 54]:

$$\epsilon = \epsilon' + i\epsilon'' = \frac{A_0}{2}\left(\frac{\Delta\Pi_{xx}}{\Delta A} + \frac{\Delta\Pi_{yy}}{\Delta A}\right)e^{i\theta} \tag{5.3}$$

$$G = G' + iG'' = \frac{A_0}{2}\left(\frac{\Delta\Pi_{xx}}{\Delta A} - \frac{\Delta\Pi_{yy}}{\Delta A}\right)e^{i\theta} \tag{5.4}$$

This technique works well if the film is characterized by relatively high compressional and shear moduli. Other problems could arise from the formation of aggregates and collapses that may be induced by the movement of the barriers.

5.3 CANAL VISCOMETER

The measurement of the steady mechanical response of viscous films can be conducted using the so-called *canal viscometry*. The viscosity of the film is measured from the study of the flow of the sample through a small channel. This flow is compared with a solution of the *Navier-Stokes* equations calculated from the channel geometry.

The experimental setup consists in a Langmuir trough divided into two separate portions of area A, connected by a teflon channel; one of the two portions is equipped with a single moving barrier.

The viscous film is formed, at the same value of surface pressure, on both sides of the separation barrier; Π is measured by two Wilhelmy balances. Then, a *constant surface pressure gradient* $\Delta\Pi$ is induced by a steady compression of the film on one side, obtained with the movement of the barrier [55]; this induces a flow of material $Q = \Delta A/\Delta t$ towards the portion of trough where Π is lower.

Calling W, L and Z the width, length and depth of the channel, in the limit case $D >> W$, the Navier-Stokes equations reduce to

$$\eta_s = \frac{\Delta\Pi\, W^3}{12\, L\ \Delta A/\Delta t} - \frac{W\,\eta_w}{\pi} \tag{5.5}$$

where η_w is the water viscosity. This equation is valid for film characterized by a viscosity $\eta_s > 10^{-4} g/s$. The flow profile of the film can also be observed by means of epifluorescence microscopy of fluorescent probes embedded in the film, or by means of Brewster angle Microscopy of Null-ellipsometry in imaging mode.

The measurements performed with this experimental setup are affected by severe problems of low reproducibility of the results. the technique induces collapses and formation of aggregates in the film, as a consequence of the steady compression through the channel.

5.4 MULTIPLE PARTICLE TRACKING

MPT investigates the rheological properties of a Langmuir monolayer measuring the 2D MSD $\langle r^2(t)\rangle$ of micron-sized spherical particles embedded into it. Therefore, the technique implies that a fluctuation-response function relation holds for the system investigated, in form of a generalized *Einstein Stokes* relation. Since it make use of *micron* and *sub-micron* particles as passive probes, MPT is categorized as a *microrheological* technique: P. Cicuta and A. Donald wrote a brief but complete review [35] of this class of techniques. The main advantages of MPT is the high sensitivity, allowing the measurements of the rheological properties of low-module expanded phases of langmuir monolayers. The position of the beads is tracked over time using an inverted microscope, equipped with an adapted Langmuir trough and a CCD camera. A calibration measurement is reported in figure 18:

it is performed following the motion of silica particles at the air/water interface. In this situation, the mean square displacement grows linearly with the experimental time. The correct value of 1cP for water viscosity is calculated from the diffusion coefficient D via the 2D Einstein relation

$$D = \frac{\langle r^2(t) \rangle}{4t} \tag{5.6}$$

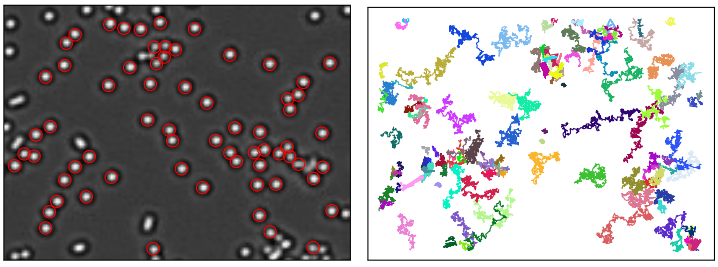

(a) (b)

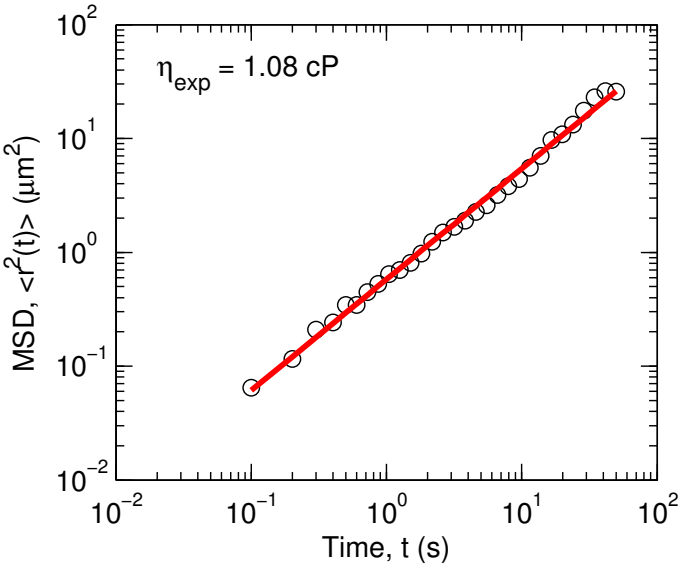

(c)

Figure 18: Calibration measurement of the multiple particle tracking algorithm, performed by tracking silica beads (2.5μm diameter) on a pure water surfaces. a) microscopy image of the particles. Tracked beads are evidences in red; b) Particle trajectories; c) Correspondent MSD as a function of time (circles). The red line is a linear fit ($< r^2 > \propto t$) of the data: the value of 1cP for water viscosity is correctly measured.

The MSD $\langle r^2(t) \rangle$ is calculated via software from the digitalization of the trajectories of the particles; then, the generalized Einstein-Stokes

relation proposed by Mason and Weitz [56] and discussed before is used to obtain the frequency-dependent dynamic shear modulus G:

$$\left\langle \Delta\tilde{r}^2(s) \right\rangle = \frac{2k_B T}{3\pi a s \tilde{G}(s)} \tag{5.7}$$

where s is the Laplace frequency, where s is the Laplace frequency, and $\left\langle \Delta\tilde{r}^2(s) \right\rangle$ and $\tilde{G}(s)$ are the Laplace transforms of $\left\langle r^2(t) \right\rangle$ and $G(t)$. As stated by equation 5.7, the measurement of G requires the determination of the Laplace transform of the MSD; then, the shear modulus is obtained as $G(\omega) = \widetilde{(}G)(s = \omega)$. The calculation of the Laplace transform of $\left\langle r^2(t) \right\rangle$ is often performed as a transform of an analytical form used to fit the experimental data. This procedure presents several disadvantages:

- since it is possible to calculate the analytic Laplace transform of few functions, the experimenter choices are reduced; often, an excessive number of parameters is introduced to adapt the fit to the experimental data;
- it implies an extrapolation of $\left\langle r^2(t) \right\rangle$ at short and long times, where experimental data are not accessible, that heavily affects the resulting $\tilde{G}_s$.

A recent procedure, proposed by Evans et al. [57], provides a straightforward numerical determination of the dynamic shear modulus from the compliance $J(t) = \frac{k_B T}{\pi a} < r(t)^2 >$, where T is the temperature and a is the radius of the particles. This procedure does not hide the experimental noise and at the same time it reduces the risk of biased extrapolation of the dynamic shear modulus. Having measured a set of experimental points $(t_i > 0, J_i)$, the dynamic shear modulus is given by the relation

$$\frac{i\omega}{G(\omega)} = i\omega J(0)\left(1 - e^{-i\omega t_1}\right)\frac{J_1 - J(0)}{t_1} + \frac{e^{-i\omega t_N}}{\eta} + \\ + \sum_{k=2}^{N}\left(\frac{J_k - J_{k-1}}{t_k - t_{k-1}}\right)\left(e^{-i\omega t_{k-1}} - e^{-i\omega t_k}\right) \tag{5.8}$$

It is worth noting that the determination of the asymptotic behavior of the compliance $J(0)$ at $t = 0$ is not hidden in the choice of an analytic form to fit $J(t)$, but it is now explicit, along with the indication of the value of the suspension viscosity η, the parameter that defines the slope of the compliance at long times. Furthermore, this expression finds application not only in MPT, but in any compliance measurement performed with any rheological technique.

6 CRITICAL DISCUSSION

The brief descriptions of the rheological techniques detailed in the previous chapters did not include a discussion of the several approximations present in the models used for the interpretation of the measurements. This is particularly relevant for the interpretation of measurement of mechanical moduli whose value fall close to the limits of the resolution of each technique.

A discussion of these approximation is given in this chapter, and it is valid, with minor modifications, for all the techniques detailed before.

A. The first a priori assumption is that of a *non-slip* contact between the probe and the sample; the slip may compromise the reproducibility of the measurements, and it could even induce damage on brittler films.

B. Another approximation consists in the assumption that the surface in the measurement area is flat. This assumption could not be accurate for the experimental techniques, such as the oscillating needle/ring techniques, where the measurement area is limited by hydrophilic walls. The requirement of a large measurement area, so that water surface is flat, is in competition with the fact that a small measurements area, e. g. a thin channel in the oscillating needle technique, increases the sensitivity range of the instrument.

C. The contact angle c between the probe and the surface is assumed to be equal to 90°; an higher value of c imply higher contributions to G due to subphase drag, while a lower value may compromise the non-slip contact with the film [58].

6.1 DEPENDENCE ON THE CONTACT ANGLE

The approximation of contact angle $c = 90°$ has relevant effects in MPT experiments. Models are needed to correct the measurement of the diffusion coefficient D to account for contributions to G due to $c \neq 90°$ and to gradients of surface pressure.

In particular, two different models of the drag coefficient of micron-sized particles embedded in a Langmuir film have been formulated, both accounting for different values of the contact angle. The two models are formulated respectively for *compressible* and *incompressible* films.

The model for the motion of particles embedded in compressible films was developed by Danov and coworkers [59], with the approximations that the contact angle does not change during the measurements and that the movement of the particles happens at low Reynolds numbers.

In a viscoelastic film the presence of Marangoni forces, due to local gradients of surface pressure, hinder any motion that compresses/-expands the film. In this situation, the behavior of the film is closer to that of an incompressible fluid. Fisher and coworkers proposed a model for particle diffusion in an incompressible fluid that accounts for contributions to the drag of the film due to Marangoni forces [60]. The model calculates the dimensionless drag coefficient d_f that relates the drag force due to the film to the particle velocity in a generalized Navier-Stokes equation for 2D films:

$$F_d = d_f \eta R v \tag{6.1}$$

d_f is expressed as a series expansion in terms of the Boussinesq number, where the coefficients depend on the radius of the particle and on their contact angle with the film surface.

6.2 MACRORHEOLOGY OR MICRORHEOLOGY?

In order to increase the accuracy of the measurements, it is relatively common to perform experiments using several rheological techniques, and in particular using active and passive rheology. Active rheology usually makes use of *macroscopic* probes (ring or needle), while in passive technique like MPT the probes are *microscopic* tracers.

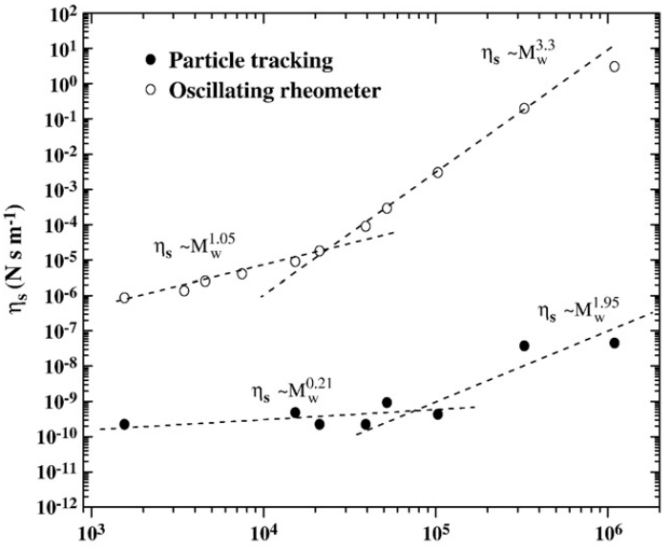

Figure 19: Surface shear viscosity for monolayers of poly(t-butyl acrylate) as a function of the molecular weight and for a surface pressure of $\Pi = 16 mN/m$.

Hoverer, the literature report several cases of huge differences - orders of magnitudes- in the dynamical shear moduli measured using macro or microrheology: an example of this discrepancy was reported by Ortega and coworkers [58] for films of poly(t-butyl-arylate) of different several weights. As shown in figure 19, the MPT experiments measured a dynamic shear modulus G that is from 4 to 8 orders of magnitude lower than the modulus measured with the oscillating ring technique.

This difference is still unexplained. It may be related with the microscopic size of the probes; their motion may couple with the microscopic domains that may characterize the morphology of the system.

Part III

MICROSCOPIC SPONTANEOUS FLUCTUATIONS

Introduction to the fundamental theory and the experimental setups behind the measurements of the slow internal fluctuations at the interface, by means of X-ray Photon Correlation Spectroscopy. The characterization of dynamical heterogeneities by means of higher order correlation functions is highlighted.

7

DYNAMICAL FLUCTUATIONS

The internal dynamics of a system, either in 2D or 3D, can be measured by means of a light scattering experiment. In order to do so, the incident light has to show a sufficiently high *degree of coherence* in the longitudinal and in the transverse directions. In general, the degree of coherence of radiation is expressed as *coherence lengths*.

The longitudinal coherence, necessary also for "static" scattering experiments, is linked to the monochromaticity of the light wave the photons have to be linked by a precise phase relation. The coherence length in the transverse directions, on the contrary, is defined as the length that separates two point on the detector that measure signals that are not cross-correlated, following Berne and Pecora [8]. This length is related to the experimental setup, in particular to the size of the light source. Transverse (l_t) and longitudinal (l_l) coherence length are related to the experimental parameters by means of the following expressions:

$$\begin{aligned} l_t &= \frac{\lambda R_s}{2\, d_s} \\ l_l &= \frac{\lambda^2}{2\, \delta\lambda} \end{aligned} \tag{7.1}$$

where λ is the wavelength, $\delta\lambda$ the width of the wavelength distribution, R_s the detector-source distance and d_s is the source size. The transverse coherence area can be expressed as

$$A_{coh} = \frac{\lambda^2}{\Omega} \tag{7.2}$$

where Ω is the solid angle subtended by the light source at the detector.

Coherent sources of visible light (lasers) are commonly available in laboratory. Intrinsically transverse coherent X-ray source, on the contrary, are still not available. If a transversely incoherent monochromatic beam is focused on a pinhole of size comparable to the transversal coherence area, the pinhole can be approximated as a point source of coherent light. This focusing procedure discards a relevant fraction of photons, so a consistent photon flux is compulsory.

Coherent radiation scattered from a disordered sample result in a random diffraction pattern. It is due to interference of many waves with different phases, originating from independently moving regions of the sample in the scattering volume. This random diffraction pattern, recorded at fixed exposure time, fluctuates over time. Since the

speckle pattern reflects the internal dynamics of the sample, the characteristic times that govern its temporal fluctuations corresponds to the relaxation times of the dynamics of the sample itself.

To access the information on the microscopic dynamics of the sample contained into the scattered intensity, the experimental setup as to be arranged so that the coherence area is comparable with the area of the detector employed [61]. The use of transversely incoherent light would lead to an averaged diffraction pattern, with consequent loss of information.

Figure 20 shows the X-ray diffraction pattern measured on a colloidal suspension of poly(methylmetacrylate) particles, with radius $R = 90nm$. The black shadow is due to a beam stopper element introduced to block the direct beam from damaging the detector. The diffraction pattern shows spherical symmetry because the sample is isotropic; anyhow, the intensity detected by pixels equidistant from the center of the diffraction pattern fluctuates spatially and over time. The pattern is characterized by rings with lower intensity as the distance from the center is increased. These rings result from the form factor of spherical particles: the distribution of size of the particles in the colloidal suspension is deduced from the ring positions and widths.

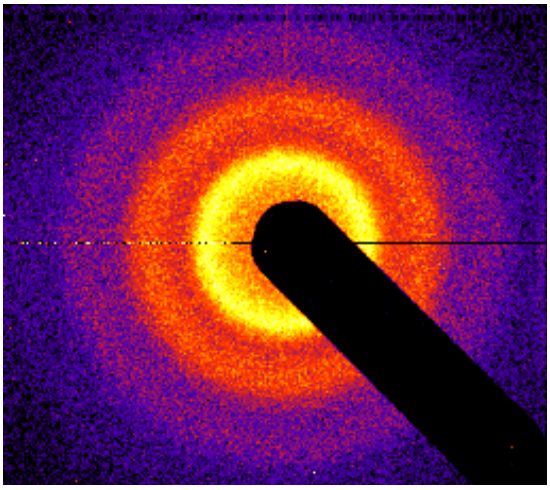

Figure 20: X-ray diffraction pattern of an high concentration colloidal suspension of hard PMMA spheres [62], characterized by the presence of speckles.

Autocorrelation and cross-correlation functions of the scattered intensity are powerful tools to perform the analysis of the temporal fluctuations of the speckle pattern: a concise description of their calculation and interpretation is reported in the following sections.

7.1 INTENSITY-INTENSITY CORRELATION FUNCTION

An intensity-intensity correlation function is calculated as the probability that an intensity I has been recored at time t, given that an intensity I_0 was recored at time t_0. This correlation function investigate the second-order coherence of light, the autocorrelation of the electromagnetic field's amplitude investigates the first-order coherence. The normalized autocorrelation function of intensity is then defined as:

$$g^{(2)}(q,t) = \frac{\langle I(q,t_1)I(q,t_1+t)\rangle_{t_1}}{\langle I(q,t_1)\rangle^2_{t_1}}. \tag{7.3}$$

We underline that equation 7.3 calculates a time-averaged correlation function, while in statistical physics we usually deal with ensemble-averaged correlation functions. The two are equivalent only if the system is ergodic. The calculation of correlation functions is usually performed by means of fast multiple-tau algorithm, implemented either as hardware electronics or software. In general, such algorithms require a good statistic to reach a sufficiently high signal-to-noise ratio. This can be achieved either by a long measurement time, or by employing an higher number of detectors, placed at the same q (by means of CCD cameras). The short and long time limits of the numerator of $g^{(2)}(q,t)$ are

$$\lim_{t\to 0} \langle I(q,t_1)I(q,t_1+t)\rangle_{t_1} = \left\langle I^2(q,t_1)\right\rangle_{t_1} \tag{7.4}$$

$$\lim_{t\to \infty} \langle I(q,t_1)I(q,t_1+t)\rangle_{t_1} = \langle I(q,t_1)\rangle^2_{t_1} \tag{7.5}$$

Thus, $g^{(2)}(q,t)$ tends to unity at long times, while at short times it approaches $1+\beta$, where β, called "optical contrast", is the variance of intensity fluctuations divided by the mean intensity. In general, the contrast depends on the experimental setup, and is affected also by the characteristics of both the sample and the detector.

We consider a sample composed by an high number of "domains" that moves separately in the scattering volume. In this situation, the electric fields scattered by each region are independent random variables, and so their sum if the *central limit theorem* is valid; then, the statistics is described by a *Gaussian* distribution. It is possible to demonstrate that, in this conditions, a very simple relation holds:

$$g^{(2)}(q,t) = 1 + \beta \left| g^{(1)}(t) \right|^2 \tag{7.6}$$

Here, $g^{(1)}(q,t)$ is the first-order correlation function, the autocorrelation function of the scattered electric field:

$$g^{(1)}(t) = \frac{\langle E^*(t_1)E(t_1+t)\rangle_{t_1}}{\langle E^*(t_1)E(t_1)\rangle_{t_1}}. \tag{7.7}$$

The condition of "Gaussian statistic"is commonly assumed; however, it may not be valid anymore if the number of independently moving regions in the scattering volume is too low.

It can be shown also that $g^{(1)}(q,t)$ is the normalized *intermediate scattering function* [63]

$$g^{(1)}(q,t) = \frac{S(\vec{q},t)}{S(\vec{q},0)} \tag{7.8}$$

where $S(\vec{q},0)$ is the static structure factor and $S(\vec{q},t)$ the intermediate scattering function or dynamic structure factor.

$S(\vec{q},t)$ is given by

$$S(\vec{q},t) = \frac{1}{Nf^2(\vec{q})} \sum_n \sum_m \left\langle f_n(\vec{q}) f_m(\vec{q}) e^{i\vec{q}[\vec{r}_n(0)-\vec{r}_m(t)]} \right\rangle \tag{7.9}$$

where the brackets indicate an ensemble average over the scattering amplitudes $f_n(\vec{q})$. The calculation from first principles of $S(\vec{q},t)$ using equation 7.9, starting from the characterization of the microscopic structure of the sample, leads to analytical models of $g^{(2)}(q,t)$ that can be used for the interpretation of experimental data.

7.2 BASIC PHENOMENOLOGY

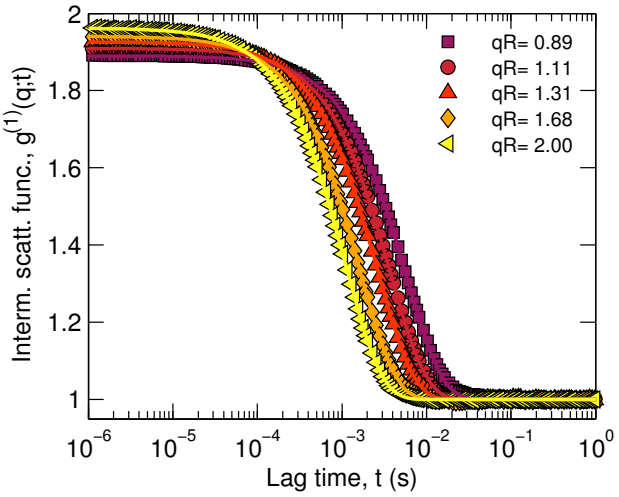

Figure 21: Correlation functions $g^{(2)}(q;t)$ measured by DLS on a low concentration suspension of PMMA particles ($R = 90nm$) [62]. Continuous lines are fits with equation 7.11

As a first example, we report the analytical prediction of $g^{(2)}(q;t)$ for particles drifting at constant velocity in a viscous fluid (ballistic motion). The a-priori calculation of the normalized dynamic structure factor leads to an exponential form for the correlation function,

$$g^{(2)}(q,t) = 1 + \beta \left| \frac{S(\vec{q},t)}{S(\vec{q},0)} \right|^2 = 1 + \beta e^{-2\left(\frac{t}{\tau(q)}\right)^2} \tag{7.10}$$

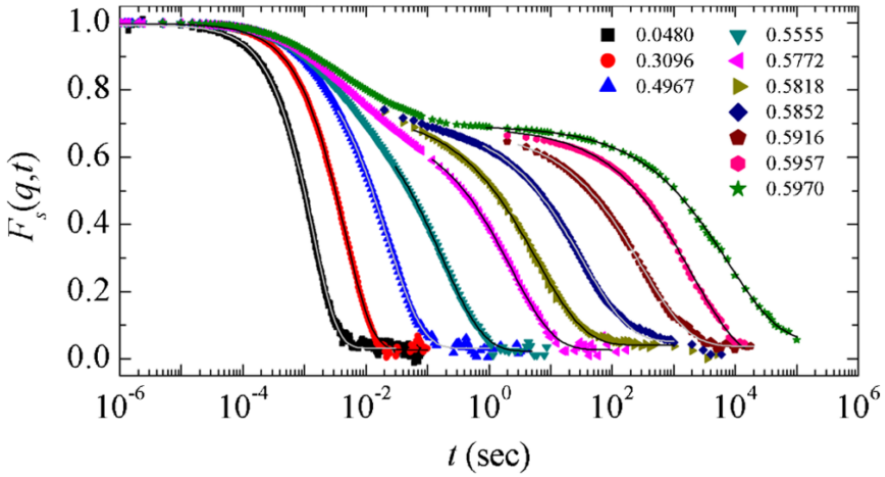

Figure 22: Intermediate scattering function measured by DLS on an highly concentrated suspension of PMMA particles ($R = 260nm$), as a function of concentration [64, 65].

with the relaxation time proportional to the exchanged momentum q: $\tau(q) \propto q^{-1}$.

A second example consists in the analytical form of $g^{(2)}(q;t)$ for a low-concentration colloidal suspension of monodisperse spherical particles under Brownian motion. In this case, the ensemble averages non-diagonal terms of equation 7.9 are equal to zero, because of the negligibility of interparticle interaction. Moreover, the displacement $[\vec{r}_n(0) - \vec{r}_m(t)]$ of each particle is a Gaussian variable whose mean square value is given by Einstein's relation for Brownian motion, $\langle r^2(t)\rangle \propto D_0 t$, proportional to the diffusion coefficient.

Combining these consideration with equations 7.6, 7.8 and 7.9, the second-order correlation function can be expressed in the form

$$g^{(2)}(q,t) = 1 + \left|\frac{S(\vec{q},t)}{S(\vec{q},0)}\right|^2 = 1 + \beta e^{-2D_0 q^2 t}. \tag{7.11}$$

An example of the measurement of Brownian dynamics using correlation functions is shown in figure 21; it reports $g^{(2)}(q;t)$ measured at several values of q on a low concentration colloidal suspension, in a DLS experiment.

This simple expression does not hold anymore when interparticle interaction are not negligible anymore. For instance, this happens in highly concentrated suspensions of hard spheres, where hydrodynamic interactions play a significant role in determining the dynamical arrest as the glass transition approaches. Below a critical temperature T_c the Mode Coupling Theory predicts [66, 67] (and experiment finds) the presence of two relaxation times: t_β, the relaxation time relative to the rattling of the particles inside the "cage" formed by the neighbor particles, and t_α, the time over which these cages relax.

An example of this double-time decay reported in the literature [64, 65] is shown in figure 22: the correlation functions were measured on a high concentration PMMA suspension by means of DLS. In this situation the decay of the correlation function is described by a double exponential, characterized by two q-dependent diffusion coefficients $D_s(q)$ and $D_l(q)$, for the short- and long-time relaxations:

$$g^{(1)}(q,t) = Ae^{-D_s(q)q^2t} + (1-A)e^{-D_l(q)q^2t}, \tag{7.12}$$

that correspond respectively to the β and α relaxations predicted by the mode-coupling theory for the glass transition.

The double-time decay of $g^{(1)}(q,t)$ was also observed by us [62] by means of X-ray Photon Correlation Spectroscopy (XPCS), and it is displayed in figure 23. Several suspensions of sterically stabilized PMMA nanoparticles (90nm) - interacting with an hard-sphere repulsive potential- in cis-decalin were prepared, with concentration ranging within $\Phi = 11\%$ and $\Phi = 50\%$. Correlation functions were measured for several values of q; at low concentration $g^{(1)}(q,t)$ decay as a simple exponential, while at high concentration a second relaxation time is observed. Morevoer, in high concentration colloids the diffusion coefficients are not constant over q anymore. The q-dependence of the diffusion coefficients is related both to the static structure of the suspension and to the hydrodynamic interactions.

When studying arrested systems -as polymeric systems, gels or glasses- characterized by soft or even weakly-attractive interaction potentials, the increase of concentration (or a decrease of the temperature) may lead to arrested states. In this case, the exponential decay of the correlation functions assume a more complex behavior, which

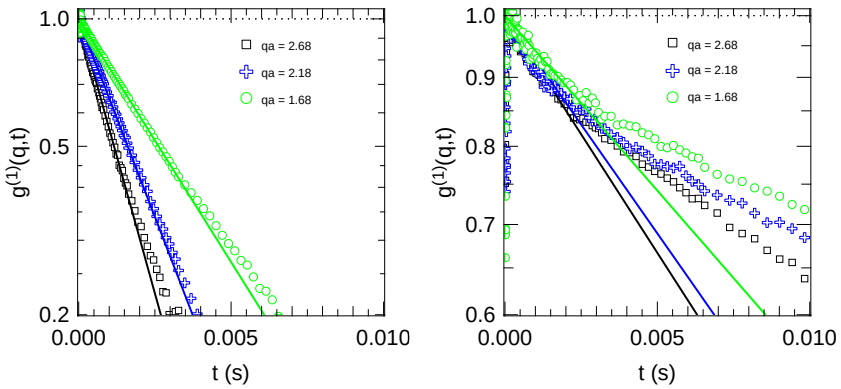

Figure 23: correlation function $g^{(1)}(q,t)$ measured on two colloidal suspension of PMMA particles ($R = 89nm$) in cis-decalin, at volume fraction a) 11% and b) 50% [62].

is usually empirically described in the literature using the Kolraush-William-Watts (KWW) functional form:

$$g^{(2)}(q,t) = 1 + \beta e^{-2(t/\tau)^{\gamma}} \tag{7.13}$$

Here γ is often called *compression exponent*. In this case, particular care has to be paid into the investigation of the q-dependencies of γ, β and τ. On the other hand, an exponent $\gamma < 1$ is commonly associated with the presence of a distribution of relaxation times, in a generalization of equation 7.12.

A $\tau \propto q^{-1}$ scaling, accompanied by compressed exponential decays (i.e. $\gamma > 1$) has been measured by XPCS in a wide variety of materials [26], including both colloidal gels [68, 69, 26] and repulsive compact arrangements of soft elastic spheres [70], emulsion droplets [71], and Laponite [72] systems.

The $\tau \propto q^{-1}$ scaling suggests that the slow dynamics may be of ballistic nature, in the sense that the average MSD grows as time squared. It has been proposed [68, 70, 71] that the dynamics could be due to randomly distributed stress sources within the sample, whose response mimics that of an elastic solid. The origin of this dynamics has been related, in colloidal samples, to a series of intermittent rearrangement of larger or smaller volumes [26]. The size of these volumes may be estimated by some "crossover" exchanged momentum q at which the compression exponent γ varies from 1 to 1.5; however, the situation is much less clear for polymeric systems. These results, in particular the $\gamma > 1$ compressed exponentials, are somehow unexpected, as one would imagine a stretched -slower than exponential- decay for a system undergoing dynamical arrest.

Another model that better describes the results experimentally found during this project is described in the following section.

7.3 THE BOUCHAUD-PITARD MODEL

A model proposed by J.-P. Bouchaud and E. Pitard [73] calculates the dynamic structure factor of a generic elastic solid characterized by micro-collapses appearing randomly -in both space and time- in the system structure. These collapses generate mechanical force dipoles. In an ideal elastic colloidal gel sample, the structure of the system rearranges locally when particles tend to collapse one against each other, generating a field of mechanical stresses.

The model predicts that correlation functions describing the rearranging dynamics of this system decay as compressed exponentials, with compression exponent $\gamma = 1.5$, when the relaxation time τ is much faster than the time scales of the collapses θ. For larger values of τ a decay of the compression exponent to $\gamma = \frac{5}{4}$ is predicted by the model. This dependence of the compression exponent is accompanied by a linear proportionality of the relaxation time τ to the

inverse of the exchanged momentum - $\tau \propto q^{-1}$, while on the contrary $\tau \propto q^{-2}$ for Brownian motion. A similar behavior has been found in a variety of arrested systems [26], e.g. in oil nanoemulsion [74], in aqueous colloidal polystyrene gels [68],

As stated before, the model is build considering an elastic bulk solid, characterized by a compressional elastic modulus. An interesting proportionality between the relaxation time and the elastic modulus,

$$\tau \propto E$$

is predicted for the slow dynamics of the sample. The article of Bouchaud and Pitard imply that analogous results should hold even for a system characterized by an elastic *shear* modulus, though a theoretical demonstration of this conclusion is not given.

7.4 HIGHER ORDER CORRELATION FUNCTIONS AND HETEROGENEOUS DYNAMICS

In recent years, research has been focused on the investigation of the dynamics of disordered soft systems, like foams, concentrated colloidal suspensions of hard and soft spheres. The correlation functions measured by XPCS experiments on these samples usually differ from the simple exponential behavior observed in Brownian dynamics. The dynamics is often not stationary, characterized by aging processes that slow down the dynamics toward arrest. Moreover, the internal fluctuations of the systems may present dynamical heterogeneities [75, 26], like distinct domains showing different dynamical regimes or avalanche-like rearranging events.

Higher order correlation functions offer a tool to investigate the complex dynamics of disordered systems,in which dynamic properties change in time, with the sample undergoing a process of aging, where the temporal invariance is broken. Information on such complex aspects of the dynamics is unavailable with an approach that involves only intensity autocorrelation functions. This new approach has been made possible thanks to the development of fast and accurate 2D array of detectors, like CCD for DLS experiments.

7.4.1 *Aging*

Informations on the aging evolution of the out-of-equilibrium dynamics can be obtained using the so-called two-times correlation function, as first proposed in [76]:

$$C(q, t_1, t_2) = \frac{\langle I(q, t_1) I(q, t_2) \rangle}{\langle I(q, t_1) \rangle \langle I(q, t_2) \rangle}. \tag{7.14}$$

Here, the averages are performed over the ensemble of the detector pixels characterized by the same exchanged momentum q. The func-

tion has its maximum along the diagonal ($t_1 = t_2$), decaying to one as the time lag $\tilde{\tau} = |t_2 - t_1|$ increases. If the contour lines are parallel to the diagonal, the sample does not present aging dynamics on the time scale investigated. On the contrary, a divergence of the contour lines from the parallel with the diagonal denotes aging. This is illustrated in the following examples.

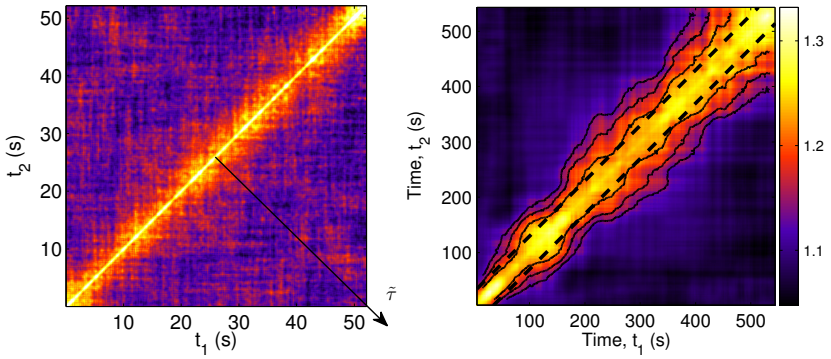

(a) (b)

Figure 24: two-times correlation function measured a) on a Langmuir film of colloidal gold nanoparticles at concentration $\Phi = 69\%$; b) on multilayers of a photosensitive azopolymer photoperturbated with UV light. These results will be further discussed in the following chapters.

The two-times correlation function reported in figure 24a was measured on a Langmuir monolayer of colloidal gold nanoparticles at surface concentration $\Phi = 0.69\%$. At fixed experimental time $t_{age} = \frac{|t_1+t_2|}{2}$, the decay along t represent the correlation function recorded at that specific aging of the sample. Since the mean characteristic time does not change during the experiment -as represented by the contour lines parallel to the diagonal - the two-times correlation function corresponds to equilibrium dynamics. On the contrary, the two-times correlation function reported in figure 24b, measured on multilayers of a photosensitive azopolymer photoperturbated with UV light, shows an evolution of the dynamics towards slower relaxation times; the contour lines are not parallel to the main diagonal, and they diverge as the experimental time increases. We have shown that an evaluation of non-equilibrium effects of the dynamics, impossible to be performed with intensity-intensity out of equilibrium dynamics, is obtained with two-times correlation functions instead.

7.4.2 *Dynamical heterogeneity*

Using the two-times correlation functions as a starting point, after having characterized aging phenomena, it is possible to study the temporal dynamical heterogeneity present in the sample in equilib-

rium conditions, e. g. due to multiple relaxation time scales connected to the presence of cooperatively moving regions.

A first investigation tool is the variance $\chi(q;\tilde{\tau})$ of the two-times correlation function:

$$\chi(q;\tilde{\tau}) = \left\langle C(t_{age},\tilde{\tau})^2 \right\rangle_{t_{age}} - \left\langle C(t_{age},\tilde{\tau}) \right\rangle^2_{t_{age}} \tag{7.15}$$

where $t_{age} = |t_1 + t_2|/2$ and $\tilde{\tau} = |t_2 - t_1|$ grows respectively along the main diagonal and the main antidiagonal. This function, also known as *dynamical susceptibility*, quantifies the amplitude of the fluctuations of the two-times correlation function, as a function of the experimental time t_{age}.

A peak in $\chi(q;\tilde{\tau})$ is usually associated in the literature with the presence of heterogeneous dynamics, taking place on a time scale identified by the time position of such peak. Further investigation requires the measurement of the q-dependencies of the position and of the intensity of the peak of χ.

An example of analysis of the aging of an arrested system using χ is reported in figure 25. Silica colloidal particles ($R = 22nm$) were suspended in a cis-decalin solution of polystyrene, for a resulting concentration $\Phi = 33\%$; the presence of the polymer creates a depletion attraction among the colloids that arrest the dynamics of the sample. χ shows a peak, indicating that the dynamics of the sample is heterogeneous. Moreover, the position of the peak shifts toward slower times as the sample ages, while on the contrary the intensity of the peak is unchanged, meaning that the degree of heterogeneity is not altered by the aging process.

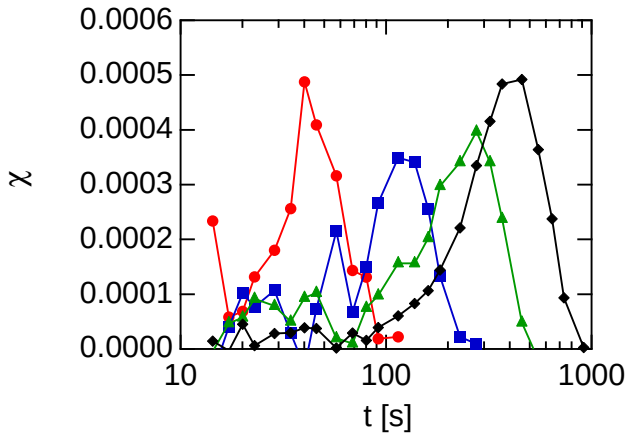

Figure 25: Variance χ for a concentrated depletion gel [77, 75], measured for several values of the aging time t_{age} = 1400s (red circles), 3400s (blue squares), 7000s (green triangles), and 14000s (black diamonds).

The analysis of the dynamical susceptibility χ gives an averaged (along t_{age}) information on the dynamical heterogeneity of the sam-

ple. To allow the discrimination of intermittent processes from continuous dynamics, in particular the slow dynamics of arrested systems, a more general tool has to be introduced: the four-times correlation function [26]. It is defined as

$$g^{(4)}(q;t,\tilde{\tau}) = \langle I(q;t_1)\, I(q;t_1+\tilde{\tau})\, I(q;t_1+t)\, I(q;t_1+t+\tilde{\tau})\rangle \quad (7.16)$$

where the averages are performed over t_1. This function is the temporal analogous of the four-points correlation function commonly found in simulations and theoretical works on arrested systems [26, 78] investigated into the real space.

Commonly, the experimental analysis is limited to the calculation of the variance χ, given the demanding signal-to-noise ratio necessary for the measurement of the four-time correlation function $g^{(4)}(q;t,\tilde{\tau})$. In this project, we have been able to measure $g^{(4)}(q;t)$-for the first time by means of XPCS- on a 2D colloidal sample, a Langmuir film of gold nanoparticles.

8

X-RAY PHOTON CORRELATION SPECTROSCOPY

X-rays speckle patterns have been observed for the first time in 1991 [79], measuring the diffuse (001) peak from an ordered single crystal of Cu_3Au, a crystal containing random arrangement of domains given by the four different ways in which the single unit can occupy a lattice site. This result demonstrated that dynamic light scattering experiments using X-rays were possible; the technique is named XPCS.

XPCS has gained attention in the last 15 years for its unique capabilities of investigation of the slow motions of arrested soft matter; it can be briefly described as the analogous of DLS using X-ray, though it presents several advantages over DLS:

- it is possible to study matter on the interatomic length scale, since it is possible to reach higher values of the exchanged momentum q;
- it is possible to study optically opaque samples, since multiple scattering, one of the main difficulties in DLS, is negligible.

With visible light, coherence is obtained using a laser source. As anticipated in the previous chapter, aside of X-ray Free Electron Lasers, every other X-ray source emits transversely incoherent light. In this case, as for X-ray undulators, coherence is obtained from an highly collimated and monochromatic beam by using micron-sized pinholes: in this case the intensity of coherent light is directly proportional to the brilliance of the source. Currently, XPCS is currently feasible at third generation synchrotrons, since they produce X-rays beams several order of magnitudes more intense than the ones produced by smaller synchrotrons or laboratory sources. The XPCS experiments described in this work were performed using partially coherent X-rays at the ID10A beamline Tröika at the European Synchrotron Radiation Facility (ESRF), a leading laboratory that significantly contributed to the development of this relatively new technique.

During XPCS experiments at ID10A, a single bounce $Si(111)$ crystal monochromator was used to select 8keV X rays, corresponding to a wavelength $\lambda \simeq 1.5\text{Å}$; the beam is characterized by a relative bandwidth $\Delta E/E \simeq 1.4\,10^{-4}$. An estimation of the coherence lengths is obtained from equations 7.1:

$$l_l \simeq \frac{2 \cdot 1.5\text{Å}}{1.4\,10^{-4}} \simeq 1\mu\text{m}$$

$$l_t \simeq \frac{1.5\text{Å} \cdot 46\text{m}}{2 \cdot 300\mu\text{m}} \simeq 10\mu\text{m}$$

A flux of coherent monochromatic x-rays photons higher than $10^9 \frac{ph}{sec}$ is obtained using a $10x10\mu m^2$ pinhole, for a electron current of 100mA injected in the storage ring of the synchrotron; the size of the pinhole is comparable to the transverse coherence area l_t^2. A maximum (but transversely incoherent) flux of $5 \cdot 10^13 \frac{ph}{sec}$ is achieved in the same conditions if the pinhole is removed.

A demonstration that synchrotron radiation is characterized by sufficient coherence, despite being generated by an incoherent source, is the measurement of Fraunhofer diffraction pattern of a pinhole, as reported in figure (26).

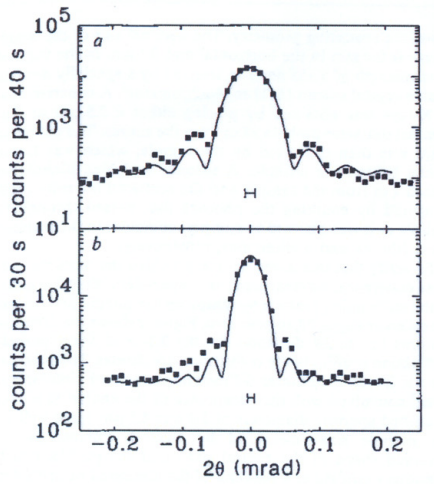

Figure 26: Fraunhofer diffraction from a, 2.5μm and b, 5μm diameter pinholes [79].

During the experiments, a set of guard slits was placed just upstream of the sample to block the parasitic scattering due to Fraunhofer diffraction from the beam-defining slit.

The scattering from the sample was usually recorded by a 2D array of detectors (Medipix [80]). It consists of 256x256 detectors (pixels) each of $55 \times 55\mu m^2$ area, and it is located 2 meters downstream of the sample. In the reciprocal space, this setup corresponds to an accessible exchanged momentum q ranging from 0.005 to $0.2nm^{-1}$. This detector is capable of acquiring up to 1000 frames per second. For measurements of dynamics characterized by timescales down to tens of nanosecond, i.e. capillary waves from water surface, an Avalanche Photo-Diode (APD) was employed, in combination with a fast, high resolution, multiple-tau digital correlator Flex01-08D[1], with a minimum sample time of 8ns and 1088 real-time channels.

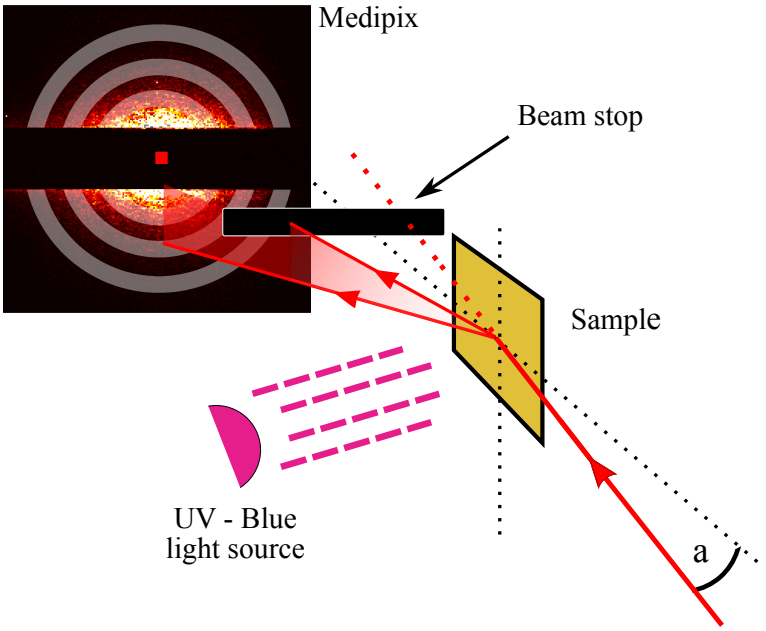

Figure 27: Sketch of the beamline setup used for XPCS measurements on deposited multilayers. Iso-q rings are indicated by lighter circular strips.

8.1 PECULIARITIES OF XPCS EXPERIMENTS ON DEPOSITED MULTILAYERS

During this project, XPCS measurements have been performed on multilayers of azopolymer transferred on silicon substrate, using a pseudo-GISAXS reflection geometry. The $10 \times 10 \mu m^2$ size beam was

1 correlator.com

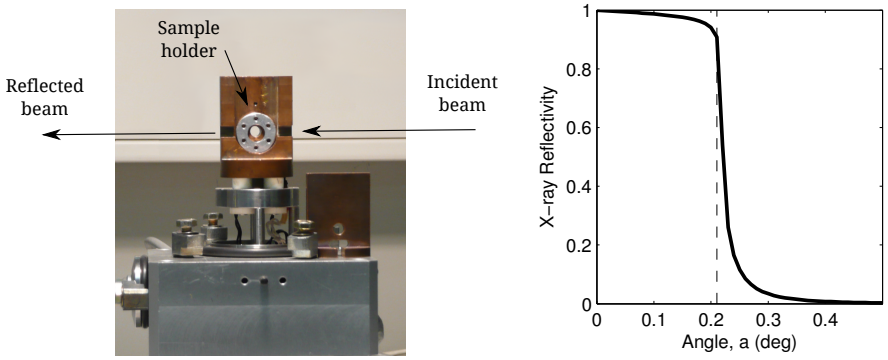

(a) (b)

Figure 28: (a) Sample chamber used for XPCS measurements on deposited multilayers. The sample is fixed vertically on the aluminum ring, and it may be illuminated with UV or Blue light frontally. (b) Simulation of grazing incidence reflection from silicon, that shows total reflection for incident angles $\alpha < 0.21°$.

directed towards the sample with a grazing incident angle $\alpha = 0.15°$, below the total reflection angle of silicon $\alpha = 0.21°$ (see figure 28b). Therefore, a total surface of size

$$10\mu m \times \frac{10\mu m}{\sin(0.15°)} = 10\mu m \times 3.8mm = 3.8\,10^4\,\mu m^2$$

is probed by the X-ray beam.

Multilayer samples were prepared by deposition of an high number (greater than 50) of Langmuir-Schaeffer layers of polymer, for a total thickness greater than 100nm. This can still be considered a 3D sample, however a complete and uniform photoperturbation of the sample is now much more feasible.

The sample holder was covered by a steel cap, equipped kapton windows. The UV ($\lambda = 395nm$) and blue light ($\lambda = 480nm$) LED arrays[2] were fixed frontally, with respect to the sample, on a custom made vacuum flange. Rotative pump vacuum was continuously maintained during measurements.

The sample chamber was equipped with an heating resistor, connected to a Lakeshore temperature controller, so that temperatures up to $T = 100°C$ could be easily kept constant within $0.1°C$ accuracy.

The Medipix pixels located around the reflected were divided into rings, each of them identified by the same exchanged momentum, in analogy with a common SAXS experiment, as indicated in figure 27. Pixels located too close to the beamstop were excluded. XPCS analysis was then conducted using an adapted Matlab version of the software correlator developed by the ID10A staff.

8.2 MEASUREMENT AT THE AIR/WATER INTERFACE

A similar experimental geometry was used also for XPCS measurements at the air/water interface. The sample chamber was replaced by a custom made Langmuir trough, fixed to the beamline spectrometer through a anti-vibration table. The Langmuir trough (figure 29) has a single teflon barrier, and it is controlled by R&K[3] hardware. The total area can be varied in the range $106 - 686.6\,cm^2$.

The trough is relatively large, to minimize meniscus effect on the scattered signal, but this imply a relatively low compression ratio 3 : 1. The water level has been adjusted so that a very small -almost absent- meniscus is present. Finally, the Langmuir setup is completed by a Wilhelmy balance by NIMA. The whole apparatus is covered by a plexiglas cap equipped with kapton windows: Helium is continuously flushed in the chamber, reducing the parasitic scattering from air and providing a controlled atmosphere that contributes to minimize radiation damage on the sample.

2 Roithner LaserTechnik GmbH, Wien, A
3 Riegler & Kirstein GmbH, Potsdam, DE

(a) (b)

Figure 29: Photos of the Langmuir trough used for XPCS measurements at the air/water interface.

The X-ray beam (size $10 \times 10\mu m^2$) is directed towards the water surface with an angle $\alpha = 0.12°$, leading to a total footprint

$$10\mu m \times \frac{10\mu m}{\sin(0.12°)} = 10\mu m \times 4.7mm = 4.7\,10^4\,\mu m^2.$$

The position of the X-ray spot on the sample has to be frequently checked, to ensure that it is located in the center of the trough, where the water surface is flat.

Again, the detector has been positioned in correspondence of the reflected beam. The pixels are grouped into square groups, each of them identified by two components of the exchanged momentum, $q_{||}$ and $q_\perp$, respectively parallel and perpendicular to the water surface, as indicated in figure 30. The diffraction pattern arising from a Langmuir film is anisotropic, hence the pixels that compose the detector

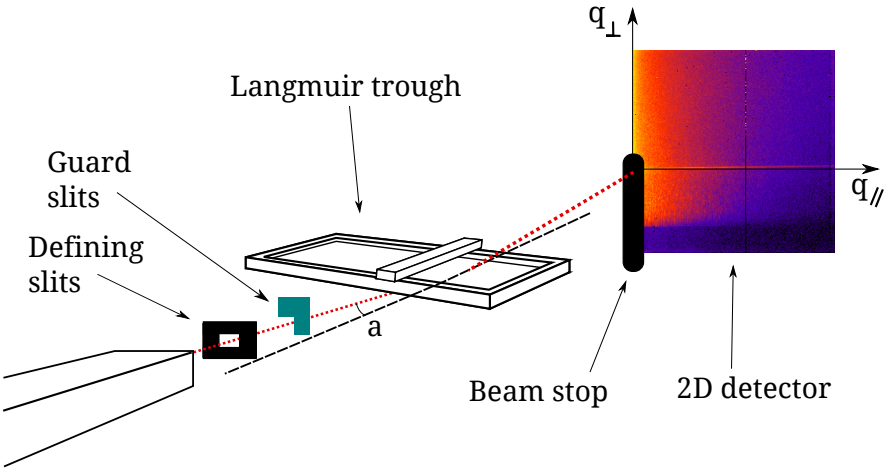

Figure 30: Sketch of the beamline setup used for XPCS measurements at the air/water interface.

area are divided into a grid of squares. Each square is then characterized by a parallel and a perpendicular component of the exchanged momentum, $q_{||}$ and $q_{\perp}$.

Part IV

STUDIED SYSTEMS: A) FILMS OF A PHOTOSENSITIVE AZOPOLYMER

Mechanical properties and internal dynamics of molecular layers of photosensitive polymers are measured. The effects of UV-blue light photoperturbations are analyzed, with particular regards to photoinduced out-of-equilibrium states.

9

A PHOTOSENSITIVE GLASS-FORMER

Azobenzene is a chromophore molecule consisting in two phenyl rings connected by the azo linkage (-N=N-). It presents two distinct isomers, indicated respectively as *trans* and *cis* (shown in figure 31a). The *trans* isomer is $0.99nm$ long and electrically neutral, while the *cis* isomer has a length of $0.55nm$ and presents a molecular dipole of 3.1 Debye units. The UV-Vis absorption spectra of the two isomers are significantly different: in particular, the *trans* isomer spectrum shows an absorption peak in the near-UV region, that is not present in the spectrum of the *cis* isomer.

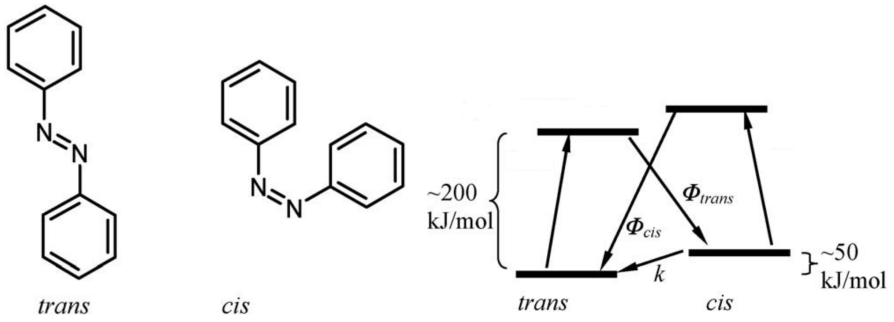

Figure 31: a) *Cis* and *trans* isomers of the azobenzene; b) Simplified model of the azobenzene state model. The *trans* isomer is the thermally stable form, while the switching to the *cis* isomer is induced by UV photoperturbation [81].

The most interesting feature shown by azobenzene is the efficient photochemical isomerization induced by the absorption of a photon [81, 82]. Figure 31b reports a scheme of the energetic states of the two azobenzene isomers; at first, we note that the *trans* isomer is thermodynamically favored, presenting an energy about $50kJ/mol$ lower than the *cis* isomer. Upon illumination of *trans* azobenzene with UV light, where its absorption spectrum shows a peak, the *trans*-to-*cis* transition is induced, with quantum yield (photoisomerized molecules per photon absorbed) Φ_t. On the contrary, a photon with wavelength in the *cis* absorption band (blue light, $\lambda \simeq 450nm$) may trigger the reverse *cis*-to-*trans* transition with quantum yield Φ_c. The photoinduced transitions between *trans* and *cis* states are completely reversible, without the formation of side products even after innumerable isomerization cycles. Furthermore, the energetically-favorite *trans* isomer is thermally recovered with rate k. This thermal isomerization presents an energy barrier of $90kJ/mol$. Summarizing these consideration, it can be noted that:

- upon illumination with UV light, the *cis*-to-*trans* transition is induced. It competes with the thermal recovery of the *trans* isomer. Therefore, the steady-state population of *cis* and *trans* isomers depends on the quantum yield Φ_t and the thermal relaxation rate k, although the *cis* isomer is commonly favored.
- irradiation with blue light pumps both *cis* and *trans* configurations with roughly the same efficiency, yielding a continuous cycling of the azobenzene molecules between the two states. The steady-state *trans*/*cis* population ratio will depend on Φ_c, Φ_t and k.

The applicative use of photoisomerization to produce molecular actuator was first proposed by de Gennes [83], and since then a wide literature flourished. The *trans-cis* isomerization has been used to modulate or trigger a desired property in many azobenzene-containing polymers or supramolecular assemblies that contained it. Among the properties modulated by the photoinduced transition of the azobenzene group, we evidence

- molecular photoinduced birefringence[84],
- photo-expansion of molecular layers[85],
- photoinduced changes in the viscoelastic response [86, 87, 88].

These remarkable features are linked to the severe photoinduced modification of the polymeric matrices or organized structures (liquid crystalline assemblies or Langmuir films) formed by azobenzene based molecules. These modifications take place on (and above) the spatial scale of the domains of the system [82] -with collective simultaneous reorganization upon photoperturbation- and on the temporal scale of tens of seconds.

In this work, attention will be focused on photoinduced effects on polymeric viscoelasticity. A work by Ketner et al. [89] revealed the remarkable potential of aqueous micellar solutions, whose viscosity can be reduced by more than four orders of magnitude upon UV exposure. The limiting factor in that study was the irreversible character of the transformation; however, in a recent study [88] the authors demonstrated reversible rheological property changes in an azo-containing siloxane polymer backbone. These properties are of particular interest for light-activated damping mechanisms, actuable armor, and related applications in fields such as robotics and sensors.

9.1 PA4, A SIDE-CHAIN AZOPOLYMER

The azobenzene-based sample under investigation in this project is a side-chain, liquid-crystal homopolymer, $Poly[[4-pentyloxy-3'-methyl-4'(6-acryloxyexyloxy)]azobenzene]$, hence named *PA4*.

PA4 contains the azobenzene moiety in its lateral chains. Its chemical formula is reported in figure 32.

In this particular polymer, azobenzene is connected to the main chain by a flexible chain consisting of 6 groups CH_2; another chain is attached after the azobenzene group to increase the chain length. The length of these spacers was chosen in order to reach an equilibrium between two competing needs:

- to decouple the side chain from the main chain, so that the photosensitivity of the molecule is enhanced;
- to bound side and main chain strongly enough to form large and stable domains.

The conformation of the azobenzene containing side chain can be changed by UV and visible light illumination.

PA4 is characterized by a glass transition temperature $T_g = 21°C$, above which a nematic phase is formed. This phase persists up to a clearing temperature $T_c \simeq 90°C$ [90].

This part will focus on:

- the preliminary characterization of Langmuir layers of PA4 in different illumination conditions, measuring
  - its UV-Vis absorption spectrum;
  - the surface pressure - area isotherms;
  - the glass transition temperature T_g;
- the measurement of the mechanical properties of Langmuir films of PA4, in particular the out-of-equilibrium photoinduced effects on the response;
- the measurement of the internal dynamics of PA4, by means of XPCS on deposited multilayers.

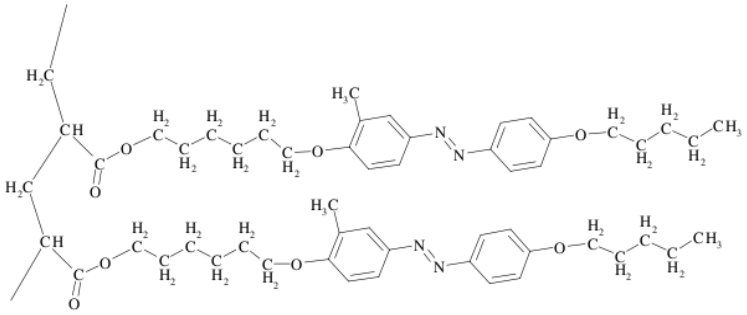

Figure 32: Two monomeric units of PA4. Note the azobenzene group in the side chain.

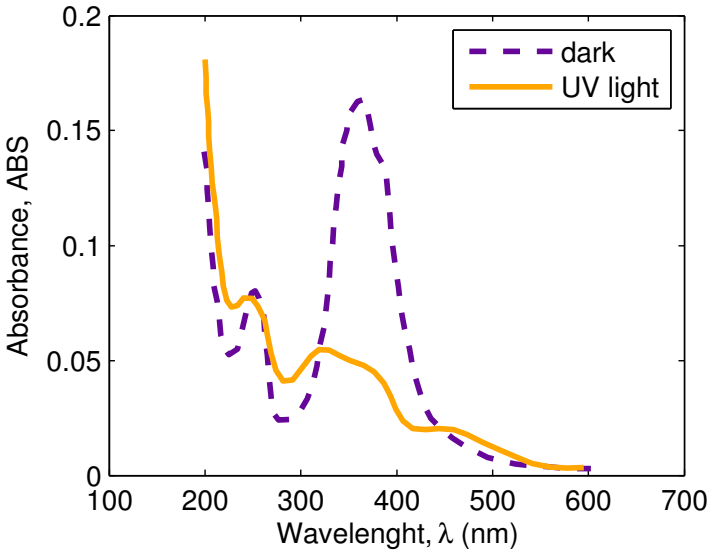

Figure 33: UV-visible light absorbance spectra of PA4, in dark and under UV light photoperturbation.

The UV-visible absorbance spectra measured on PA4 in different illumination conditions are reported in figure 33. In thermal equilibrium and in absence of illumination, the absorption spectrum of PA4 shows *trans*-azobenzene's pronounced absorbance peak in the near-UV region of the spectrum. After UV photoperturbation with light at 395nm, the absorption spectrum presents a much weaker peak in the UV region, while a peak centered at 450nm appears. In every measurement reported in this chapter, the *trans*-to-*cis* transition of PA4 is induced through illumination with UV light at $\lambda = 395nm$, while the *trans-cis* configuration cycling is obtained via illumination with light at $\lambda = 480nm$.

9.2 $\Pi - A$ ISOTHERMS

Monolayers of PA4 were formed at the air/water interfaces using the Langmuir trough apparatus described in chapter 2. A $0.33mg/ml$ benzene/hexane 2:1 solution of PA4 was spread on high purity water; then, the surface area A of the trough is slowly reduced by closing the teflon barriers, while the surface pressure Π is measured.

This measurement was repeated in dark and under UV illumination, at room temperature: results are shown in figure 34. In the first case, the isotherm presents a steep increase in the surface pressure at a reduced area $A \simeq 40Å/mol$. Under UV photoperturbation the isotherm shows a constant but weak increase in surface pressure stating from $A \simeq 90Å/mol$. The two isotherms intersect at a surface pressure $\Pi = 10mN/m$; in other words, in correspondence of this value of the surface pressure PA4 films in *cis* and *trans* configurations

have roughly the same area per molecule. This value of Π was therefore chosen as the working surface pressure for all the subsequently measurements of the out-of-equilibrium properties of PA4 films, because it minimizes eventual macroscopic transfers of matter due to photoinduced gradients of pressure.

9.3 PHOTOINDUCED CHANGES OF THE GLASS-TRANSITION TEMPERATURE

This section reports a null-ellipsometry experiment performed to determine the changes in the glass transition temperature of PA4 due to photoperturbation with UV (395nm) and blue (480nm) light. The glass transition temperature is measured, in the different illumination conditions, by monitoring the thickness of multilayers of PA4 on silicon substrate as a function of temperature; T_g correspond roughly to the point where rate of increase of thickness upon heating changes. Similar experiments were performed in the past to measure the dependence of the glass-transition temperature T_g as a function of the number of deposited layers [91, 92, 93, 94]. In particular, interfacial effects were found for a number of layers lower than 4; since we are not interest in the investigation of these effects, our samples consisted on a higher number of layers.

By means of layer-by-layer Langmuir Schaeffer deposition, either 25 or 50 layers of PA4 were transferred on silicon surfaces. The interfacial layer was formed by spreading the PA4 solution at the air/water interface as described in the previous section, followed by a slow

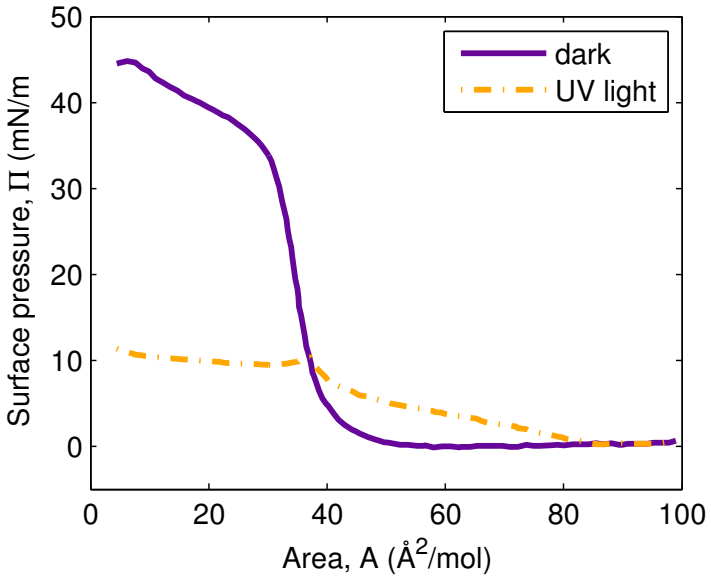

Figure 34: Surface pressure - Area isotherms of PA4 monolayers in thermal equilibrium, in dark and under UV illumination.

compression, reaching the deposition surface pressure $\Pi = 10 mN/m$, at constant temperature $T = 24°C$. Deposition was performed with minimum ambient light, to avoid unnecessary photoperturbation of the sample. Deposited multilayers were left to equilibrate, prior to characterization, for 12 - 24 hours at room temperature.

Null-ellipsometry measurements were performed at incident angle $\alpha = 70°$ with a He-Ne laser ($\lambda = 632.8nm$). The sample was placed on a Peltier device in cooling/heating mode, controlled by an Eurotherm PID controller equipped with a K-type thermocouple. A thin layer of thermo-conducting paste was interposed between the silicon wafer and the Peltier itself, to ensure proper thermal exchange. The temperature of the sample was determined with $0.1°C$ accuracy. The sample was heated well above the expected value for T_g, but below the clearing temperature. The temperature was the diminished at a very slow rate, $14K/hour$, while the ellipsometric angles Δ and Ψ were measured. A measurement performed in dark conditions is reported in figure 35.

From $\Delta(T)$ and $\Psi(T)$, the temperature dependence of the thickness d of the multilayer is obtained; results are reported in figure 36 for the three illumination conditions investigated: thermal equilibrium in dark and photoperturbation with UV and blue lights. The thickness d measured in each condition was normalized by dividing it with its value measured at $T = 50°C$. The curves show a change of slope, whose position indicates the glass transition temperature T_g. Data were fitted with lines in the regions above and below the point of slope change. Parallel lines are used in the three different illumination

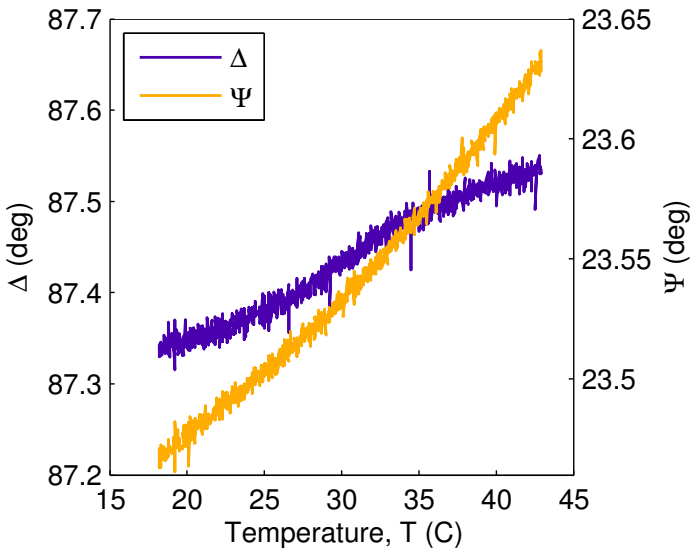

Figure 35: Temperature dependence of the ellipsometric angles Δ (red line) and Ψ (blue line) measured on a sample consisting of 25 PA4 layers transferred on silicon, without photoperturbation.

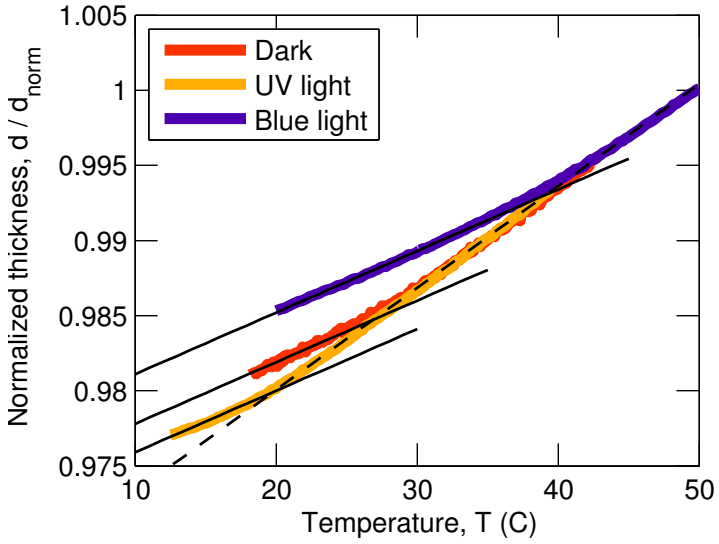

Figure 36: Temperature dependence of the thickness of a multilayer sample of PA4 deposited on silicon, in different illumination conditions (thick lines), normalized to the value measured or inferred at $T = 50°C$. Thin black lines represents the linear fits described in the text.

dark	$27 \pm 2°C$
UV light	$19.8 \pm 1°C$
Blue light	$39 \pm 2°C$

Table 2: Glass transition temperature T_g determined with null-ellipsometry in dark and under UV and blue lights photoperturbation.

conditions. The value of T_g correspond to the temperature at which the two lines intersects: values are reported in table 2.

Considering the result in absence of photoperturbation, it has to be noted that the value of the glass transition temperature measured on multilayers transferred on silicon differs significantly from the value measured in bulk [95], $T_g = 21°C$. This difference can be ascribed to the fact that the present measurements were conducted on deposited multilayers, and not in bulk; therefore, we consider the relative changes of T_g induced by photoperturbation, reported in table 3.

	$\Delta T_g/T_g$ (dark)
UV light	-2%
Blue light	3%

Table 3: Relative changes in the glass transition temperature T_g induced by UV and blue lights photoperturbation.

These changes in the glass transition temperature of PA4 may be imputed to the conformational changes due to the variation of the *trans*/*cis* population. The illumination with UV light folds the side chains of the polymer, thus reducing the entanglements in the polymer matrix and leading to an higher value of T_g. On the contrary, the *cis-trans* cycling isomerization induced by irradiation with blue light may cause a reorganization that leads to a more energetically stable state, characterized by lower T_g.

9.4 MULTILAYERS DEPOSITED ON SILICON

The investigation of the mechanical shear response of PA4 is performed at the air/water interface. The demanding signal-to-noise ratio requirements of XPCS experiments required for these measurements, on the contrary, the use of multilayers deposited on silicon.

The samples consisted of 75 molecular layers (at surface pressure $\Pi = 10 mN/m$) transferred on a silicon substrate by means of the Langmuir-Schaeffer technique. The thickness of each individual monolayer was found to be about $2nm$, which gives a total sample thickness of $150nm$.

A typical AFM image of a monolayer of PA4 [85] is reported in figure 37. Though the deposition of a single layer results in an evident structural heterogeneity, the successive transfer of Langmuir-Schaeffer results in a overall homogeneous sample.

The homogeneity of their surface was extensively characterized by null-ellipsometry, AFM, and SEM. The null-ellipsometry characterization of the surface retrieves a typical surface roughness of $1nm$, in excellent agreement with the typical values previously reported for films of this polymer [94, 96].

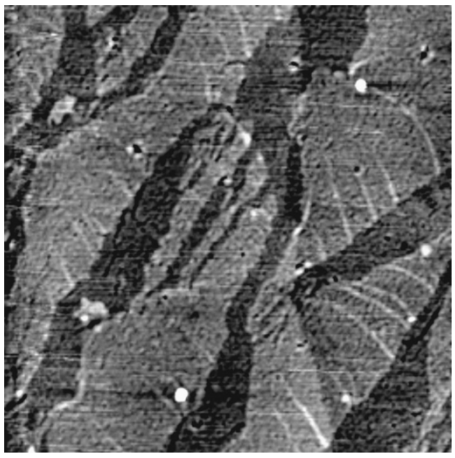

Figure 37: AFM image of a film of PA4 ($\Pi = 15 mN/m$) transferred on silicon substrate [85]. The horizontal scale is $6 \times 6 \mu m^2$, the vertical contrast scale is $8nm$.

10

MECHANICAL PROPERTIES OF THE AZOPOLYMER PA4

The observed changes in the glass transition temperature of PA4 indicates a change in the microscopic structure of the sample; this may lead to analogous variations in the viscosity of PA4 Langmuir monolayers. Using the interfacial shear rheometer described in section 4, the rheological properties of Langmuir monolayers of PA4 were investigated at different temperatures, and under several illumination conditions. In this section we report results observed in equilibrium. The Langmuir monolayer is formed as usual, spreading a $0.33 mg/ml$ benzene/hexane 2:1 solution of PA4 on high purity water. The area of the Langmuir trough is then reduced to reach a surface pressure $\Pi = 10 mN/m$, at which measurements are performed.

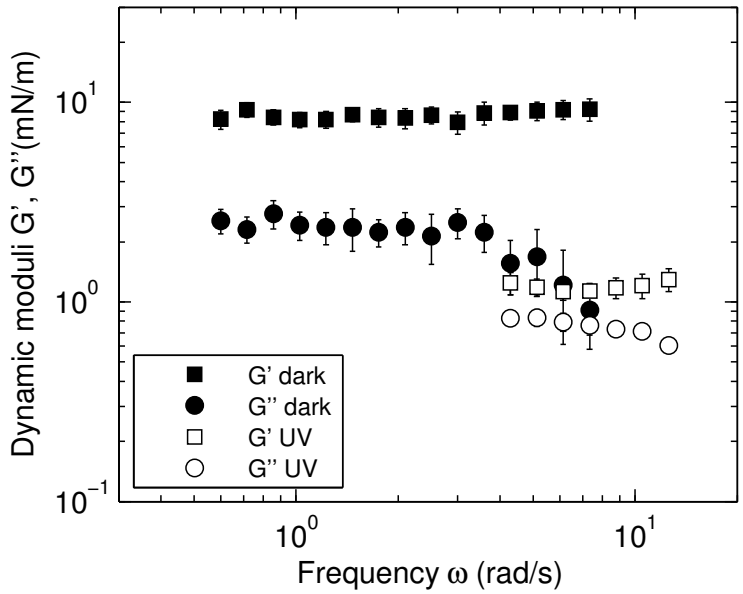

Figure 38: Angular frequency dependence of the dynamic shear moduli G' (squares) and G'' (circles) measured on PA4 in trans configuration (filled points) and under UV illumination ($1.5 mW/cm^2$, empty symbols).

Figure 38 reports the angular frequency dependence of G' and G'', in dark and under UV light ($P = 1.5 mW/cm^2$). In both illumination conditions G' and G'' show a very weak -almost absent- frequency dependence. On the contrary, UV illumination varies the loss factor $\tan\delta$: *trans* PA4 is mainly elastic, having a loss factor $\tan(\delta)$ roughly

equal to 0.2, while *cis* PA4 shows a viscoelastic behavior, with a value of the loss factor close to unity.

Figure 39 reports the variation of the mechanical response of a Langmuir film of PA4 under UV illumination, with power density ranging from 0 to $1.5 mW/cm^2$. Measurements were performed at constant frequency ($\omega = 3.14 rad/s$),

Since the trans configuration of the azobenzene moiety in the side chains is induced by thermal agitation, constant UV illumination has to be maintained during the measurement. An equilibrium between the competing *trans-to-cis* and *cis-to-trans* mechanisms, induced respectively by UV light and thermal agitation, is reached; therefore, the mechanical properties observed depend on both temperature and UV illumination power density.

Having determined the illumination conditions that ensure the reaching of a stable *cis* state, we characterize the temperature evolution of the mechanical properties of both the *trans* and the *cis* PA4 Langmuir monolayers. At temperatures ranging from 19°C to 36°C, several measurements of the frequency dependence of G' and G'' were performed. The surface tension of the film was kept constant at $\Pi = 10 mN/m$. Given the weak frequency dependence of both G' and G'', we consider data taken at a single frequency ($\omega = 3.14 rad/s$). Measurements performed with the ISR apparatus were compared with analogous measurements performed with a *CIR-100 oscillating ring rheometer* and by means of the *oscillating barriers* technique, founding complete agreement in the the results.

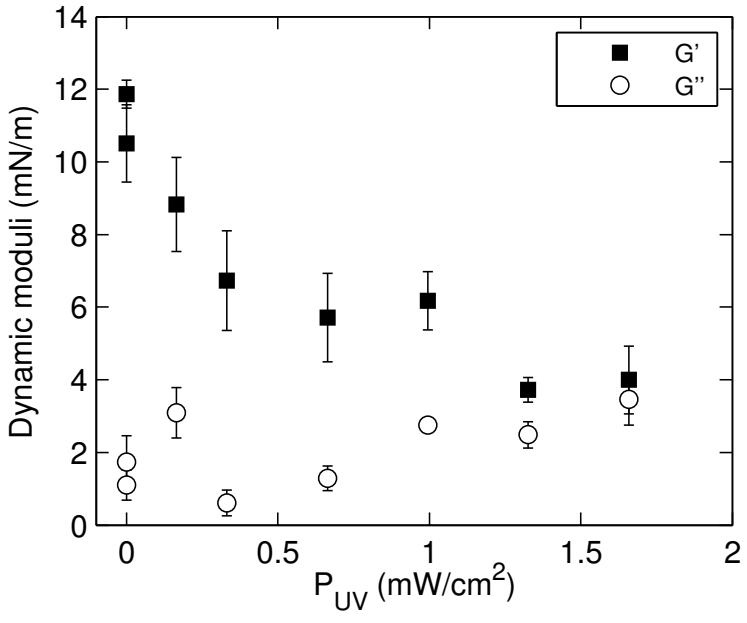

Figure 39: Evolution of the dynamic shear moduli G' and G'' as a function of the UV power density on the sample.

Figure 40 report the Arrhenius plot of the temperature evolution of the 2D viscosity $|\eta| = |G|/\omega$ for PA4 in *trans* configuration and after 5 minutes of UV exposure at high power density. These illumination conditions ensure the reaching of an equilibrium *cis* configuration, as demonstrated in the previous measurements.

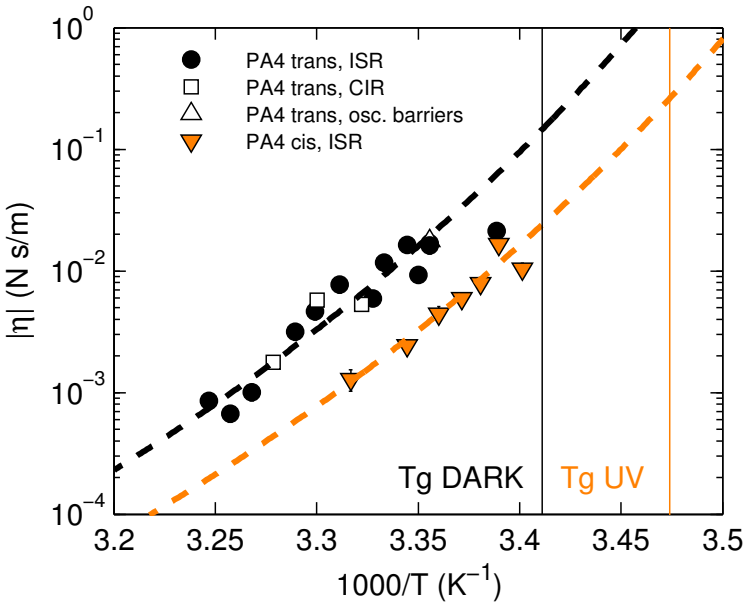

Figure 40: Shear viscosity $|\eta|$ measured at constant frequency ($\omega = 2\pi \mathrm{rad/s}$) and at several temperature using several different techniques in equilibrium (Black and empty symbols) and after UV photo-perturbation (yellow triangles). Data are compared with the VFT laws described in the text (dashed lines).The vertical continuous lines represent the glass transition temperatures measured by null-ellipsometry.

The temperature dependencies of the viscosity η, for PA4 both in its *trans* or *cis* states, are compatible with a Vogel-Fulcher-Tamman (VFT) exponential decay:

$$\eta = \eta_\infty \exp\left(\frac{T_A}{T - T_0}\right). \tag{10.1}$$

The temperature range probed is small, because of the huge water-evaporation problems that occur during a Langmuir experiment when temperature is raised above $30 - 35°C$. Both the *Vogel temperature* T_0 and the *activation temperature* T_A were therefore fixed to the values determined - in bulk PA4 in thermal equilibrium- by means of Electron Paramagnetic Resonance (EPR) measurements [97] and then confirmed by depolarized micro-Raman and Quartz Crystal Microbalance experiments [98]. Therefore, the only remaining fit parameter is η_∞, determined via a χ^2 minimization procedure. All the parameters are reported in table 4.

	$T_A(K)$	$T_0(K)$	$\eta_\infty(Ns/m)$
dark	1270	237	$(0.9 \pm 0.1) \cdot 10^{-15}$
UV light	1270	237	$(0.3 \pm 0.07) \cdot 10^{-15}$

Table 4: VFT parameters T_0, T_A and η_∞ measured for PA4 in *trans* and *cis* configurations.

10.1 OUT-OF-EQUILIBRIUM RESPONSE: REVERSIBILITY

After having studied the mechanical response PA4 in equilibrium condition in its *cis* and *trans* states, in this section the mechanical characterization of the out-of-equilibrium transition processes is reported. A Langmuir monolayer is formed in absence of illumination at $\Pi = 10mN/m$, following the procedure described in the previous sections. An ISR measurement is started at constant frequency $\omega = 3.14rad/s$. Subsequently, while the PID controller of the Langmuir trough keeps constant the surface pressure, the illumination conditions inside the ISR apparatus are changed, alternatively illuminating the sample with UV and Blue lights. The illumination power density in correspondence of the film was roughly equal to $P = 1.5mW/cm^2$, for UV and blue lights. A fully reversible transition of the film between its equilibrium states configuration is observed, tough it requires several minutes to be completed.

A measurement is reported in figure 41. A *reversible* transition is shown, although it seems evident that equilibrium states are not reached. Despite this, a change of roughly one order of magnitude in $|G|$ is observed. While illumination with UV light makes the system more fluid, as already verified with equilibrium measurements, we note that illumination with blue light push the system towards a more rigid state, with an higher dynamic shear modulus $|G|$. Since under photoperturbation at this wavelength both *cis*-to-*trans* and *trans*-to-*cis* isomerization processes have approximately the same efficiency, on the macroscopic scale probed by ISR the film stiffens, because of the reduction of defects and grain boundaries comparable to that achieved through a thermal annealing process.

To ensure a faster transition and the reaching of equilibrium values in the different illumination conditions during the limited time-scale over which a Langmuir layer is stable, the illumination power density provided by the light sources was raised to roughly $3mW/cm^2$: then, a *cis-trans-cis* transition is measured at constant frequency ($\omega = 3.14Hz$). In figure 42, the needle position during oscillations is reported as a function of time. It is worth noting the huge reduction of the oscillation amplitude $d(t)$ caused by blue light photoperturbation (from $50\mu m$ to $\simeq 1\mu m$, a value barely detectable with the current experimental setup) as well as the complete recovery of the *cis* state after UV light is turned on.

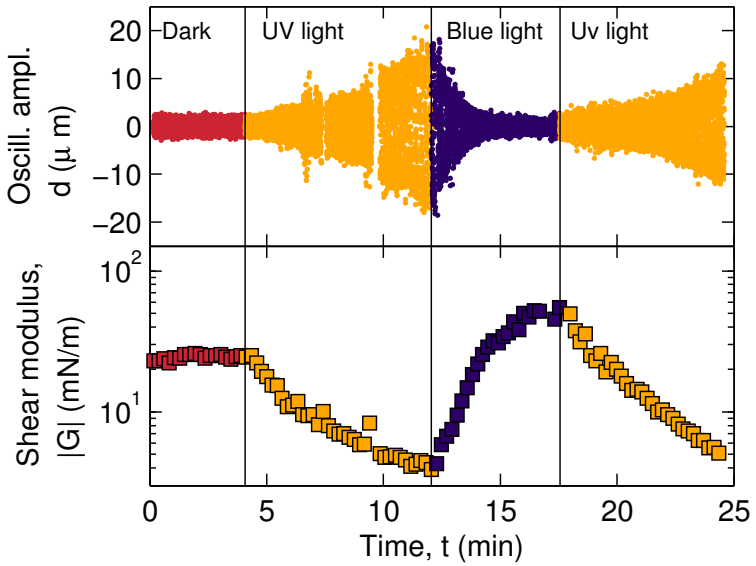

Figure 41: Reversible transition of the dynamic shear modulus |G| during photo-perturbation, measured at constant frequency $\omega = 3.14$Hz and at constant temperature $T = 26°C$. Top panel: photoinduced change in the needle oscillation amplitude. Bottom panel: photoinduced reversible change in the dynamic shear modulus G.

Figure 43 reports the dynamic shear modulus |G| as a function of time. The change in illumination from UV to blue light causes a change of almost three orders of magnitude in the mechanical shear response of the film: despite this, this huge change is completely reversible when the illumination is reverted back to UV light.

Inspection of figure 43 shows that the film illuminated by blue light is characterized by a value of $|G|$ larger than that of the all trans equilibrium film, represented in the figure by the dash-dot red line. This can be explained recalling the two effects of blue light on the azobenzene film: on one side it induces *cis*-to-*trans* isomerization, thus reverting the effects of UV illumination, on the other side it also induces resonant isomerization, due to the fact that both *trans* and *cis* isomers have a comparable absorption at this wavelength, as shown in figure 33. The same effect is present also in the measurement reported in figure 41. Therefore, resonant isomerization could be responsible of the enhancement of azobenzene packing that induces a more compact and stiff phase than that obtained in the completely *trans* film obtained by formation and compression of the film in absence of illumination.

If the time scale of the transitions is considered, we find that both the two processes are completed in several tens of seconds, a time scale far longer than that (tens of nanoseconds) required for the photoswitching of the azobenzene moiety [84]. This long time scale is due to the mesoscopic rearrangements occurring in the film structure, that are responsible for the very different mechanical properties of the

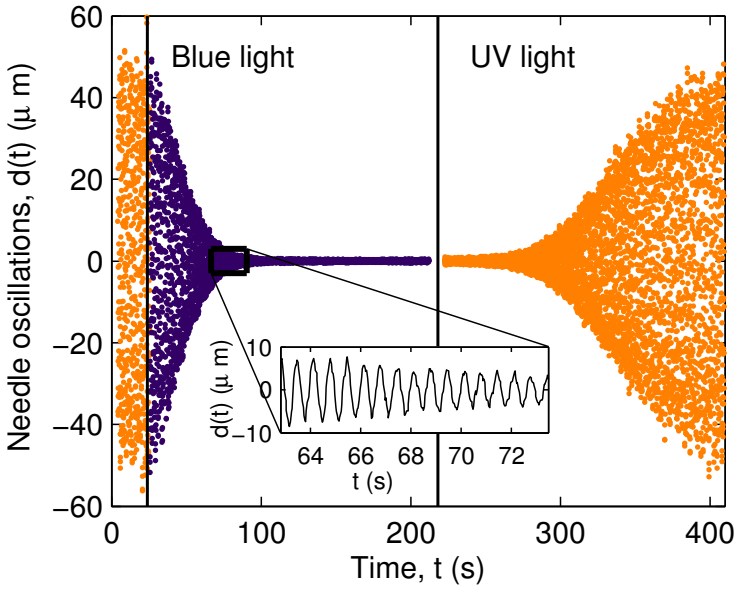

Figure 42: Needle oscillations in a PA4 film measured in different illumination conditions, at constant temperature $T = 26°C$. Note the complete reversibility of the oscillation amplitude change. The vertical lines indicates the instants where the illumination conditions were changed.

different states of the polymers. The two transitions are fitted with two different phenomenological forms:

- the *cis-trans* cycling annealing process (Blue light photoperturbation) is fitted by an *error function* increase to a saturation value:
$$|G(t)| \propto \operatorname{erf}\left(-\frac{t}{\tau}\right) = \frac{2}{\sqrt{\pi}}\int_0^{-t/\tau} e^{-s^2}\,ds$$
with a resulting characteristic time $\tau = 42s$;
- the transition to the *cis* state (UV light photoperturbation) is described as an exponential decrease of $|G(t)|$:
$$|G(t)| \propto \exp\left(-\frac{t}{\tau}\right)$$
with a characteristic decay time $\tau = 17s$;

Similar time scales were also found by XPCS on the same transitions (see chapter 11), and by pump probe photoinduced birefringence on molecular layers of the same polymer [90, 99]. The different analytical shapes of the two kinetics can be explained as follows: in the fluid *cis* film the presence of a small number of *trans* isomers has a negligible effect, the modulus starts to build only when the *trans* concentration grows above some threshold. In the stiff film obtained with blue light photoperturbation, on the contrary, even a small concentration of *cis*

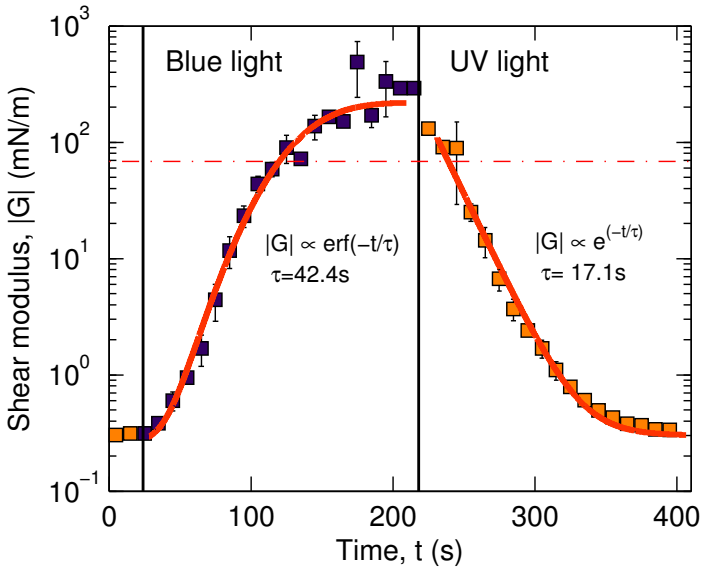

Figure 43: Evolution of the dynamic shear modulus |G| during photo-perturbation. Note the huge, but still reversible, change of roughly three orders of magnitude.

molecules acts as plasticizer, thus being effective in fast reduction of the shear modulus.

In figure 44 the loss factor tan(δ) is reported, showing a transition from a more viscous response towards a more elastic one during blue light photoperturbation. Again, the change in the viscoelastic response is completely reversible.

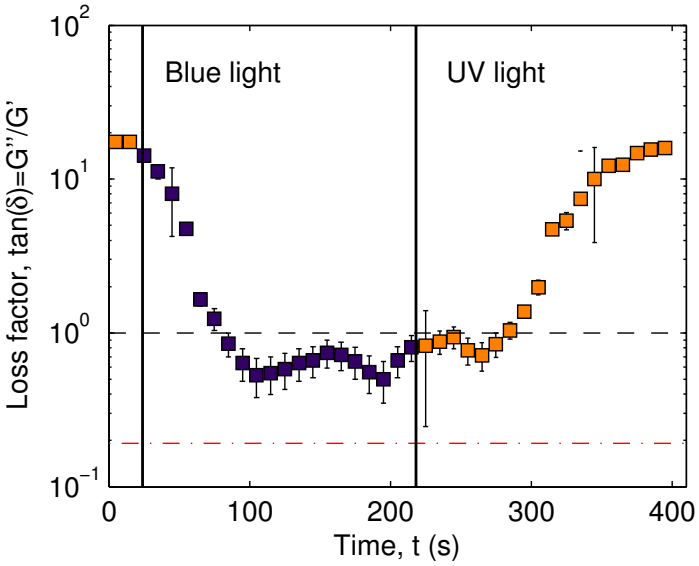

Figure 44: Evolution of the loss factor tan(δ) during photo-perturbation. The sample change from an elastic to a viscous response.

11

MICROSCOPIC DYNAMICS OF THE AZOPOLYMER PA4

Internal dynamics of PA4 was measured by means of XPCS on Langmuir-Schaeffer (LS) multilayers of PA4 transferred on silicon, using the experimental setup described in section 8.1.

Several measurements were performed in the temperature range $40 - 90°C$, in dark and under UV and blue light illuminations.

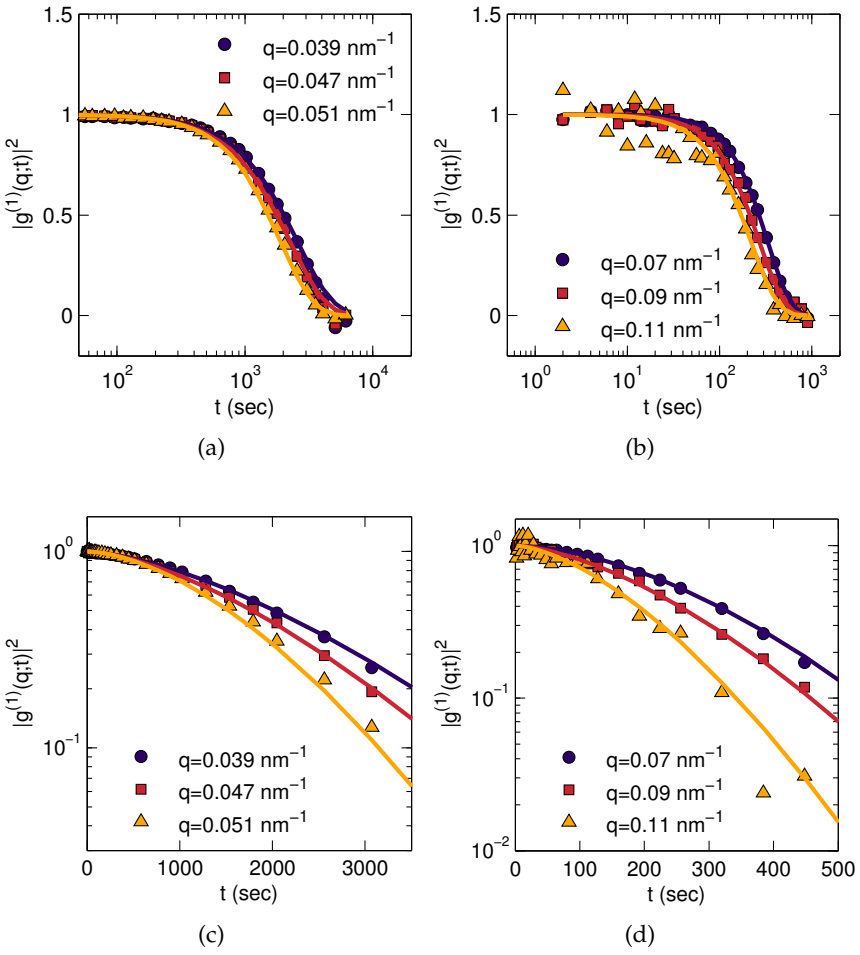

Figure 45: Normalized correlation functions $\left|g^{(1)}(q;t)\right|^2$ measured at $T = 62°C$ and for several values of the exchanged momentum q, in dark (a, c) and under UV illumination (b, d). Panels a) and b) report the usual lin-log plot, while in panels c) and d) data are reported in a log-lin plot to highlight the q-dependence of the correlation functions.

A proper waiting time was introduced, after the application of photoperturbation, in order to ensure the reaching of equilibrium conditions. Sets of 10000 frames each were collected, with a separation time between frames of the order of $1-5sec$ at low temperatures. The exposure time of each frame was limited to 0.5 seconds by means of a triggered shutter, in order to minimize beam damage effects on the sample. At higher temperatures, the separation time between frames was reduced, since the dynamics is faster in such conditions. Therefore, the total measurement time ranged from 10 minutes up to a few hours.

Correlation functions $g^{(2)}(q;t)$ were calculated for several values of the exchanged momentum q in the range $q = 0.05-0.15nm^{-1}$. A subset of correlation functions is reported in figures 45a-c (dark) and 45b-d (UV illumination). Each correlation function has been fitted with the KWW exponential (equation 7.13) with all parameters left free to vary.

In the subsequent analysis we heuristically rejected about 10% of the data corresponding to the worst fits as measured by the χ^2 test. The extracted relaxation times τ are shown in figure 46 as a function of q for different temperatures, in dark -panel (a)- and under UV illumination -panel(b). Power law fits $\tau \propto q^{-1}$ are shown by the continuous lines in the same figure 46.

Both the contrast β and the compression exponent γ are constant in the limited q range investigated. In figure 47a the temperature evolution of γ is reported, in the different illumination conditions. At low temperature, $\gamma = 1.5$; in other words, $g^{(2)}(q;t)$ is described by a compresses, faster-than-exponential decay. At high temperature, both in dark and under UV light, the value of γ drops to values comparable

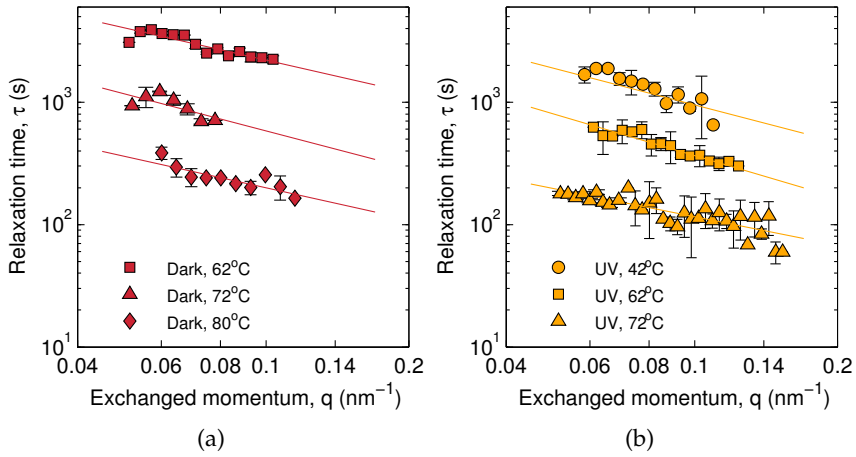

Figure 46: Equilibrium relaxation time τ measured as a function of the exchanged momentum q and at several temperatures, in dark (a) and under UV illumination (b).

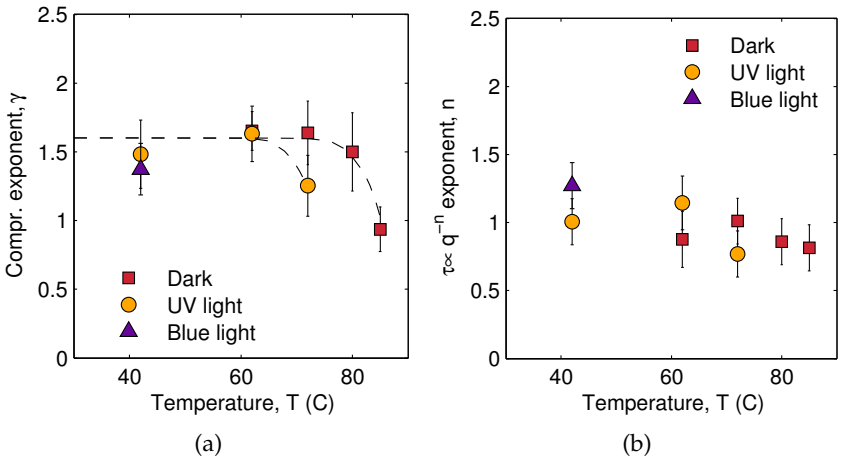

Figure 47: (a) Temperature and illumination dependence of the compression exponent γ. Dashed lines a re a guide to the eye. (b) Exponent n which describes the power law dependence of the relaxation time, measured for several illumination conditions and temperatures.

with 1, meaning the $g^{(2)}(q;t)$ decays a simple exponential. The exponent n obtained by the power law fits of the relaxation times $\tau \propto q^{-1}$ is reported as a function of temperature in figure 47b. In all the illumination conditions and temperatures investigated, n is roughly equal to unity, compatibly with the experimental errors.

These results can be interpreted within the Bouchaud-Pitard model (see chapter 7.3), built to describe the microscopic motion of systems characterized by an elastic mechanical response, such as PA4. Let's recall that the model predicts $\tau \propto q^{-1}$ along with a crossover in the compression exponent from $gamma = 3/2$ to $\gamma = 5/4$ at some characteristic time scale τ_q. We assume τ_q to be temperature dependent and to decrease upon heating following the temperature dependence of the viscosity; this could explain why the decay is observed as a function of temperatures. Moreover, we interpret our experimental result of the decrease of τ_q upon heating above $T = 80°C$ for PA4 in absence of illumination, and above $T = 65°C$ for PA4 in the *cis*, UV induced state, as support for such a crossover.

At the same temperature, relaxation times measured with the sample illuminated by UV light are sensibly faster than the ones measured in dark. In particular, figure 48a shows that the ratio of relaxation times measured under UV light and in dark, τ_{UV}/τ_{Dark}, is constant at all temperatures and equal to 0.2. This result is consistent with the reduction in the shear viscosity observed on the macroscopic scale by means of ISR, although on monolayers at the air/water interface. More surprisingly, the ratio τ_{Blue}/τ_{Dark} measured at $T = 42°C$ is equal to 0.1, meaning that a faster dynamics is observed under blue light photoperturbation. In section 10.1, rheological measurements on the macroscopic scale showed that the same photoperturbation

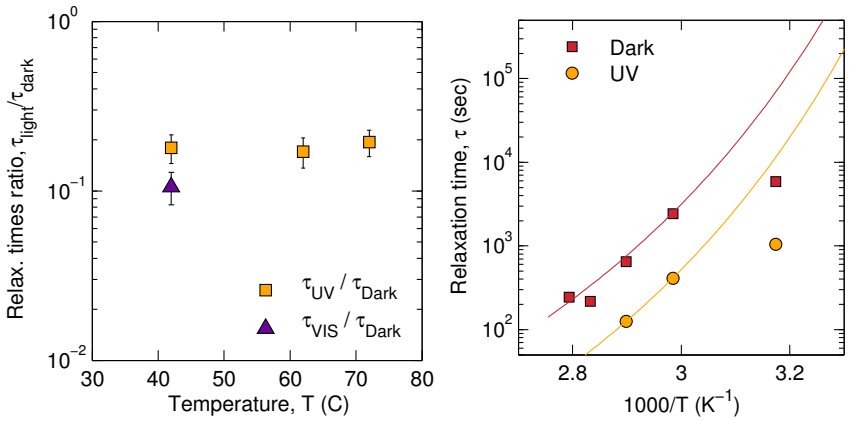

Figure 48: (a) Relaxation time τ as a function of temperature under UV and blue light photoperturbation, normalized by the correspondent relaxation time measured in dark, at $q = 0.1 nm^{-1}$.(b) Arrhenius plot of the relaxation times measured in the temperature range $40 - 90°C$, in dark and under UV illumination, at $q = 0.1 nm^{-1}$. Data are compared with the VFT curves (continuous lines) that describe the temperature dependence of the mechanical shear viscosity.

causes an increase in the shear viscosity, i.e. the film becomes more rigid. The *cis-trans* configuration cycling induced by blue light seems to cause fast molecular reorganization on the microscopic scale, leading to a macroscopically more rigid system.

Figure 48b reports an Arrhenius plot of the temperature dependence of the relaxation time τ measured at $q = 0.1 nm^{-1}$. Data are compatible with the VFT curves obtained from the analysis of the mechanical properties of PA4 monolayers at the air/water interface, with the exception of data measured at $T = 42°C$. This deviation could be due to the fact that the slow dynamics may start approaching the long-time stability of the experimental setup, which is limited by phenomena such as the drift of the synchrotron x-ray beam for the dark data, or radiation induced damage of the sample for the UV case.

11.1 DYNAMICAL HETEROGENEITY

In this section, the equilibrium dynamics of the system under UV illumination is characterized using higher order correlation function, investigating for the eventual presence of heterogeneous dynamics.

Figure 49 shows the two times correlation $C(q; t_1, t_2)$ measured under UV photoperturbation, at $T = 72°C$ and with exchanged momentum in the range $q = 0.05 - 0.08 nm^{-1}$. At all the values of q investigated, a close but qualitative inspection the two times correlation functions show that the relaxation time τ is roughly constant

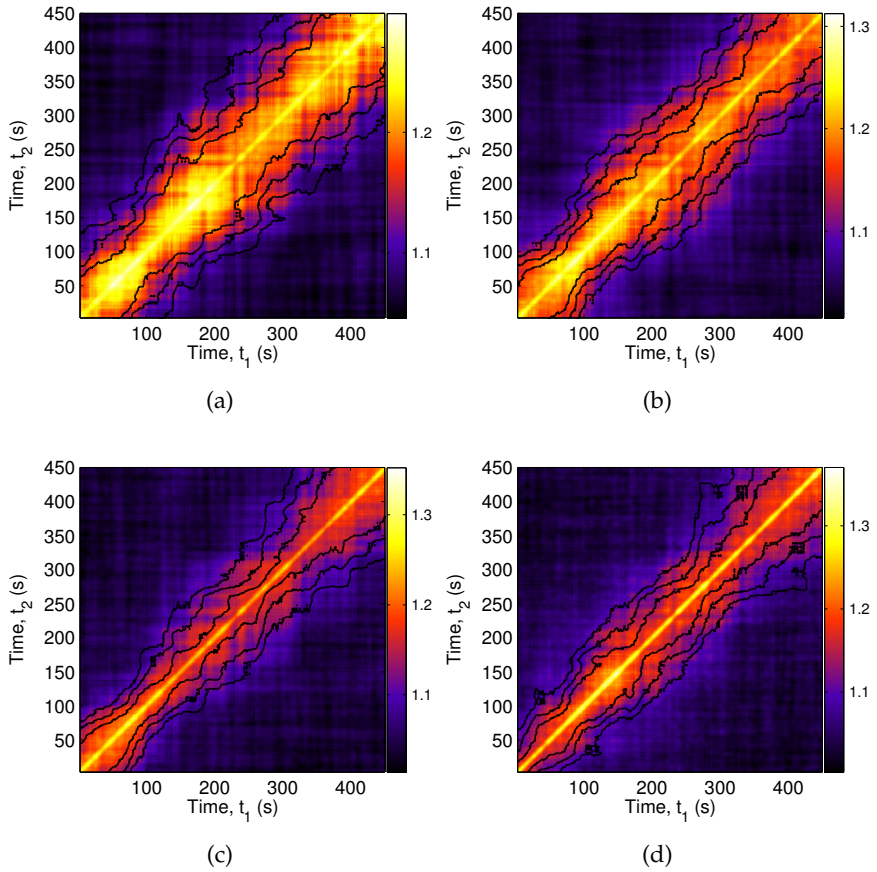

Figure 49: Two times correlation function $C(q; t_1, t_2)$ measured under UV illumination at $T = 72°C$ and (a) $q = 0.05 nm^{-1}$, (b) $q = 0.06 nm^{-1}$, (c) $q = 0.07 nm^{-1}$, (d) $q = 0.08 nm^{-1}$.

with time, although it seems to display fluctuations as a function of aging time. This statement is deduced by a qualitative analysis of figure 49, but it can be verified by the more refined approach that involves the calculation of the variance χ of $C(q; t_1, t_2)$, performed as outlined in section 7.4.

The variance χ, reported for several values of q in figure 50, presents a well defined peak in the time range between $10 - 50$ seconds, symptomatic of heterogeneous dynamics, only for data measured under UV illumination. No peak has been detected in absence of illumination. In figure 51 the position τ_C -(a) panel- and the intensity χ^* -(b) panel- are reported. It is worth noting that τ_C show the same proportionality with the inverse of q that was observed for the relaxation time τ. On the other hand , the intensity of the variance peak χ^* is found to be inversely proportional to the cube of the exchanged momentum, $\chi^* \propto q^{-3}$. Since χ^* is expected to be inversely proportional to the number of independent regions in the scattering volume that are responsible for the observed dynamical heterogeneity, the observed dependence is reasonable, assuming the characteristic size of

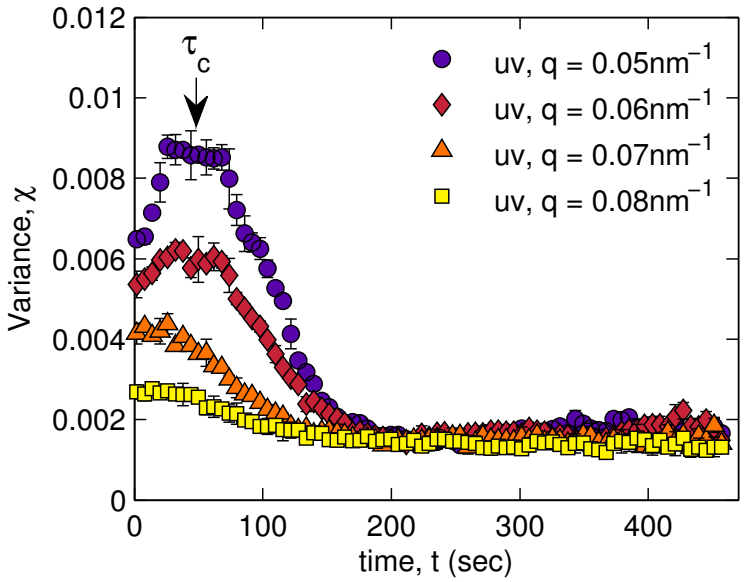

Figure 50: Variance χ of the two times correlation functions reported in figure 49, measured under UV illumination.

the regions to be proportional to the length scale probed $d = 2\pi/q$ at each value of the momentum transfer q.

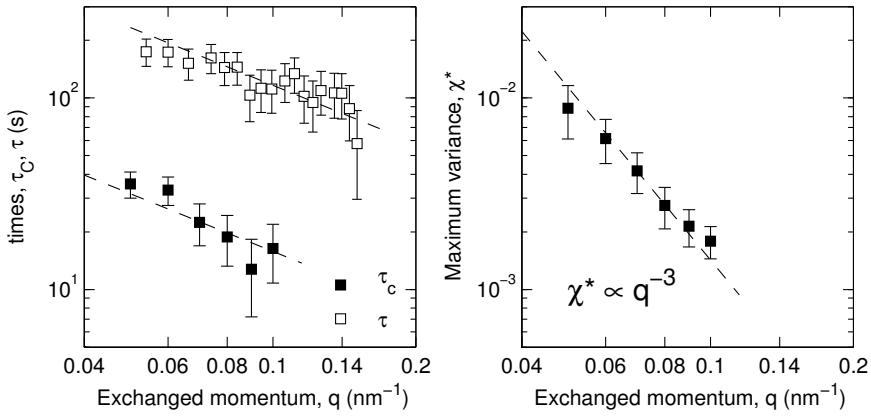

Figure 51: (a) Time position τ_C of the peak found in the variance $\chi(q;t)$ of the two times correlation function, measured under UV illumination at $T = 72°C$, reported as a function of q along with the corresponding relaxation time τ. Dashed lines are fit with q^{-1} dependencies. (b) Intensity χ^* of the peak of χ, measured in the same condition. Dashed line is the fit with q^{-3} described in the text.

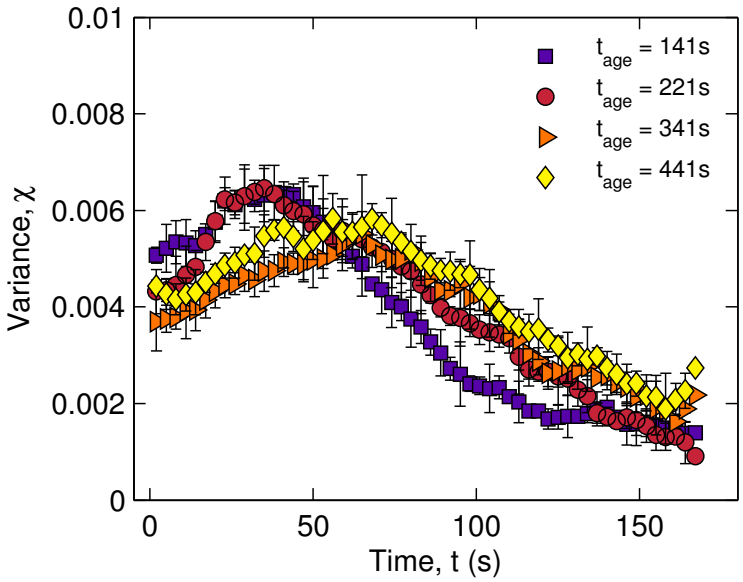

Figure 52: Aging evolution of the variance χ of two times correlation functions measured at different waiting time after the illumination with UV light. χ is reported for several waiting times, with zero time corresponding to the beginning of photoperturbation with UV light.

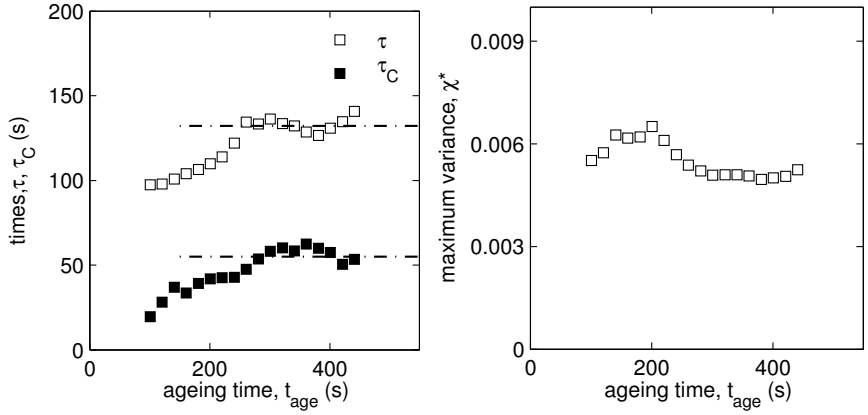

(a) (b)

Figure 53: (a) Time position τ_C of the peak in the variance of the two times correlation function $\chi(q;t)$, measured during UV photoperturbation at $T = 72°C$, reported as a function of aging time, along with the relaxation time τ. Dashed lines are a guide to the eye. (b) Intensity χ^* of the peak of variance χ, measured in the same conditions, reported as a function of the aging time.

11.2 OUT-OF-EQUILIBRIUM DYNAMICS

The previous sections report a deep characterization of the equilibrium dynamics in the different illumination conditions. This section

focus on the out-of-equilibrium *trans*-to-*cis* transition, induced by UV illumination.

Several correlation functions $C(t_1, t_2)$ were calculated at different waiting times t_{age}, measured after the time $t_{age} = 0$ at which the UV light was turned on. From each of these, a variance χ was calculated. A subset of variances are shown in figure 52. Unsurprisingly, the variance shows a peak, indicating that the UV-induced rearrangement dynamics is heterogeneous; this result is somehow expected, given the strong rearrangements of molecules induced in the sample by the external photoperturbation. The time position τ_C and the intensity χ^* of the peak of χ are measured as a function of the aging time, and they are reported respectively in panels (a) and (b) of figure 53. The evolution of τ_C indicates that an equilibrium state is reached after roughly 300 seconds, a result confirmed by the corresponding evolution of the relaxation time τ 300s calculated from single time correlation functions $g^{(2)}(q;t)$. Analogously, the intensity χ^* reaches a stable value at $t_{age} \simeq 300s$; we note that this time scale if compatible with the duration of the transition as probed by ISR, measuring the mechanical properties of a single monolayer of PA4.

Part V

STUDIED SYSTEMS: B) 2D NANOPARTICLE GELS

The mechanical response and the internal dynamics of 2D nanoparticle gels at the air/water interface are measured. Dynamical heterogeneities are characterized by means of four-times correlation functions.

12

2D GELS OF GOLD NANOPARTICLES

The second class of systems investigated in this work consists of 2D films of gold nanoparticles (GNPs) formed at the air/water interface.

Random 2D assemblies of GNPs are remarkably interesting from an applicative point of view, in particular in the field of non-linear optics[100], as catalyst for chemical reactions [101], for bio-inspired molecular electronics [20, 102], or even in medicine, diagnostics and therapeutics [12, 103, 104]. Moreover, 2D arrays of GNPs are used as substrates in Surface-Enhanced Raman Spectroscopy (SERS) experiments [105], capable of single-molecule investigations. Most of these recent applications of inorganic nanoparticles to nano-science are based on their adsorption at fluid-fluid or air/fluid interfaces [106, 107, 108], obtaining interesting experimental realization of ideal 2D systems.

The high variability of interparticle interactions of inorganic nanoparticles in granted by functionalization or coating with different polymers or molecular groups. An accurate tuning of the size and interparticle potentials of GNPs makes their investigation particularly useful to complement the theoretical investigation of interfacial systems, filling the gap of length scales between molecular surfactants and micron-sized particles.

This part of the project is focused on the study of monolayers of *weakly attractive gold nanoparticles* at the air/water interfaces. The following chapters report:

- the morphological characterization of GNPs Langmuir films, as a function of their surface concentration, with particular regard to the characterization of their morphology (and of its structural heterogeneity);
- the measurement of the mechanical response function of these films, performed by means of oscillating needle shear rheology, as a function of relative strain, frequency and surface concentration;
- the investigation of the internal dynamics of GNPs films by means of XPCS, as a function of surface concentration, focusing on the characterization of dynamical heterogeneities using four-times intensity correlation functions $g^{(4)}(q;t)$.

12.1 LANGMUIR FILMS OF THYOLATED GOLD NANOPARTICLES

Colloidal suspensions of GNPs, stabilized by a coating of dodecanethiol, were produced by Prof. Ruggeri and coworkers (University of Pisa) following the literature [109], by means of the reduction of hydrogen tetrachloroaurate(III) by sodium borohydride in methanol using mercaptosuccinic acid (MSA) as the stabilizing thiol ligand.

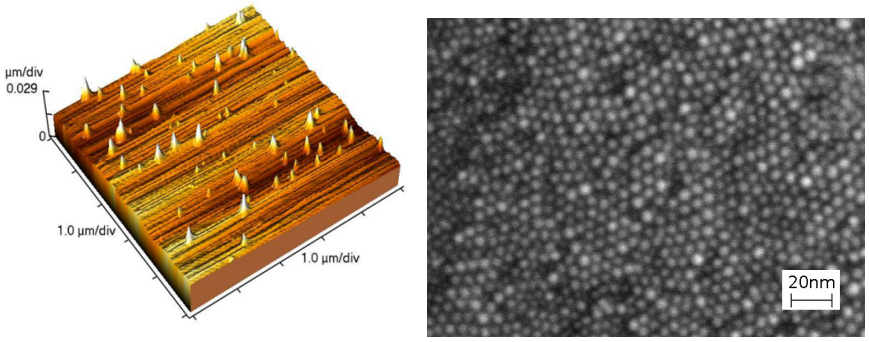

(a) (b)

Figure 54: a) AFM microscopy image of 7nm GNPs. b) SEM microscopy image of 7nm GNPs.

The two different batches of colloids used in the present study, with diameter 7nm and 80nm respectively, have typical distribution widths $\sigma = 5$Å and 20Å. The particles and their size distribution and polydispersity were characterized by means of AFM, SEM and TEM microscopies: examples of such measurements are shown in figure 54.

The size of the nanoparticles has been checked also by measuring the UV-Vis absorption spectrum, which is shown in figure 55. Spectra were measured on highly diluted hexane solution of GNPs. The estimation of the diameter, used to confirm the measurement obtained through SEM and TEM characterization, was evaluated from the position of the surface plasmon resonance peak of gold, following [110].

It must be noted that the dodecanethiol coating provides a hydrophobic interaction which stabilizes the particles when they are suspended in an organic solvent, so that the bulk suspensions are stable for months after preparation by an hard-sphere-like interaction. On the contrary, when spreaded at the air/water interface, the same organic coating provides a weakly attractive interaction between the particles. When two particles are brought closer, they are suddenly linked by the interdigitation of the hydrophobic dodecanethiol chains, so that water is expelled from the interparticle region. A very delicate branched 2D network structure is then formed, and it requires particular care in handling.

To form the Langmuir monolayer, an hexane-chloroform 9 : 1 suspension of gold nanoparticles, with optical density 0.48abs/cm, was spread on the water surface using a 50µl Hamilton syringe. The

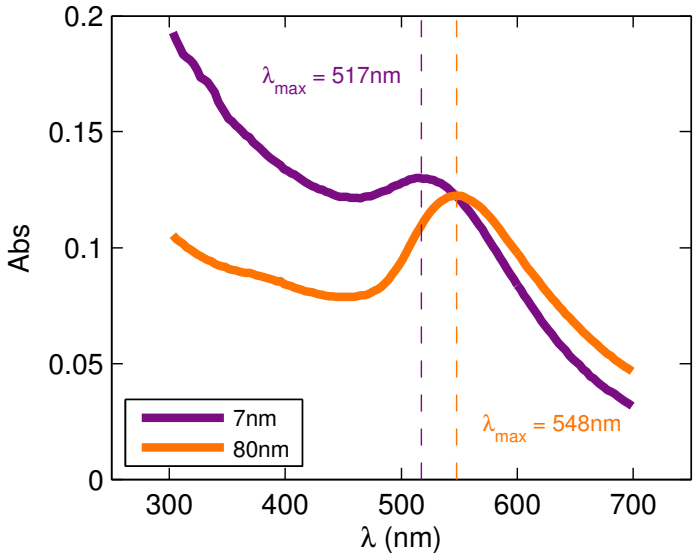

Figure 55: UV-Vis absorption spectra measured on diluted solutions of gold nanoparticle of diameter 7nm and 80nm.

spreading of a single syringe of solution, performed while keeping the tip of the needle in contact with the water surface, required roughly 5 minutes, with frequent changes of the position of the needle's tip on the water surface. This was followed by a waiting time of 5-10 minutes, included to ensure complete solvent evaporation. The procedure was repeated to reach the total amount of 400µL of solution spread, for a total spreading time of roughly one hour. Subsequently, the compression was started; successive cycles of very slow compression/expansion motions of the barriers were applied between the pressures of $\Pi = 3\text{mN/m}$ and $\Pi = 5\text{mN/m}$, repeating the cycles at increasing pressure up to a maximum value $\Pi = 9\text{mN/m}$, at constant temperature of $T = 15°C$, in a similar way as reported in literature [111]. Measurements were then performed at constant temperature ($T = 18°C$) and increasing surface pressure, ranging from $\Pi = 10\text{mN/m}$ up to $\Pi = 30\text{mN/m}$.

Figure 56 reports a compression isotherm obtained following this procedure, that produce an irreversible compaction of the Langmuir film. The required number of cycles (around 5) is empirically determined by observing when they do not produce a further increase of the packing of the film. As explained in chapter 4.1, if the film presents an high shear modulus, the surface pressure is to be replaced by the tensor of the stresses, and therefore the reading of Wilhelmy plate depends also on its relative orientation with respect to the moving barriers [112, 113]. Keeping this in mind, the isotherms as well as all the rheological measurements presented in this work were performed while keeping the Wilhelmy plate always in the same ori-

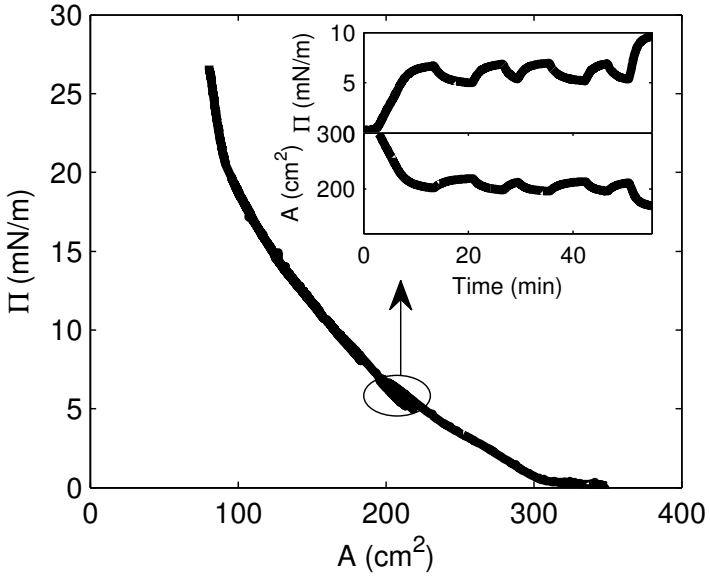

Figure 56: $\Pi - A$ isotherm of a Langmuir film of GNPs (diameter: 80nm). The insets show in detail the compression-expansion cycles described in the text.

entation, i.e. perpendicular to the moving barriers of the Langmuir trough.

12.2 MORPHOLOGY AND SURFACE CONCENTRATION

The morphology of the films formed at the air/water interface has been directly observed by means either of Brewster Angle Microscopy (BAM) or Null-Ellipsometry in imaging mode. Ellipsometry measure-

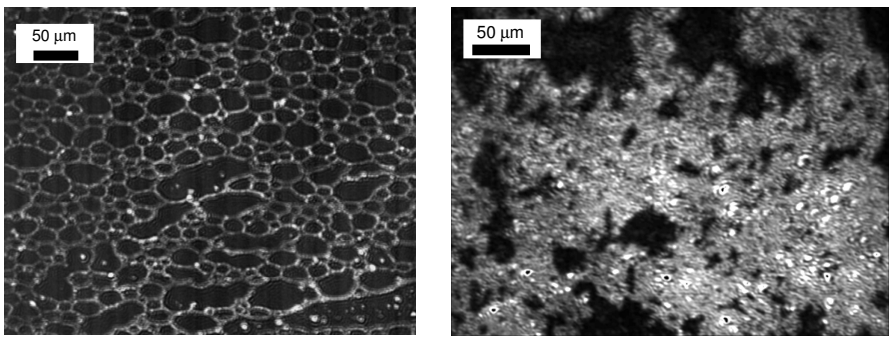

(a) (b)

Figure 57: a) Brewster Angle Microscopy (BAM) and b) Null-Ellipsometriy images of a Langmuir monolayers of GNPs, respectively at $\Phi = 33\%$ and $\Phi = 71\%$ respectively.

ments were performed with an angle of incidence of 22° with respect to the vertical direction, thus obtaining a wider field of view with

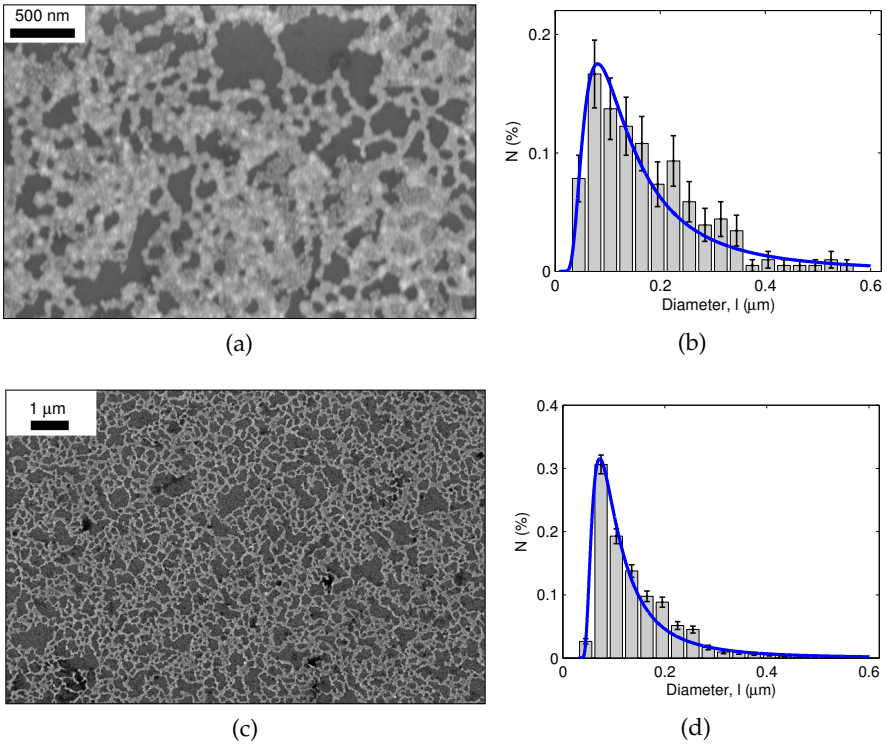

Figure 58: SEM images of GNPs monolayers transferred on silicon ($\Phi = 69\%$) along with the correspondent histograms of the void diameters, compared with the Levy distribution (blue line) given in equation 12.1 (algebraic exponent $\alpha \simeq 3$). a-b) Magnification 100k, c-d) magnification 10k.

respect to that obtained at air/water interface's Brewster angle (53°). At low surface pressure, a foam-like structure is observed (see figure 57a), with at higher surface pressure, above $\Pi = 20 mN/m$, the structure of the film is more compact. This compact film still shows irregular holes at all the spatial scales, as shown in figure 57b.

This irregular morphology can be quantitatively investigated by the analysis of films transferred on solid substrate. Typical SEM images, recorded at 100k and 10k magnification, are shown in the left panels of figure 58. They confirm the presence of structural heterogeneity in the morphology of the system, with the presence of clusters and holes. The size of these structures varies on a broad range, from few tens of nanometers to several microns.

The distributions of hole sizes calculated from these images are shown in the right panels of figure 58. They were calculated by extrapolating a mean diameter, approximating the holes as circles. The distributions, peaked roughly at $l = 100 nm$, are strongly asymmetrical and compatible with a Levy distribution function [114]

$$N(l) \propto \frac{\exp^{-\frac{c}{l-\mu}}}{(l-\mu)^{\alpha}}. \tag{12.1}$$

In this equation,

- α is the tail exponent, which defines how the distribution decay at large values of the diameter;
- μ is called *location parameter* and can be viewed as the "minimum diameter" of the distribution;
- c is the *scale parameter*, defining the width of the distribution: an higher value of c corresponds to a larger distribution.

The distributions measured at 100k and 10k magnification are both characterized by an algebraic tail with exponent $\alpha \simeq 3$. The location parameter μ decreases as the magnification is raised, as expected; in fact, the value of μ corresponds to the smaller hole that can be distinguished in the image. On the contrary, the scale parameter c (and the distribution width) is almost constant among error bars; the two distributions have comparable widths.

A summary of the fitting parameters is reported in table 5.

Magnification	10k	100k
$\mu(\mu m)$	0.030 ± 0.003	0.01 ∓ 0.005
$c(\mu m)$	0.25 ± 0.03	0.4 ± 0.2
α	3.0 ± 0.1	2.9 ± 0.2

Table 5: Parameters retrieved from the fit with equation 12.1 of the SEM image hole size distributions of films of gold nanoparticles.

No crystalline phase was detected neither by in-situ GID nor by SEM imaging in the direct space, even in films transferred at high surface pressure, where an higher fraction of area covered by the film, and a possible crystalline phase was more likely to appear.

The fraction Φ of surface covered by the film is usually deduced from the dispersed aliquot. The precise determination of Φ is particularly relevant [115] in the discussion of the results of ISR and XPCS experiments, reported in the following chapters. Therefore, its determination from the volume of solution spreaded at the interface was double checked *in situ* by null-ellipsometry and *ex situ* by SEM imaging of monolayers transferred onto a solid substrate. The three independent determinations coincide, as shown in figure 59, making us confident of the accuracy of Φ.

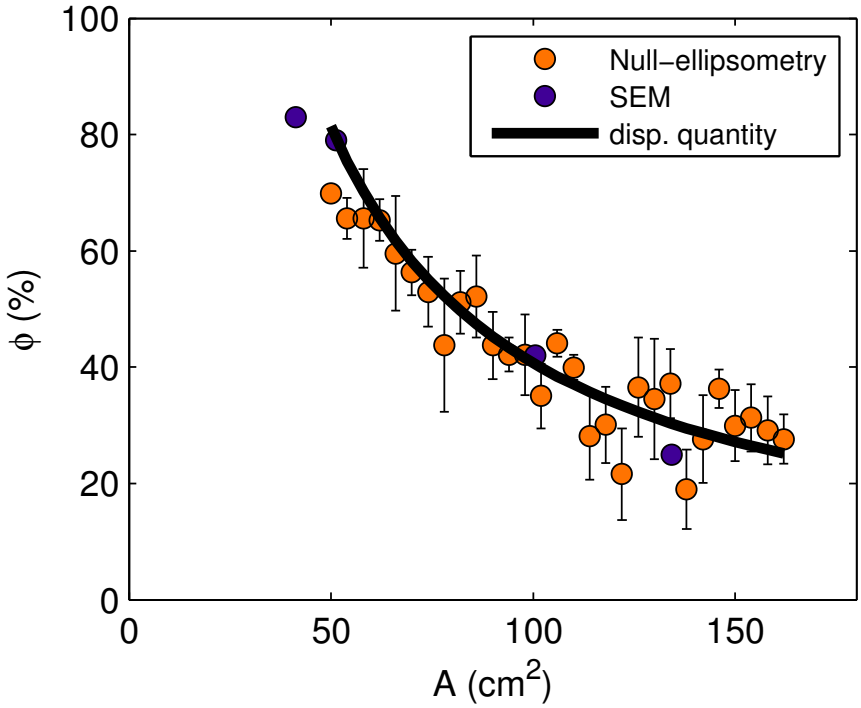

Figure 59: Evaluation of surface concentration Φ as a function of the trough Area, obtained from Null-ellipsometry measurements, analysis of SEM images, and from the spreaded amount of sample.

13

INTERFACIAL ELASTIC RESPONSE

The mechanical response of the film has been characterized using the oscillating needle interfacial rheometer described in chapter 4.1.

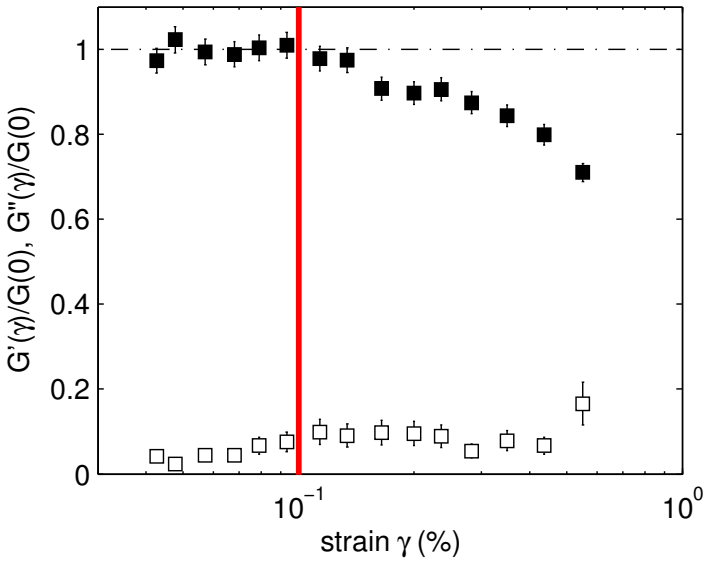

Figure 60: Storage and loss moduli G' and G'' measured on a Langmuir film of GNPs (diameter 80nm) as a function of its relative strain. The measurement was performed at constant frequency $\omega = 3.14 rad/s$.

The first characterization was performed at constant frequency $\omega = 3.14 rad/s$, while varying the stress exerted on the Langmuir film. The dynamic shear moduli G' and G'' obtained from this measurement are reported in figure 60 as a function of the relative stress $\gamma_r = |\gamma|/H$, where H is the distance that separates the magnetic needle and the glass channel. The mechanical response is constant for $\gamma_r < 0.1\%$, while for higher strain the storage modulus G' drops. This phenomenology is known as *strain softening*, typical of many soft gel systems.

The loss of elasticity is due to the rupture of the weak links that form the gel structure formed at the air/water interface, caused by the excessive amplitude of the movement of the needle when $\gamma_r > 0.1\%$. We can identify a critical strain rate $\gamma' = 2 \cdot 10^{-3} sec^{-1}$ as the limit below which the modulus is strain-rate independent. All the measurements reported here have been performed while maintaining the strain rate well below this threshold, in the *linear regime* of the mechanical response.

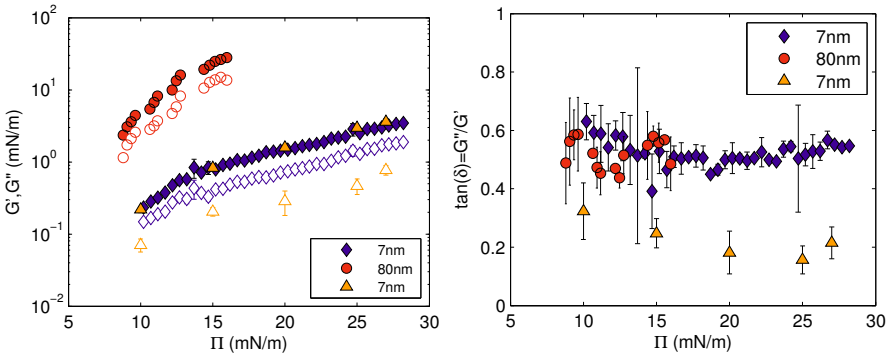

(a) (b)

Figure 61: ISR measurements on films of GNPs (80nm and 7nm diameter), performed with the oscillating needle technique at $T = 18°C$. a) Dynamic shear moduli G' and G'' as a function of the surface pressure Π. b) Loss factor $\tan(\delta)$ reported a function of surface pressure Π.

Figure 61 shows the evolution of the dynamic shear modulus (a) and of the loss factor (b), a s a function of Π. The measurements indicated as circles (80nm) and diamonds (7nm) were performed at constant frequency $\omega = 3.14 rad/s$ during compression of the Langmuir film at constant barrier velocity, as it is done while measuring a $\Pi - A$ isotherm. As the area is reduced, and the surface pressure increases, $|G|$ steadily increases while $\tan(\delta)$ shows little evolution, decreasing slightly and reaching a limit value close to 0.5. Therefore, the mechanical response of films formed by particles of either 7nm and 80nm diameter is mainly elastic even at the lowest concentration studied, confirming that a gel network has been formed. This result seems to be independent from the procedure followed to form the Langmuir film, since it has been observed both in a film formed with the compression-expansion cycles and in a film formed without such a preliminary preparation. Hence, we suppose that the behavior of $\tan(\delta)$ is related to the interparticle interaction more than to the mesoscopic structure of the film. A similar evolution of mechanical moduli as a function of aging time has been recently found in thermotropic colloidal gels [116]. On the contrary, the modulus $|G|$ clearly depends on the diameter of the particles, which is reasonable for a gel presenting formation of irreversible links during compression.

We compare these results with measurements performed after a waiting time of 5 minutes following the end of the barrier's motion necessary to reach each surface pressure (triangles). We note that, while the storage modulus G' is unchanged, the loss modulus G''- and $\tan(\delta)$- is reduced by a factor of 2.5. This finding helps to clarify the origin of the dissipation response of the film, which is likely to be related to the presence of *dissipative friction* between the particles, in

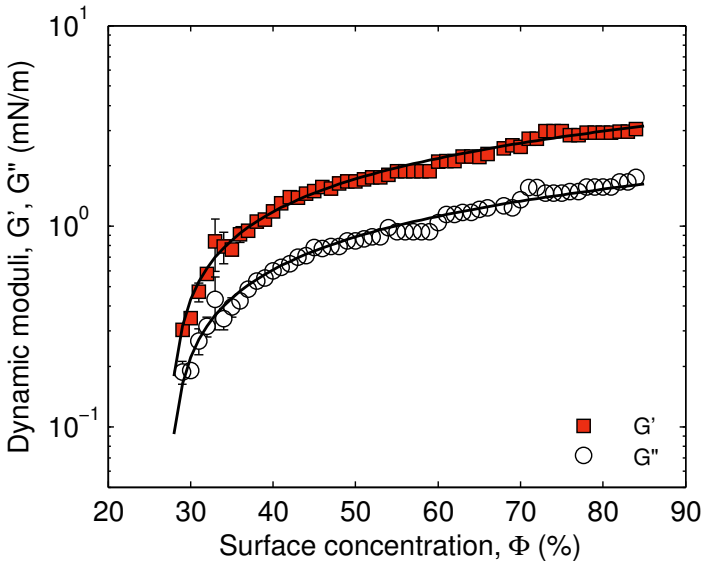

Figure 62: Storage and loss moduli G' and G'', measured on a Langmuir film of GNPs, reported as a function of the surface concentration Φ.

particular at high surface concentration. This contribution is stronger when the system is much out of equilibrium (steady compression); at the same time, it is less pronounced when the system is allowed to relax toward a stationary gel state, waiting for some minutes after the end of the barrier motion before starting the measurement.

The mechanical shear moduli are reported in figure 62 as a function of the surface concentration Φ of nanoparticles at the air/water interface. Both G' and G'' are found to obey a power law like $G \propto \widetilde{\Phi}^z$ in which the power law exponent $z = 0.65(1)$ is the same for all the three quantities, and $\widetilde{\Phi}$ is the reduced concentration $\widetilde{\Phi} = \frac{\Phi - \Phi_0}{\Phi_0}$, thus defined by scaling the concentration to a reference value $\Phi_0 = 0.27(1)$. Noteworthy, Φ_0 is close to that at which the gel was compacted by the expansion/compression cycles. Analogous results were found for films of 80nm particles.

Similar power law scaling behaviors of elasticity post gel-formation have been found in many bulk systems, and they are related to the underlying physics of percolation [117, 118]. The value of $z = 0.65$ measured here for the growth of two-dimensional G is weaker than 2.4 observed in protein gels [119] or 4.0 in carbon black gels [120]. However, both are 3D systems: a dependence on dimensionality is to be expected. There is less comparable data in 2D, but approximately linear growth of G for protein layers can be seen in [52].

The frequency dependencies of G' and G'' are shown in figure 63a and 63b. The storage modulus is almost constant in the frequency range here probed, with only a slight frequency dependence on the lower frequency side, which becomes more apparent at the highest

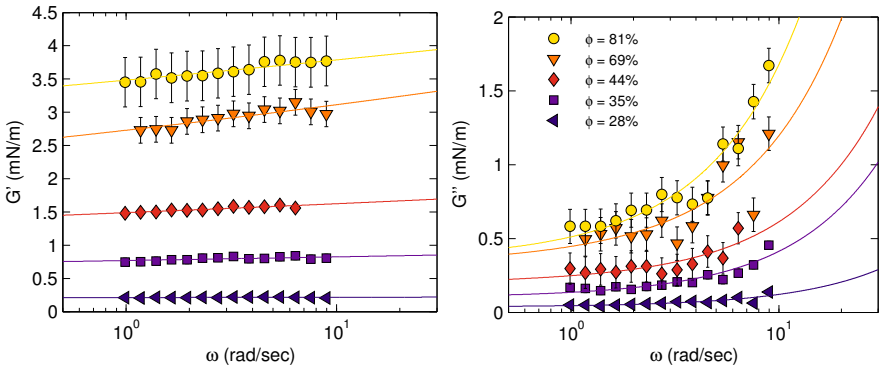

(a) (b)

Figure 63: a) frequency dependence of the storage modulus G' measured at $T = 18°C$, for several values of the surface pressure b)frequency dependence of the loss modulus G'', measured in the same conditions.

covered fractions. The loss modulus is, on the contrary, almost constant at low frequency, crossing over to a linear increase at the higher frequencies. It should also be remembered that it remains always smaller than G'. This complex behavior can be rationalized in the framework of a widely used model for the soft glass rheology (SGR) [121].

This viscoelastic model is an extension to the field of rheology of models, such as the trap model, commonly used in glass physics to describe systems under aging [78]. The SGR model predicts that G' and G'' follow, at sufficiently low frequencies, the same power law with exponent $m = x/x_g - 1$. Here x is an effective noise temperature and x_g a glass transition temperature, below which the system dynamics is time-dependent, in the sense that it shows aging. In the

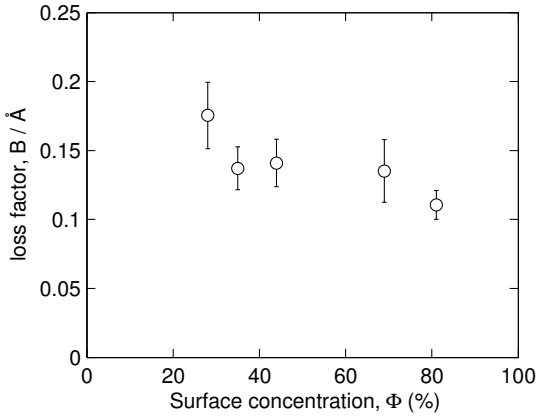

Figure 64: Cocentration dependence of the loss factor B/A obtained from the fit of the frequency dependencies of G' and G'' using equations 13.1.

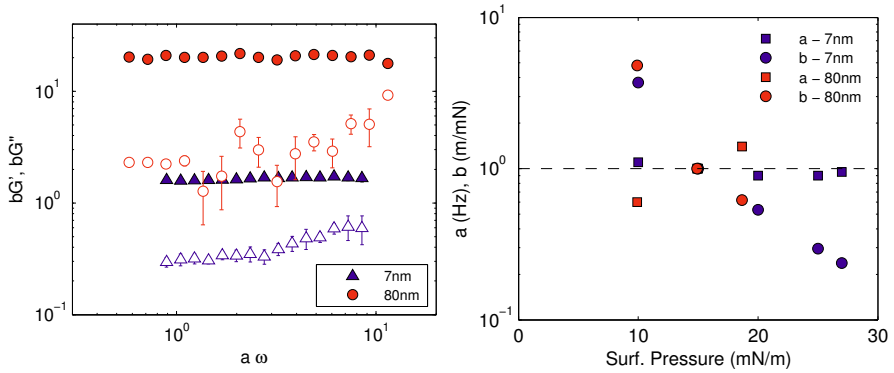

(a) (b)

Figure 65: a) Master curves obtained from the measurement of the frequency dependence of G' and G'' at several values of the surface pressure. b) master curves parameters a and b reported as a function of surface pressure Π.

same frequency range the loss factor, $\tan(\delta)$, is predicted to be proportional to m. Hence for small values of m the model is suitable to describe an essentially elastic material. In this framework, the complex shear modulus is described by the following equations:

$$G' = A\omega^m$$
$$G'' = B\omega^m + \eta\omega \tag{13.1}$$

where $m(\Phi)$, $A(\Phi)$, $B(\Phi)$, $\eta(\Phi)$ are the free parameters of the model.

The purely viscous, or linear, term in G'' is not part of the SGR model itself; it is observed in many systems, and can be added to the model to account for the contribution coming from the suspension viscosity η [122, 56]. The continuous lines in figures 63a and 63b are obtained fitting simultaneously $G'(\omega)$ and $G''(\omega)$ for each measured packing fraction. The values of the exponent m range between 0.01 and 0.06. This could mean that the system is close to a transition towards an aging state of the dynamics. However, it is difficult to draw any conclusion, since m is more likely to be zero, compatibly with the error bars.

The ratio between the parameters B and A (the $\tan(\delta)$ of the SGR contribution) is always greater than 0.1 and almost constant as a function of the covered fraction, as shown in figure 64. We are thus confident that what we see is not an artifact of the measurement, since the ISR instrument is sensitive to such values of $\tan(\delta)$. On the contrary, viscosity η increases with the surface concentration Φ.

The frequency dependent mechanical moduli measured at several values of concentration Φ for either 7nm and 80nm nanoparticles, can be superposed to form a mastercurve. The superposition is obtained following a robust two step rescaling of each data set: the first step consists in a shift of both G' and G'' by the same factor b; the

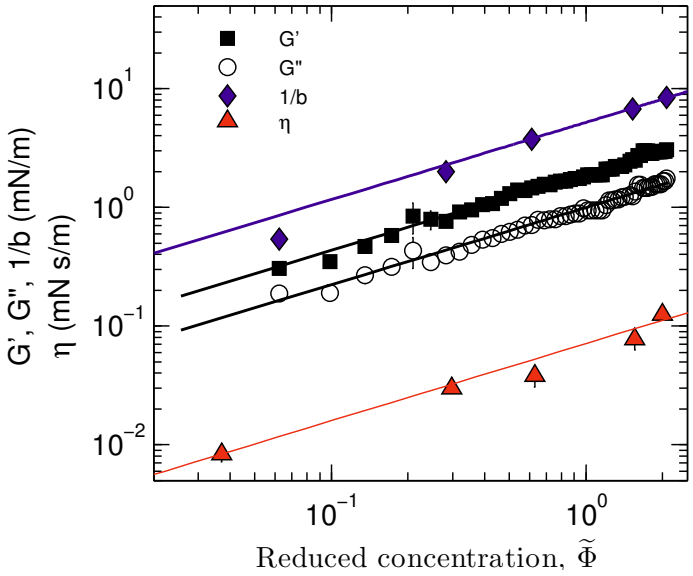

Figure 66: The dynamic shear moduli G' and G'', the inverse of the mastercurve scaling parameter b and the viscosity η as a function of surface concentration. Continuous lines are fit with the power law of the reduced concentration

second step is done by multiplying the frequencies by a factor a. The master curves obtained are reported in figure 65. Since the frequency dependencies of G' and G'' are quite similar at all the values of Π considered, the shifting procedure was mainly performed along the y-axis. Therefore, the parameter a -representing the shift along the x-axis- is constant over Π (i. e. over the surface concentration Φ) and close to 1, as shown in figure 65b.

The inverse of the scaling parameter b -obtained from the mastercurve building procedure- and the viscosity η -governing the loss modulus frequency behavior in the SGR model- scale (as expected, given how they are obtained) with the surface concentration Φ in the same way as the shear moduli G' and G''; these quantities are reported in figure 66, along with the fits with the power laws described above in this chapter, confirming the overall consistency and reproducibility of the different measurements.

14 XPCS MEASUREMENTS OF 2D GEL DYNAMICS

The internal dynamical fluctuations of the 2D gel formed by gold nanoparticles at the air/water interface have been measured at the beamline ID10A (ESRF) using the experimental setup detailed in chapter 8.2.

Interestingly, we note that the correlation functions measured at the same value of $q_{||}$, but at different values of $q_{\perp}$, are identical; they decay with the same relaxation time. In the left panels of figure 67 we report the correlation functions measured at several values of $q_{||}$ and at $q_{\perp} = 0.005\text{Å}^{-1}$. Each panel refers to a different surface concentrations of the 2D gel. The panels on the right of the same figure, on the contrary, report the very same correlation functions as a color map, function of $q_{||}$ and of the correlation time t. In these images, the relaxation time τ obtained from the fits with the KWW exponential are reported as white lines. Note that the correlation functions, as well as τ, relax faster as $q_{||}$ increases.

14.1 ANISOTROPIC DYNAMICS

In figure 68, the relaxation time τ is shown as a map, as a function of $q_{||}$ and $q_{\perp}$. Each panel refers to a different values of the concentration Φ. The dynamics is clearly anisotropic, with the relaxation time scaling along $q_{||}$ while remaining constant along $q_{\perp}$. This result indicates that the slow dynamics probed by the correlation functions $g^{(2)}(q;t)$ is confined at the air/water interface.

Hence, from now on the relaxation times of the 2D slow dynamics are averaged along the $q_{\perp}$ direction. Correlation functions were fitted with KWW exponentials. A compression exponent $\gamma = 1.5$ is found at all the values of $q_{||}$, $q_{\perp}$ and Φ probed. Henceforth in the subsequent analysis, the value $\gamma = 1.5$ has been kept fixed.

The q-dependence of the relaxation time τ is reported in figure 69, for several values of Φ. At all the concentrations investigated, τ in roughly inversely proportional to $q_{||}$, in particular $\tau \propto q_{||}^{-n}$ with $n = 0.8(1)$.

At the same time, from these curves we obtain the Φ-dependence of τ, reported in figure 70. The relaxation time grows with increasing surface concentration, compatibly with the behavior found for elastic shear modulus G' on the very same sample:

$$\tau = \tau_0 \left(\frac{\Phi - \Phi_0}{\Phi_0} \right)^z \tag{14.1}$$

with $\Phi_0 = 27\%$ and $z = 0.65$.

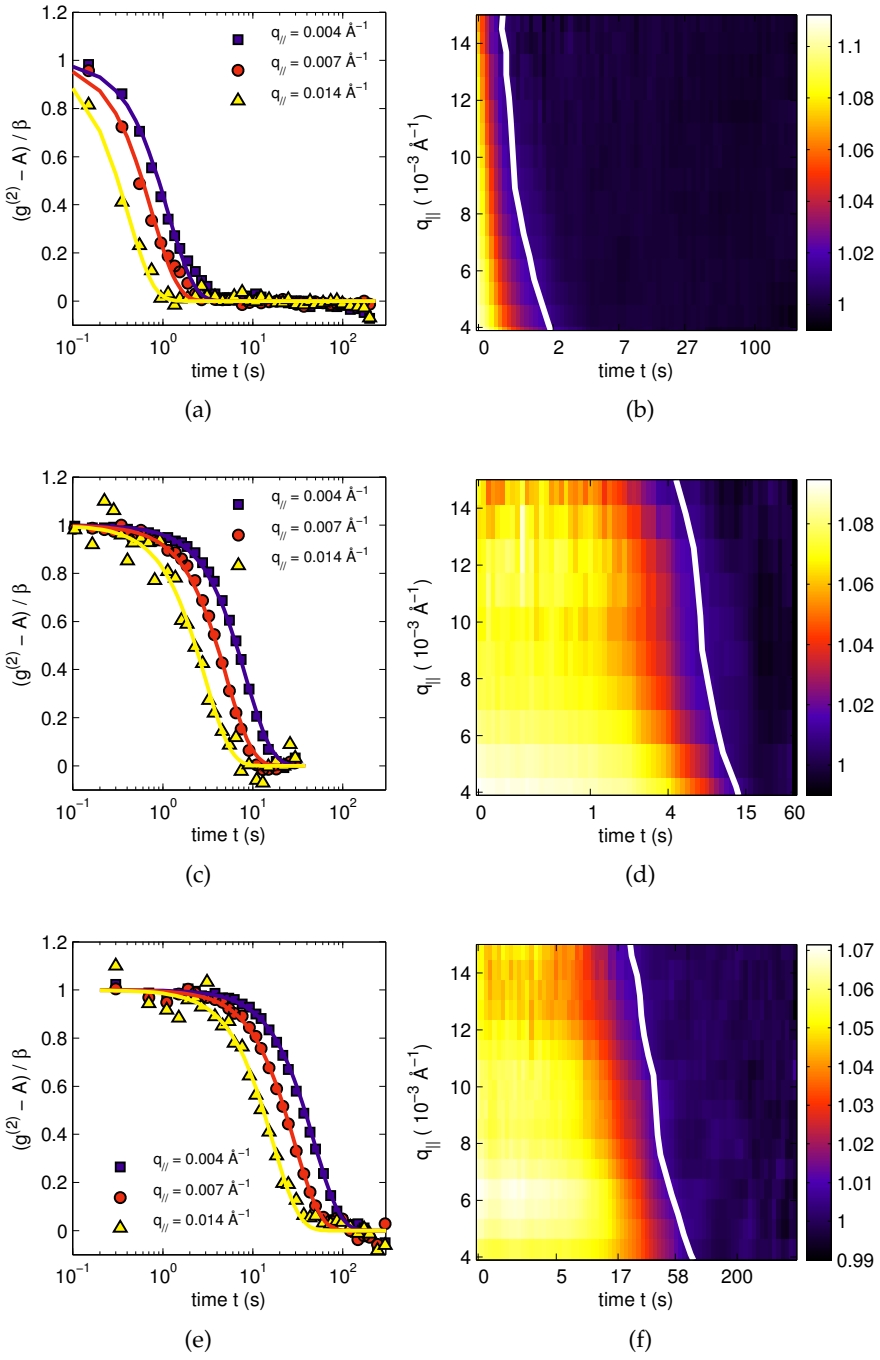

Figure 67: the panels on the left report correlation functions measured at several values of $q_{||}$; continuous lines are fits with KWW exponentials. The same correlation functions are reported in the panels on the right as a function of $q_{||}$ and of the correlation time t; white lines represent the relaxation time τ obtained from the fits.
a,b) $\Phi = 35\%$; c,d) $\Phi = 69\%$; e,f) $\Phi = 88\%$.

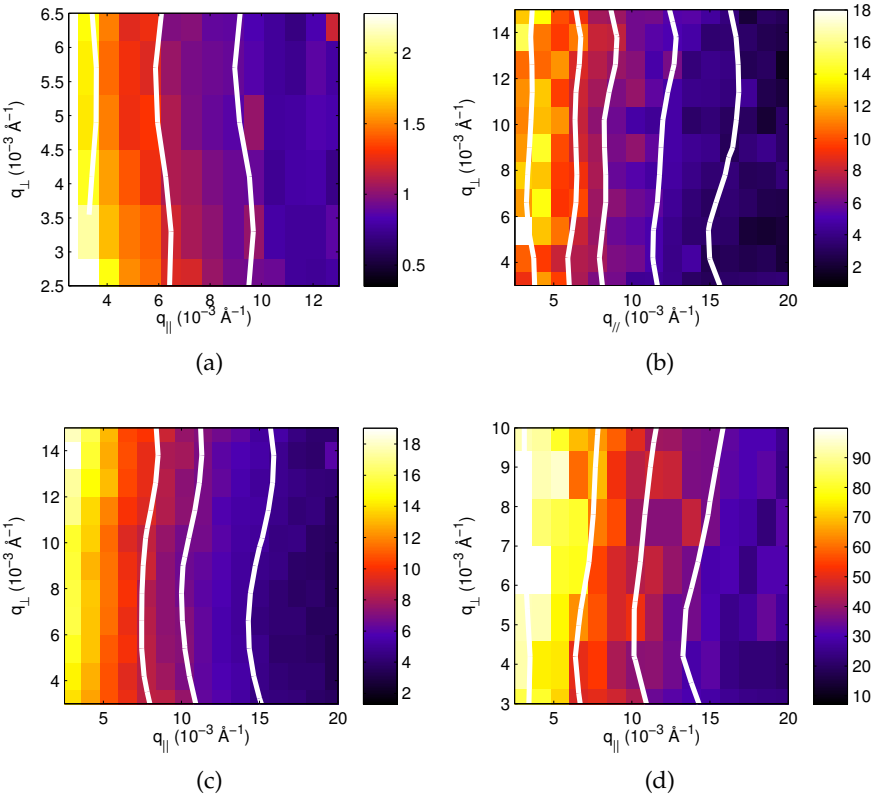

Figure 68: Maps of the relaxation time τ as a function of the components of the exchanged momentum, $q_{||}$ and $q_{\perp}$, measured at a) $\Phi = 35\%$, b)$\Phi = 69\%$, c)$\Phi = 81\%$ and d)$\Phi = 88\%$. The color-bar scale values are expressed in seconds. White lines are isochronous curves.

These results are compatible with the predictions of the Bouchaud-Pitard model detailed in chapter 7.3, describing the internal fluctuations of an elastic solid, such as the 2D gel currently under investigation. In particular we briefly recall here that in this model, the dipoles of forces induced by rearranging stresses in the elastic gel network imply that:

- the correlation functions $g^{(2)}(q;t)$ follow a compressed, *faster-than-exponential* decay with compression exponent $\gamma = 1.5$;
- the relaxation time decais with the inverse of the exchanged momentum
$$\tau \propto q^{-1};$$
- the relaxation time is proportional to the elastic shear modulus G'
$$\tau \propto G'$$

.

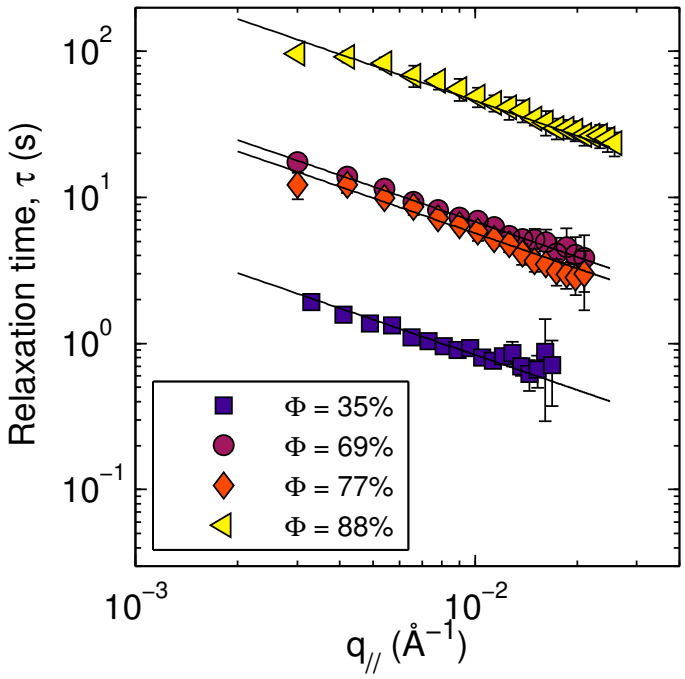

Figure 69: Relaxation time τ as a function of the parallel component of the exchanged momentum, $q_{||}$, at several values of the surface concentration.

This results can be view as an experimental confirmation of the validity of a generalized fluctuation-response function theorem in the 2D gel of gold nanoparticles. However, we must recall that the Bouchaud-Pitard model predicted a proportionality between the relaxation time and the *dilational* elasticity. An analogous coupling for shear elasticity is supposed by the authors [73].

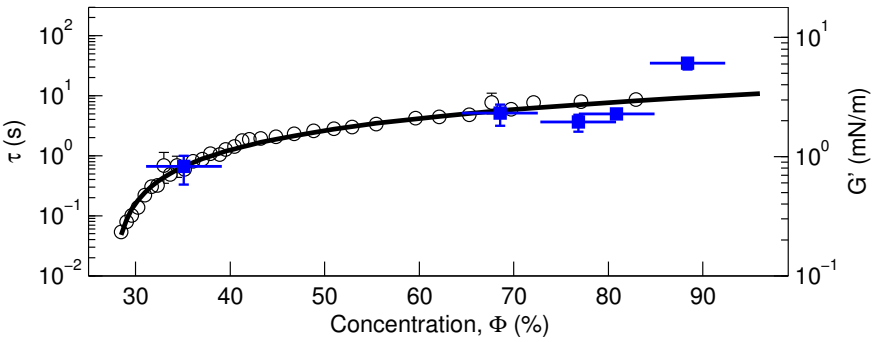

Figure 70: Relaxation time τ as a function of the surface concentration Φ (blue squares), compared with Φ-dependence of the storage modulus G' (circles). The continuous line is a fit with the power law of the reduced concentration $\widetilde{\Phi}$ described in the text.

14.2 DYNAMICAL HETEROGENEITIES

To check if the slow dynamics is the only surface dynamics of the sample, it is not possible to rely exclusively on intensity autocorrelation functions. As a matter of fact, the analysis of $g^{(2)}(q;t)$ characterize dynamics within a given time window, whose short-time limit is mainly determined by the amount of scattered intensity and by the detector speed. In our experiment, the signal intensity did not allow acquisitions with exposure time faster than 0.01 sec.

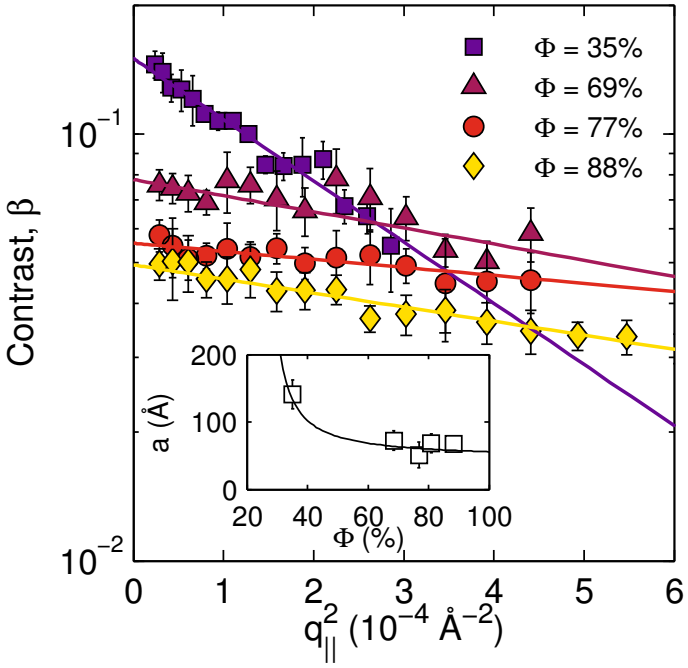

Figure 71: Contrast β of the correlation function $g^{(2)}(q;t)$, reported as a function of $q_{||}{}^2$. It follows a Debye-Waller decay, with exponent related to the localization length a. Inset) localization length a reported as a function of the surface concentration Φ.

A different strategy is required. As a starting point, we report the investigation of the dependence of the contrast β on the exchanged momentum q. As a matter of fact, any dynamics faster than the exposure time may reduce the contrast of the correlation function from the *Siegert factor*, which is roughly equal to 0.2 in this configuration of the experimental setup. This it what is observed in this work, as clearly shown in figure 71.

Information on this motion, if present, can be obtained from the q-dependence of the contrast β, which follows a pseudo Debye Waller law [116, 72, 123] parametrized by the localization length a:

$$\beta = \beta_0 \exp\left(-\frac{q^2 a^2}{3}\right) \tag{14.2}$$

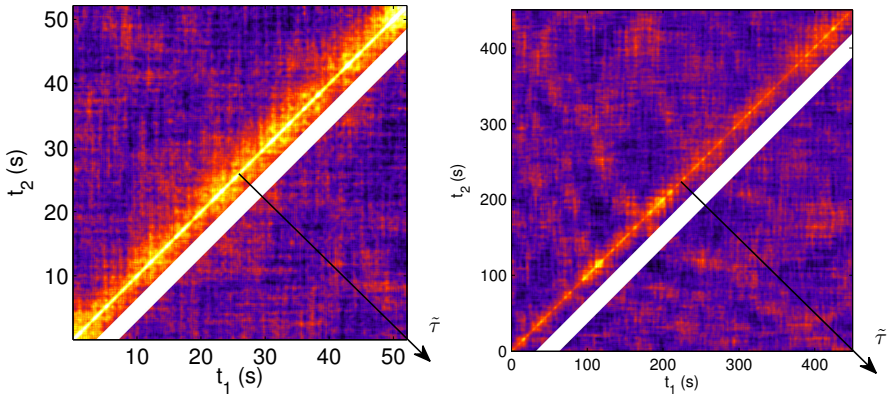

(a) (b)

Figure 72: two times correlation functions measured at $T = 18°C$, $q_{||} = 0.009\text{Å}^{-1}$, $q_{\perp} = 0.004\text{Å}^{-1}$ and surface concentration a) $\Phi = 69\%$, b) $\Phi = 88\%$. The arrow represents the direction along which the lag time $\tilde{\tau}$ grows. The white stripe indicates the value $\tilde{\tau} = \tau_C$ where $g^{(4)}(q;t)$ is calculated.

The fits are displayed in figure 71. The inset shows the variation of a as a function of increasing surface concentration Φ: the localization length decreases to reach a limiting value of 50Å. This value is comparable with the radius of the particles; this result provides a direct confirmation of the presence of increasing caging effects -and subsequent dynamical arrest- as the surface concentration increases.

We note that the extrapolation of β to $q_{||} = 0$ never reaches the Siegert factor; this suggests heterogeneity: during each exposure, only a fraction of particles remains localized within the length scale a, while the remaining population is more mobile, traveling over distances longer than $1/q_{min} \simeq 250\text{Å}$ [116].

As detailed in chapter 7.4, higher order correlation functions are a key tool to access and fully characterize the dynamical heterogeneity of the sample dynamics. Figure 72 reports the two times correlation functions $C(q, t_1, t_2)$ measured at $q_{||} = 0.009\text{Å}^{-1}$, $q_{\perp} = 0.004\text{Å}^{-1}$ and surface concentration $\Phi = 69\%$ (left) and $\Phi = 88\%$ (right). Both correlation functions shows a stationary slow dynamics, represented by contour lines that are parallel to the main diagonal. Therefore, the presence of aging on the temporal scale investigated by the experiment can be excluded.

In order to confirm the presence of heterogeneous dynamics in the sample, the "standard" approach involves the calculation of the variance $\chi(\tilde{\tau})$ of these two-times correlation functions, as already done in this project on films of the photosensitive azopolymer PA4.

The variance χ measured for surface concentration $\Phi = 88\%$ is reported in figure 73, for several values of q. The presence of a very

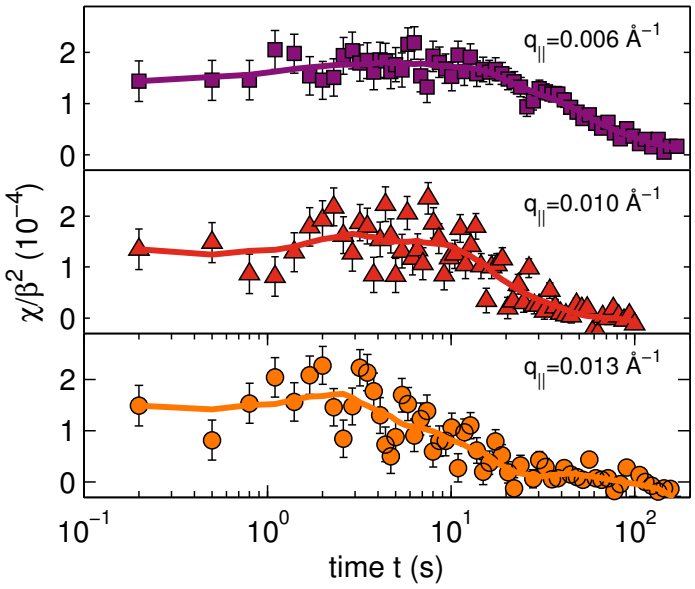

Figure 73: Variance χ of the two-times correlation function, measured on a film of GNPs at $\Phi = 88\%$, for several values of $q_{||}$.

broad peak seems to confirm that the dynamics of the sample is heterogeneous.

The position τ_C of the peak seems to be shifted towards faster times as the exchanged momentum is increased, compatibly with the large width of the peaks that hinder the analysis. Analogous results were obtained for $\Phi = 69\%$. On the contrary, the XPCS experiment performed at the other values of surface concentration were characterized by a too high value of exposure time ($\simeq 1sec$) to allow a similar analysis.

Usual XPCS experiments characterize the dynamical heterogeneity by means of the variance calculation only. The extremely high signal-to-noise ratio allows the calculation of the four-times correlation function $g^{(4)}(q;t,\widetilde{\tau})$, using equation 7.16. Here, the correlation time $\widetilde{\tau}$ is kept fixed to τ_C, the time where the variance χ has its maximum (sketched as a white stripe in figure 72). This result enables a direct comparison between the time-scales identified by two intensity autocorrelators, $g^{(2)}(q;t)$ and $g^{(4)}(q;t)$, which is in principle more straightforward than the more common (but indirect) comparison between the time scales identified by a two-times correlator ($g^{(2)}(q;t)$) and a dynamical susceptibility (χ).

The results of the calculation of $g^{(4)}(q;t)$ for the sample at $\Phi = 88\%$ are reported in figure 74a, for several values of q: the four times correlation functions shows a peak whose position τ^*, in a similar way as the variance χ, is shifter towards faster times as the value of $q_{||}$ is increased. Within the experimental uncertainty, the intensity g^* of the peak of $g^{(4)}(q;t)$, reported in figure 74b, is roughly constant over the whole experimental range of $q_{||}$ accessed in this experiment, for

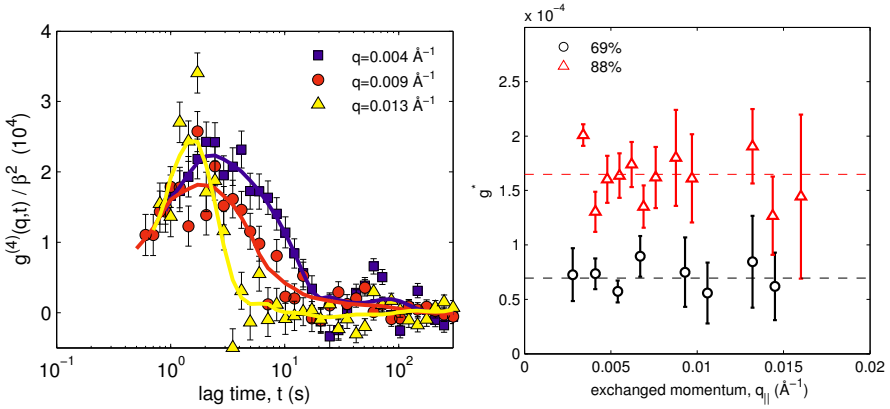

(a) (b)

Figure 74: Four-times correlation function $g^{(4)}(q,t)$, measured on a film of GNPs at $\Phi = 88\%$, for several values of $q_{||}$.

both $\Phi = 69\%$ and $\Phi = 88\%$. Therefore, it is not possible to identify a characteristic spatial scale over which the motion is heterogeneous: similar results were found also in other systems presenting dynamical heterogeneity [124, 99].

On the contrary, the intensity of the peak increases as the concentration is raised. The analysis of the effect of an increased concentration Φ on $g^{(4)}(q;t)$ are detailed in figure 75a. Reaching the higher value of Φ, the peak of $g^{(4)}(q;t)$ is shifted towards slower times and its intensity grows. The increase of the peak intensity g^* is commonly related to an increased dynamical correlation length. This behavior is similar to what is predicted by numerical simulations [78], keeping in mind

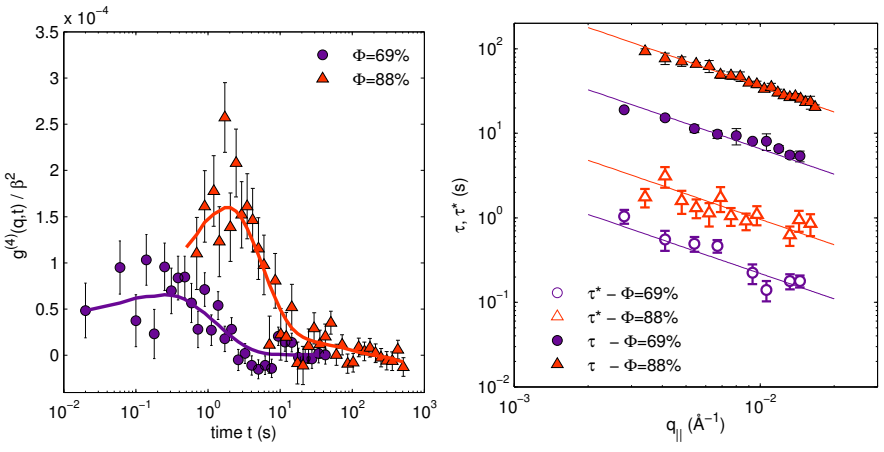

(a) (b)

Figure 75: a) Four-times correlation function measured at $q_{||} = 0.009 Å^{-1}$ at $\Phi = 69\%$ and $\Phi = 88\%$. b) q-dependencies of the position of the peak of $g^{(4)}(q,t)$ (empty symbols) and of the relaxation times τ obtained from the analysis of $g^{(2)}(q;t)$.

the analogy between decreasing temperature in supercooled liquids and increasing packing fraction in colloids. A similar behavior is also exhibited by the variance χ as measured by XPCS on gel systems [75] and it is in agreement with the general idea that dynamical arrest is related to developing heterogeneities.

The characteristic times τ^* - corresponding to the peak of $g^{(4)}(q;t)$- and τ - corresponding to the relaxation time from $g^{(2)}(q;t)$- are reported in figure 75b as a function of $q_{||}$ for different values of Φ. They all scale roughly as $q_{||}^{-1}$ in the very same fashion, however the heterogeneity appears on a time scale much shorter than the dynamics probed by the intensity autocorrelation function. This behavior has been found in other arrested systems, e.g. [124]. No dependence of τ^* on $q_\perp$ was observed, indicating that all the investigated motions (fast and slow) are confined at the air/water interface. Hence, it is reasonable to ascribe the Debye-Waller like reduction of the contrast β, characterized by the localization length a, to heterogeneous fast surface dynamics.

These experimental results are hence in good agreement with earlier simulations and experiments on supercooled liquids and attractive colloids in 3D [75, 78, 125], in which the decreased mobility (determined e. g. by temperature or concentration) is followed by an increase in the range of spatial and temporal correlations between particles.

Part VI

A COMMON VIEW

15 CONCLUSIONS

This Thesis reports a comprehensive characterization of the dynamical properties of Langmuir films belonging to two families:

- polymeric films made of a photosensitive azobenzene-based polyacrylate, PA4;
- films of gold nanoparticles functionalized with dodecanethiol.

The characterization is obtained combining delicate measurements of the interfacial mechanical properties with that of the spontaneous fluctuations in the same samples, an approach inspired by fluctuation/response function theorems. The results are also compared with the phenomenology of the 3D counterparts of the same systems. Interesting analogies are found, the more relevant ones are detailed in the following:

A. Both systems - in "equilibrium" conditions- show viscoelastic response with a dominant *elastic* part, i. e. the storage shear modulus G' is higher than the loss modulus G''.

B. The dependence of the mechanical modulus G as a function of the relevant system variable (temperature and illumination for the photosensitive azopolymer, concentration for the nanoparticle films) is consistent with the behavior found in analogous 3D systems. In particular:
   - in PA4 Langmuir films UV photoperturbation induces a decrease in the mechanical modulus, accompanied by a decrease in the correlation times, fully consistent with what is found in 3D;
   - in the same system, both in dark and under photoperturbation, the temperature dependence of $\eta_{2D} = G''/\omega$ follows the same VFT law observed for the 3D viscosity with EPR experiments [97, 126];
   - in GNPs Langmuir films, the shear modulus G grows following a power law of the reduced concentration, $G \propto \left(\frac{\Phi-\Phi_0}{\Phi_0}\right)^z$, as found in 3D gels [120, 127];

C. The internal dynamics of the systems was measured by means of XPCS on the mesoscopic spatial scale corresponding to tens/hundreds of nanometers. The spontaneous microscopic fluctuation dynamics is connected to the macroscopic elastic mechanical response within the model proposed by Bouchaud and Pitard [73] for the slow relaxation dynamics in elastic solids:

- the correlation functions $g^{(2)}(q;t)$ decay as compressed exponentials,
$$g^{(2)}(q,t) = 1 + \beta e^{-2(t/\tau)^{\gamma}}$$
with exponent $\gamma = 1.5$;
- the relaxation time τ grows as the inverse of the exchanged momentum q, $\tau \propto q^{-1}$.
- The temperature (for azopolymer films) and concentration (for GNPs films) dependencies of the relaxation time τ are compatible with the corresponding dependencies of the mechanical shear modulus G.

D. The existence, and the extent, of dynamical heterogeneities are highly debated subjects within the community studying arrested systems. In this Thesis dynamical heterogeneities were experimentally investigated by XPCS measuring not only the variance of the 2.nd order correlation function (which is the usual approach) but also, and for the first time, the 4.th order temporal correlation function $g^{(4)}(q;t)$.

- The GNP films present pronounced dynamical heterogeneity: the relevant time scale τ^*, indicated by the position of the peak observed in $g^{(4)}(q;t)$, scales as q^{-1}. The intensity of the peak is constant as a function of q, implying that a peculiar spatial scale for the dynamical heterogeneity was not observed. Moreover, the number of particles that move cooperatively increase as the surface concentration is raised.
- Also in the azopolymer film under UV photoperturbation, dynamical heterogeneities were characterized analyzing the q-dependence of the peak observed in the variance χ of the two times correlation function $C(q;t_1,t_2)$. The time scale τ_C identified by the position of the peak is proportional to the inverse of q, as observed for τ. The intensity of the peak decays as q^{-3}, indicating that the size of the cooperative regions is proportional to the cube of the spatial scale probed $d = \frac{2\pi}{q}$.

In general, the time scale of the fast heterogeneous dynamics scale as the relaxation time of the slow dynamics measured using $g^{(2)}(q;t)$; the two time scales are separated by almost an order of magnitude in both system. A similar behavior was found in many arrested systems [26, 72, 75].

It would be interesting to connect, in 2D gel films of GNPs, the presence of heterogeneous dynamics with the hierarchy of heterogeneous structures which is characterized in this Thesis on different spatial scales using a combination of optical and electronic microscopies. In

particular, at low volume fractions, a foam-like structure is observed. At higher values of the surface concentration, although the film packing is increased, the film is still characterized by holes of irregular shape, whose size distribution is compatible with a Levy distribution. In theoretical works and simulations reported in the literature, a "Levy" structure is commonly associated to heterogeneous dynamical fluctuations [128, 129].

15.1 FUTURE WORK

Some problematics encountered during this project have still to be addressed. The characterizations of the mechanical response reported in this Thesis are performed on the macroscopic spatial scale identified by the dimensions of the probe (i. e. an oscillating needle of diameter $D = 0.35mm$), while the internal fluctuations are measured on the spatial scale accessed by X-ray in a small-angle diffraction geometry, e. g. tens/hundreds of nanometers.

It is indeed remarkable to have found many analogies between the two quantities in the two systems investigated, despite this huge gap in the spatial scales investigated. However, a more accurate characterization could be obtained by measuring the mechanical response of the system on the same spatial scale accessed by XPCS, using microrheology techniques, such as MPT. In an even more advanced approach, a combined XPCS/MPT experimental setup may allow a contemporaneous mechanical/dynamical characterization on the very same sample.

At the same time, several points of this analysis remain open to further investigations. In particular, the investigation of 2D film of gold nanoparticles can be improved by studying the dependence of the behavior of the system to:

- different size of the nanoparticles, up to hundreds of nanometers, thus filling the gap of experimental analysis of 2D systems with the theoretical simulations and experiments reported in the literature, mainly performed on systems of micro-particles [130, 131] and macroscopic disks [132].
- different interparticle potentials; while the weakly attractive potential that characterize the GNPs system examined in this work leads to the formation of a gels, a system where nanoparticles interact through a repulsive potential could help to investigate the behavior of 2D glasses.

Finally, similar investigations have recently begun on 2D films of iron-oxide (Fe_3O_4) nanoparticles at the air/water and oil/water interfaces [107], that proved to be subject to aging phenomena.

Part VII

APPENDICES

A

X-RAY SPECKLE VISIBILITY SPECTROSCOPY

The measurements of internal fluctuactions reported in this work show that XPCS is not suited to access very fast dynamics: even if APD detectors and hardware correlators are employed, the faster time scale that can be accessed is close to $1\mu s$. The faster 2D X-ray detector currently available, Medipix, is characterized by a minimum exposure time of $1ms$. On the other hand, synchrotron radiation itself does not possess a temporal structure fast enough to allow the investigation of systems on the picosecond scale.

The construction of X-ray Free Electron Laser sources, like XFEL at Desy (Hamburg, DE), will make the measurement of dynamics down to the femtosecond scale possible. Such a fast timescale can not be observed by means of XPCS with the detectors currently available: a different approach is needed.

As shown, during this project, for XPCS measurements on films of gold nanoparticles (chapter 12), spontaneous fluctuations taking place on a timescale faster than the exposure time of the detector induce a loss of contrast in the diffraction pattern. Subsequently, the

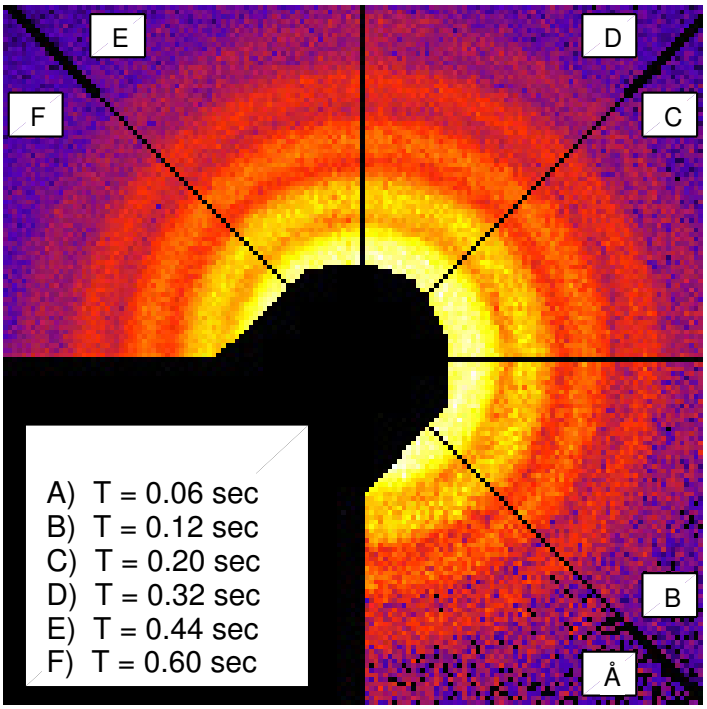

Figure 76: Diffraction pattern of a colloidal suspension of silica spheres of radius $R = 250nm$. Each portion report a measurement performed at a different value of the exposure time.

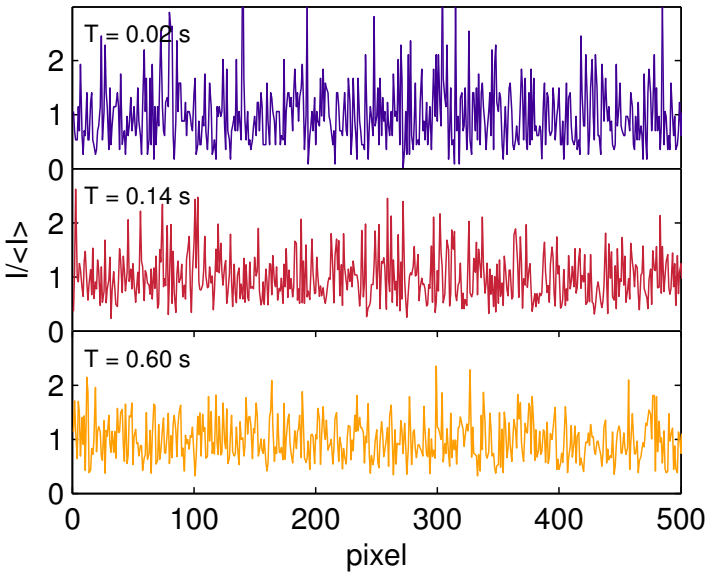

Figure 77: Relative variation of the intensity over the pixels correspondent to $q = 0.004 Å^{-1}$, measured at several values of the exposure time.

speckles are temporally averaged and they tend to fade as the exposure time is increased. If an experiment that quantifies this loss of contrast is performed, in principle it could measure the relaxation times that characterize the dynamics of the system.

The presence of speckles in a diffraction pattern is quantified calculating the normalized variance of the scattered intensity over the ensembles of pixels characterized by a certain value of the exchanged momentum. The analysis of the variance loss as the exposure time of the detector is increased allows the measurement of the relaxation time of the dynamics of the system at the given value of q. This technique is called X-ray Speckle Visibility Spectroscopy (XSVS) [133].

We collaborated to a feasibility experiment proposed by dr.Andrei Fluerasu and coworkers (NSLS-II, Brookhaven National Laboratory, New York, USA) and performed at the ID10A beamline of synchrotron ESRF. Figure 76 reports the X-ray diffraction pattern of a colloidal suspension of silica nanoparticles in propylene glycol (PG) at concentration $\Phi = 1\%$ and constant temperature (12°C). The diffraction pattern is divided into six portions: each portion was measured with a different exposure time. As the exposure time is increased, the diffraction pattern appears "smoother", as the speckles are averaged over time.

During the experiment, diffraction patterns were measured for exposure time ranging from $T = 0.01s$ up to $T = 0.3sec$; the time T was increased by $0.01sec$ steps. In order to improve the statistics of the measurement, for each value of the exposure time we measured a sequence of 10 images. By summing frames, longer exposure times have been be obtained. The detector pixels were grouped into concen-

tric rings, centered on the position of the direct beam; each ring was labeled with the respective value of q.

Figure 77 reports the relative variation of the intensity measured, for several values of the exposure time, over a group of pixel at the same value of q. It can be noted that the fluctuations of relative variation $I/ < I >$ over the pixels are reduced as the exposure time is increased.

The variance of the diffraction pattern -measured during an exposure of duration T- on a ensemble of N pixels characterized by the same value of q is quantified calculating the so-called *speckle visibility*:

$$v(q;T) = \frac{\sum_1^N I_i^2/N}{\langle I \rangle^2} - 1 \tag{A.1}$$

where I_i is the intensity measured by the i-th pixel and $\langle I \rangle$ is the intensity averaged over the pixels. The visibility v was calculated using equation A.1 on each ring -i.e. for each value of q- for increasing exposure time. A subset of the resulting curves is reported in figure 78.

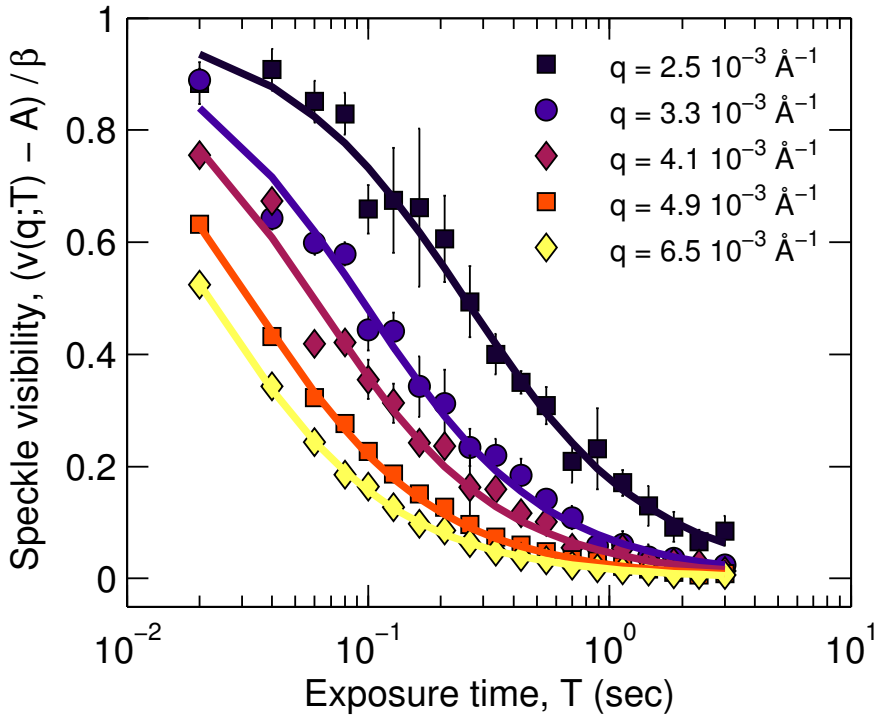

Figure 78: Normalized speckle visibility $(v(q,T) - A)/\beta$ reported for several values of q, measured on the low concentration colloidal suspension described in the text. Continuous lines are fit with equation A.3.

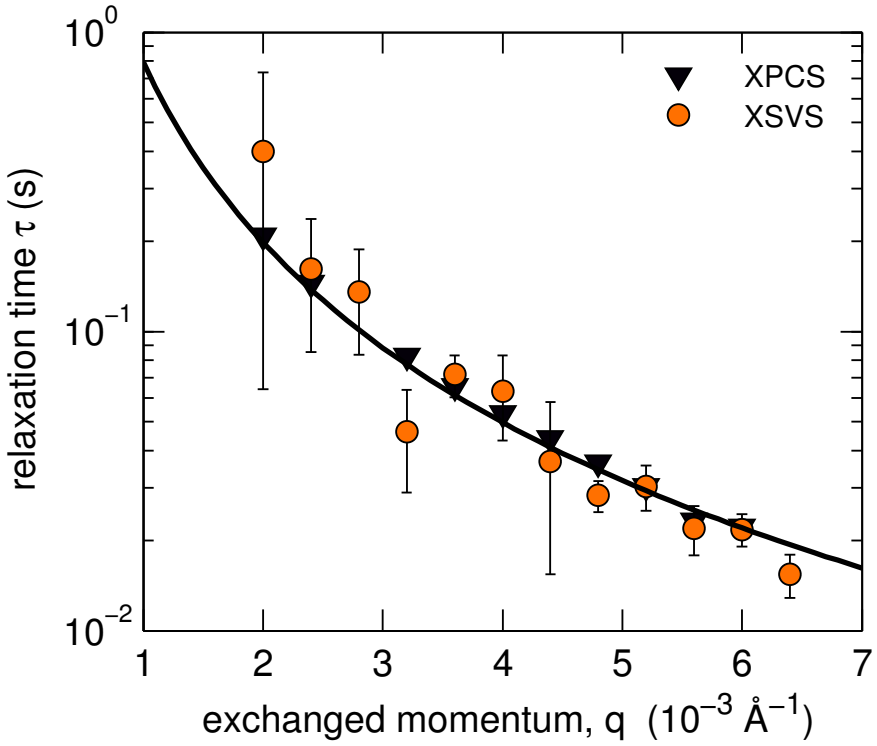

Figure 79: Relaxation time τ as a function of q (circles), obtained from the fitting of visibility $v(q;T)$ with equation A.3. Data are compared with the relaxation times obtained from the XPCS analysis of a series of 5000 frames with constant exposure of 1msec (trinagles).

It can be shown that the visibility is related to the intermediate scattering function $g^{(1)}(q,t)$:

$$v(q;T) = 2\beta \int_0^T \frac{1-t/T}{T} \left| g^{(1)}(q;t) \right|^2 dt \tag{A.2}$$

The sample considered here is a low-concentration colloidal suspension: hence, the particles are likely to be subject to Brownian motion. Consequently, the intermediate scattering function decay as a simple exponential, $\exp(-t/\tau)$, and equation A.2 reduces to

$$v(q;T) = \beta \frac{e^{-2T/\tau} - 1 + 2T/\tau}{2\,(T/\tau)^2} + A \tag{A.3}$$

where the baseline term A is introduce to account for higher-than-expected values of v due to too-low count rates (i. e. see section A.1). This model of the decay of the speckle visibility with increasing exposure time was used to fit the experimental data: the resulting curves are shown as continuous lines in figure 78.

The relaxation time τ, measured for several values of q using this fitting procedure, is reported in figure 79. Its q-dependence is compatible with the q^{-2} behavior expected for Brownian motion, which

is reported in the figure as a continuous line. Furthermore, the relaxation times were measured also by means of an XPCS experiment (5000 frames with 1msec exposure time) performed on the very same sample: the agreement between the results of the two techniques is remarkable.

In conclusion, in an ideal XFEL XSVS experiment, the X-ray detector receives a number n of pulses -each of them with a duration $dt = 15fs$- scattered from the sample, during its exposure time $\widetilde{T}$ (of the order of 1ms). The effective exposure time of the diffraction pattern is $T = n \cdot dt$. The required series of frames with increased exposure time is obtained increasing the number of pulses that hit the sample during the (fixed) detector exposure time $\widetilde{T}$.

A.1 CRITICAL DISCUSSION

Several experimental conditions have to be satisfied in order to obtain a sufficiently high signal-to-noise ratio in a XSVS experiment. At first, the experimental setup has to be configured so that the observation of speckles is possible: these requirements are the same that have to be satisfied in an XPCS experiment.

More strict conditions have to be posed on the intensity of the signal measured by the detector. If the intensity is too low, the detector image of the diffraction pattern contains mainly 0 and 1, generating a speckle visibility which is higher than the value expected at the exposure time considered. This problem is particularly intense at high values of q, where the diffracted signal intensity is lower. In the test experiment described in this chapter, the maximum value of q considered is $q = 0.0065\text{Å}^{-1}$. At higher values of q, for $T < 0.1sec$ the measured intensity was too low to correctly measure the speckle visibility.

Another source of miscalculation of the speckle visibility arises when dark counts have to be subtracted to the measured intensity; the Medipix detector does not present this problem, given its single-photon counting capabilities, but the problem may arise when employing an X-ray CCD detector. A secondary aspect to be noted is that the XSVS experiment reported here required the acquisition of 300 frames with different values of the exposure time, while the XPCS experiment performed to check the results required 5000 frames, with a huge saving of computational space and time.

BIBLIOGRAPHY

[1] J. W. Strutt Lord Rayleigh, Philosophical Magazine **48** (1899).

[2] A. Pockels, Nature **43** (1891).

[3] I. Langmuir, Science (New York, N.Y.) **84**, 379 (1936), ISSN 0036-8075.

[4] I. Langmuir and V. J. Schaefer, J. Am. Chem. Soc. **58**, 284 (1936).

[5] I. Langmuir and V. J. Schaefer, J. Am. Chem. Soc. **59**, 2400 (1937), ISSN 1438-8359.

[6] K. Blodgett, Science **89**, 60 (1939).

[7] R. Kubo, Reports on Progress in Physics **29**, 255 (1966), ISSN 00344885.

[8] B. Berne and R. Pecora, *Dynamic Light Scattering* (Dover, New York, 1976), 2000th ed.

[9] A. Tamime, *Structure of diary products* (John Wiley & Sons, Inc., 2007), ISBN 9781405129756.

[10] Y. Liu, H. Miyoshi, and M. Nakamura, International journal of cancer. Journal international du cancer **120**, 2527 (2007), ISSN 0020-7136.

[11] B. P. Timko, T. Cohen-Karni, Q. Qing, B. Tian, and C. M. Lieber, IEEE transactions on nanotechnology **9**, 269 (2010), ISSN 1941-0085.

[12] S. Lal, S. E. Clare, and N. J. Halas, Accounts of Chemical Research **41** (2008).

[13] G. Attolini, F. Rossi, F. Fabbri, M. Bosi, G. Salviati, and B. E. Watts, in *Nanowires*, edited by P. Prete (INTECH, Croatia, 2010), March, chap. 1, p. 414, ISBN 9789537619794.

[14] M. Llusar and C. Sanchez, Chemistry of Materials **20**, 782 (2008), ISSN 0897-4756.

[15] H. Nakahara, S. Lee, Y. Shoyama, and O. Shibata, Soft Matter (2011), ISSN 1744-683X.

[16] P. Rispoli, R. Carzino, T. Svaldo-Lanero, A. Relini, O. Cavalleri, A. Fasano, G. M. Liuzzi, G. Carlone, P. Riccio, A. Gliozzi, et al., Biophysical journal **93**, 1999 (2007), ISSN 0006-3495.

[17] L. Cristofolini, M. P. Fontana, F. Serra, A. Fasano, P. Riccio, and O. Konovalov, European biophysics journal : EBJ **34**, 1041 (2005), ISSN 0175-7571.

[18] W. A. Lopes and H. M. Jaeger, Nature **414**, 735 (2001), ISSN 0028-0836.

[19] S. Xie, A. Natansohn, and P. Rochon, Chemistry of Materials **5**, 403411 (1993).

[20] T. Berzina, A. Pucci, G. Ruggeri, V. Erokhin, and M. P. Fontana, Synthetic Metals **161**, 1408 (2011), ISSN 03796779.

[21] A. C. Balazs, T. Emrick, and T. P. Russell, Science (New York, N.Y.) **314**, 1107 (2006), ISSN 1095-9203.

[22] G. Kumar and D. Neckers, Chemical Reviews **89**, 1915 (1989).

[23] M. Yamada, M. Kondo, J.-i. Mamiya, Y. Yu, M. Kinoshita, C. J. Barrett, and T. Ikeda, Angewandte Chemie (International ed. in English) **47**, 4986 (2008), ISSN 1521-3773.

[24] V. Balzani, A. Credi, S. Silvi, and M. Venturi, Chemical Society reviews **35**, 1135 (2006), ISSN 0306-0012.

[25] V. P. Veedu, A. Cao, X. Li, K. Ma, C. Soldano, S. Kar, P. M. Ajayan, and M. N. Ghasemi-Nejhad, Nature materials **5**, 457 (2006), ISSN 1476-1122.

[26] L. Cipelletti and L. Ramos, J. Phys.: Condens. Matter **17**, 253 (2005).

[27] G. Ruocco, Nature materials **7**, 842 (2008), ISSN 1476-1122.

[28] H. Shintani and H. Tanaka, Nature materials **7**, 870 (2008), ISSN 1476-1122.

[29] A. Einstein, Annalen der Physik **322**, 549 (1905), ISSN 00033804.

[30] H. Nyquist, Physical Review **32**, 110 (1928), ISSN 0031-899X.

[31] R. Kubo, M. Toda, and N. Hashitsume, *Statistical Physics II* (Iwanami, Tokyo, 1978).

[32] T. Mason and D. Weitz, Physical Review Letters **75**, 2770 (1995), ISSN 0031-9007.

[33] A. J. Levine and T. C. Lubensky, Physical Review Letters **85** (2000).

[34] T. A. Waigh, Reports on Progress in Physics **68**, 685 (2005), ISSN 0034-4885.

[35] P. Cicuta and A. M. Donald, Soft Matter **3**, 1449 (2007), ISSN 1744-683X.

[36] C. Giles, S. Forrester, and G. Roberts, in *Langmuir Blodgett films*, edited by G. Roberts (Plenum Press, New York, 1990), chap. 1.

[37] G. Roberts, *Langmuir-Blodgett Films* (Plenum Press, 1990), ISBN 978-0306433160.

[38] V. Kaganer, H. Möhwald, and P. Dutta, Reviews of Modern Physics **71**, 779 (1999).

[39] J. Boussinesq, Ann. Chim. Phys. (Ser.) **29**, 349 (1913).

[40] J. Boussinesq, C.R. Acad. Sci. **156**, 1124 (1913).

[41] R. Miller, R. Wustneck, J. Krägel, and G. Kretzschmar, Colloids and Surfaces A: Physicochemical and Engineering Aspects **111**, 75 (1996).

[42] E. Spigone, G. Cho, G. G. Fuller, and P. Cicuta, Langmuir **25**, 7457 (2009), ISSN 0743-7463.

[43] H. Rehage and H. Hoffmann, The Journal of Physical Chemistry **92**, 4712 (1988), ISSN 0022-3654.

[44] R. Larson, *The structure and rheology of complex fluids* (Oxford University Press, 1999), ISBN 0-19-512197-X.

[45] B. Warburton, Current Opinion in Colloid & Interface Science **1**, 481 (1996), ISSN 13590294.

[46] C. F. Brooks, G. G. Fuller, C. W. Frank, and C. R. Robertson, Langmuir **15**, 2450 (1999), ISSN 0743-7463.

[47] S. Reynaert, C. F. Brooks, P. Moldenaers, J. Vermant, and G. G. Fuller, Journal of Rheology **52**, 261 (2008), ISSN 01486055.

[48] A. Levine, T. Liverpool, and F. MacKintosh, Physical Review Letters **93**, 1 (2004), ISSN 0031-9007.

[49] C. F. Brooks, G. Fuller, C. W. Frank, and C. R. Robertson, Langmuir **5**, 2450 (1999).

[50] E. Shotton, K. Wibberley, B. Warburton, S. S. Davis, and P. L. Finlay, Rheologica Acta **10**, 142 (1971).

[51] R. S. Ghaskadvi, J. B. Ketterson, R. C. MacDonald, and P. Dutta, Review of Scientific Instruments **68**, 1792 (1997), ISSN 00346748.

[52] P. Cicuta and E. M. Terentjev, The European physical journal. E, Soft matter **16**, 147 (2005), ISSN 1292-8941.

[53] P. Cicuta, Journal of colloid and interface science **308**, 93 (2007), ISSN 0021-9797.

[54] J. T. Petkov, T. D. Gurkov, B. E. Campbell, and R. P. Borwankar, Langmuir **16**, 3703 (2000), ISSN 0743-7463.

[55] M. Sacchetti, H. Yu, and G. Zografi, Review of Scientific Instruments **64**, 1941 (1993), ISSN 00346748.

[56] T. Mason and D. Weitz, Physical Review Letters **74**, 1250 (1995), ISSN 0031-9007.

[57] R. Evans, M. Tassieri, D. Auhl, and T. Waigh, Physical Review E **80** (2009), ISSN 1539-3755.

[58] F. Ortega, H. Ritacco, and R. G. Rubio, Current Opinion in Colloid & Interface Science **15**, 237 (2010), ISSN 13590294.

[59] K. Danov, R. Dimova, and B. Pouligny, Physics of Fluids **12**, 2711 (2000).

[60] T. Fischer, P. Dhar, and P. Heinig, Journal of Fluid Mechanics **558**, 451 (2006).

[61] M. Sutton, Comptes Rendus Physique **9**, 657 (2008), ISSN 16310705.

[62] D. Orsi, A. Fluerasu, L. Cristofolini, A. Moussaïd, F. Zontone, and A. Madsen, Physical Review E (2011).

[63] P. N. Pusey, in *Liquids,Freezing and the Glass Transition*, edited by J. Hansen, D. Levesque, and J. Zinn-Justin (Elsevier, Amsterdam, 1991), pp. 763–942.

[64] G. Brambilla, D. El Masri, M. Pierno, L. Berthier, L. Cipelletti, G. Petekidis, and a. Schofield, Physical Review Letters **102**, 3 (2009), ISSN 0031-9007.

[65] G. Brambilla, D. El Masri, M. Pierno, L. Berthier, L. Cipelletti, and a. Schofield, Physical Review Letters **104**, 169602 (2010), ISSN 0031-9007.

[66] W. Götze, in *Liquids, freezing and the glass transition*, edited by J. P. Hansen, D. Levesque, and J. Zinn-Justin (North-Holland, Amsterdam, 1991).

[67] W. Götze, Journal of Physics Condensed Matter **11**, A1 (1999).

[68] L. Cipelletti, S. Manley, R. C. Ball, and D. A. Weitz, Physical Review Letters **84**, 2275 (2000).

[69] A. Fluerasu, A. Moussaid, A. Madsen, and A. Schofield, Physical Review E **76**, 10401 (2007).

[70] L. Ramos and L. Cipelletti, Physical Review Letters **87**, 245503 (2001).

[71] L. Cipelletti, L. Ramos, S. Manley, E. Pitard, D. A. Weitz, E. E. Pashkovski, and M. Johansson, Faraday Discussions **123**, 237 (2003), ISSN 13596640.

[72] R. Bandyopadhyay, D. Liang, H. Yardimci, D. A. Sessoms, M. A. Borthwick, S. Mochrie, J. L. Harden, and R. L. Leheny, Physical Review Letters **93**, 228302 (2004).

[73] J.-P. Bouchaud and E. Pitard, The European Physical Journal E **6**, 231 (2001).

[74] H. Guo, J. N. Wilking, D. Liang, T. G. Mason, J. L. Harden, and R. L. Leheny, Physical Review E **75**, 041401 (2007).

[75] A. Madsen, R. L. Leheny, H. Guo, M. Sprung, and O. Czakkel, New Journal of Physics **12**, 055001 (2010).

[76] G. Brown, P. Rikvold, M. Sutton, and M. Grant, Physical Review E **60**, 5151 (1999), ISSN 1063-651X.

[77] B. Chung, S. Ramakrishnan, R. Bandyopadhyay, D. Liang, C. F. Zukoski, J. L. Harden, and R. L. Leheny, Physical Review Letters **96**, 228301 (2006).

[78] L. Berthier, Physics **4** (2011), ISSN 1943-2879.

[79] M. Sutton, S. G. J. Mochrie, T. Greytak, S. E. Nagler, L. E. Berman, G. A. Held, and G. B. Stephenson, Nature **352**, 608 (1991), ISSN 0028-0836.

[80] X. Llopart, M. Campbell, R. Dinapoli, D. San Segundo, and E. Pernigotti, IEEE Transactions on Nuclear Science **49**, 2279 (2002).

[81] K. G. Yager and C. J. Barrett, Journal of Photochemistry and Photobiology A: Chemistry **182**, 250 (2006), ISSN 10106030.

[82] A. Natansohn and P. Rochon, Chemical reviews **102**, 4139 (2002), ISSN 0009-2665.

[83] P. De Gennes, Physics Letters A **28**, 725 (1969), ISSN 03759601.

[84] R. Hildebrandt, M. Hegelich, H. Keller, G. Marowsky, S. Hvilsted, N. Holme, and P. Ramanujam, Physical review letters **81**, 5548 (1998).

[85] L. Cristofolini, M. P. Fontana, T. Berzina, and O. Konovalov, Physical Review E **66** (2002), ISSN 1063-651X.

[86] L. Cristofolini and M. P. Fontana, PHILOSOPHICAL MAGAZINE **84**, 1537 (2004), ISSN 1478-6443.

[87] A. M. Ketner, R. Kumar, T. S. Davies, P. W. Elder, and S. R. Raghavan, Journal of the American Chemical Society **129**, 1553 (2007), ISSN 0002-7863.

[88] E. Verploegen, J. Soulages, M. Kozberg, T. Zhang, G. Mckinley, and P. Hammond, Angew. Chem. Int. Ed. **48**, 3494 (2009).

[89] A. M. Ketner, R. Kumar, T. S. Davies, P. W. Elder, and S. R. Raghavan, Journal of the American Chemical Society **129**, 1553 (2007), ISSN 0002-7863.

[90] P. Camorani and M. P. Fontana, Physical Review E **73**, 11703 (2006).

[91] J. L. Keddie, R. A. L. Jones, and R. A. Cory, Europhysics Letters **27**, 59 (1994), ISSN 0295-5075.

[92] J. Forrest, K. Dalnoki-Veress, J. R. Stevens, and J. R. Dutcher, Physical Review Letters **77**, 2002 (1996).

[93] B. Jérôme and J. Commandeur, Nature **386**, 589 (1997).

[94] L. Cristofolini, S. Arisi, and M. P. Fontana, Physical Review Letters **85**, 4912 (2000).

[95] L. Andreozzi, M. P. Fontana, F. Francia, M. Giordano, D. Leporini, and M. Rateo, Journal of Non-Crystalline Solids **172-174**, 943 (1994).

[96] L. Cristofolini, T. Berzina, M. P. Fontana, and O. Konovalov, Molecular Crystals and Liquid Crystals **375**, 689 (2002), ISSN 1058-725X.

[97] L. Andreozzi, *Ph.D. thesis* (University of Pisa, Pisa, 1997).

[98] L. Cristofolini, P. Facci, P. Camorani, and M. P. Fontana, Journal of Physics Condensed Matter **11**, A355 (1999).

[99] D. Orsi, L. Cristofolini, M. P. Fontana, E. Pontecorvo, C. Caronna, A. Fluerasu, F. Zontone, and A. Madsen, Physical Review E **82**, 031804 (2010), ISSN 1539-3755.

[100] K. Ueno, S. Juodkazis, T. Shibuya, Y. Yokota, V. Mizeikis, K. Sasaki, and H. Misawa, Journal of the American Chemical Society **130**, 6928 (2008), ISSN 1520-5126.

[101] M.-C. Daniel and D. Astruc, Chemical reviews **104**, 293 (2004), ISSN 0009-2665.

[102] C. Lee, Y. Kang, K. Lee, S. R. Kim, D.-j. Won, J. S. Noh, H. K. Shin, C. K. Song, Y. S. Kwon, H.-m. So, et al., Current Applied Physics **2**, 39 (2002).

[103] M. Namdeo, S. Saxena, R. Tankhiwale, M. Bajpai, Y. M. Mohan, and S. K. Bajpai, Journal of Nanoscience and Nanotechnology **8**, 3247 (2008), ISSN 15334880.

[104] W. Zhao, M. a. Brook, and Y. Li, Chembiochem : a European journal of chemical biology **9**, 2363 (2008), ISSN 1439-7633.

[105] N. Felidj, J. Aubard, G. Levi, J. R. Krenn, A. Hohenau, G. Schider, A. Leitner, and F. R. Aussenegg, Applied Physics Letters **82**, 3095 (2003), ISSN 00036951.

[106] F. Bresme and M. Oettel, Journal of Physics: Condensed Matter **19**, 413101 (2007), ISSN 0953-8984.

[107] L. Isa, E. Amstad, M. Textor, and E. Reimhult, Chimia **64**, 1 (2010).

[108] L. Isa, E. Amstad, K. Schwenke, E. Del Gado, P. Ilg, M. Kröger, and E. Reimhult, Soft Matter pp. 7663–7675 (2011), ISSN 1744-683X.

[109] S. Chen and K. Kimura, Langmuir **15**, 1075 (1999), ISSN 0743-7463.

[110] W. Haiss, N. T. K. Thanh, J. Aveyard, and D. G. Fernig, Analytical chemistry **79**, 4215 (2007), ISSN 0003-2700.

[111] X. Chen, J. Li, and L. Jiang, Nanotechnology **11**, 108 (2000).

[112] E. Aumaitre, D. Vella, and P. Cicuta, Soft Matter **7**, 2530 (2011).

[113] D. Orsi, L. Cristofolini, M. Fontana, E. Pontecorvo, C. Caronna, A. Fluerasu, F. Zontone, and A. Madsen, Physical Review E **82**, 031804 (2010), ISSN 1539-3755.

[114] B. Gnedenko and A. Kolmogorov, *Limit distributions for sums of independent random variables* (Addison-Wesley Cambridge, 1954), ISBN 0471939692.

[115] W. C. K. Poon, E. R. Weeks, and C. P. Royall, Soft Matter (2011), ISSN 1744-683X.

[116] H. Guo, S. Ramakrishnan, J. L. Harden, and R. L. Leheny, The Journal of Chemical Physics **135**, 154903 (2011), ISSN 00219606.

[117] D. Stauffer, A. Coniglio, and M. Adam, *Polymer Networks*, vol. 44 of *Advances in Polymer Science* (Springer Berlin Heidelberg, Berlin, Heidelberg, 1982), ISBN 978-3-540-11471-0.

[118] H. H. Winter and F. Chambon, Journal of Rheology **30**, 367 (1986).

[119] a. M. Corrigan and a. M. Donald, The European physical journal. E, Soft matter **28**, 457 (2009), ISSN 1292-895X.

[120] V. Trappe, V. Prasad, L. Cipelletti, P. N. Segre, and D. a. Weitz, Nature **411**, 772 (2001), ISSN 0028-0836.

[121] P. Sollich, F. Lequeux, P. Hébraud, and M. Cates, Physical Review Letters **78**, 2020 (1997), ISSN 0031-9007.

[122] A. J. C. Ladd, The Journal of Chemical Physics **93**, 3484 (1990), ISSN 00219606.

[123] O. Czakkel and A. Madsen, EPL (Europhysics Letters) **95**, 28001 (2011), ISSN 0295-5075.

[124] S. Maccarrone, G. Brambilla, O. Pravaz, A. Duri, M. Ciccotti, J.-M. Fromental, E. Pashkovski, A. Lips, D. Sessoms, V. Trappe, et al., Soft Matter **6**, 5514 (2010), ISSN 1744-683X.

[125] A. Duri, D. Sessoms, V. Trappe, and L. Cipelletti, Physical Review Letters **102**, 085702 (2009), ISSN 0031-9007.

[126] D. Orsi, L. Cristofolini, and M. Fontana, Journal of Non-Crystalline Solids **357**, 580 (2011), ISSN 0022-3093.

[127] A. M. Corrigan and A. M. Donald, Langmuir **25**, 8599 (2009).

[128] O. Dauchot, D. J. Durian, and M. van Hecke, in *Dynamical Heterogeneities in Glasses, Colloids, and Granular Media*, edited by L. Berthier, G. Biroli, J.-P. Bouchaud, L. Cipelletti, and W. VanSaarloos (Oxford Scholarship Online, Oxford, UK, 2011), chap. 6, 1010.0873.

[129] P. Buonsante, R. Burioni, and a. Vezzani, Physical Review E **84**, 1 (2011), ISSN 1539-3755.

[130] P. Yunker, Z. Zhang, and a. G. Yodh, Physical Review Letters **104**, 2 (2010), ISSN 0031-9007.

[131] C. O'Hern, S. Langer, A. Liu, and S. Nagel, Physical Review Letters **88**, 3 (2002), ISSN 0031-9007.

[132] P. Lemieux and D. Durian, Physical review letters **85**, 4273 (2000), ISSN 1079-7114.

[133] R. Bandyopadhyay, a. S. Gittings, S. S. Suh, P. K. Dixon, and D. J. Durian, Review of Scientific Instruments **76**, 093110 (2005), ISSN 00346748.